Turbulence structures in the planetary boundary layer measured with a Doppler LIDAR

Turbulente Strukturen in der planetaren Grenzschicht gemessen mit einem Doppler LIDAR

Diplomarbeit
im Fach Meteorologie

Vorgelegt von

Roger Huckle

Institut für Meteorologie und Klimaforschung
Universität Karlsruhe

November 30, 2005

Deutsche Zusammenfassung

Der größte Teil des Lebens spielt sich auf der Erdoberfläche ab. Hier sind wir ständig von der Luft der planetaren Grenzschicht umgeben. Dieser Teil der Atmosphäre wird durch ihren turbulenten Zustand charakterisiert. In einer turbulenten Strömung existieren, im Gegensatz zu laminaren Strömungen, Wirbel in allen Größenordnungen. Im Inertialbereich des Energiespektrums wird die Turbulenzenergie von den großen zu den kleinen Wirbeln weiter gegeben.

Turbulenz, insbesondere solche die durch Konvektion entsteht, ist für das Leben auf der Erde von großer Bedeutung. Turbulenz ist für die vollständige homogene Durchmischung der planetaren Grenzschicht mit Feuchte und Spurenstoffen verantwortlich. Ohne diese Durchmischung wäre die bodennahe Luft nach kürzester Zeit vollständig verschmutzt und würde ein Leben unmöglich machen. Unter konvektiven Bedingungen ist sogar ein Austausch von Luft und Luftbeimengungen zwischen Grenzschicht und freier Atmosphäre durch ein Überschießen der aufsteigenden Luftmassen durch die begrenzende Inversion möglich.

Untersuchungen und Messungen der planetaren Grenzschicht wurden während des gesamten letzten Jahrhunderts durchgeführt. Bereits 1915 beschäftigte sich Taylor als erster Meteorologe mit der planetaren Grenzschicht. Bis heute ist das größte Problem beim Messen in der Grenzschicht mit in-situ Messgeräten, dass nur ein kleiner Teil der planetaren Grenzschicht erfasst werden kann. Bei der Verwendung von meteorologischen Messmasten, wie denen in Cabauw, BAO-Boulder oder im FZK, kann maximal in den untersten 300 m der Grenzschicht gemessen werden. Flugzeuge können in größeren und verschiedenen Höhen messen, sie erfassen aber nur kurze Zeiträume und haben eine geringe vertikale Auflösung. Radiosonden können die gesamte Grenzschicht messen, geben allerdings nur eine Momentaufnahme wieder. Zudem sind Flugzeug- und Radiosondenmessungen kosten- und personalintensiv.

Um kontinuierliche Messungen der kompletten Grenzschicht mit einer hohen zeitlichen und räumlichen Auflösung zu ermöglichen, muss auf Fernerkundungsinstrumente zurückgegriffen werden. Die Verwendung eines Lidar ist daher für diese Zwecke ideal.

Ein LIDAR (Light Detecting And Ranging) sendet einen, in der Regel

gepulsten, Laserstrahl in die Atmosphäre. Dabei sind die Messgrößen die erfasst werden können von der Wellenlänge des Lasers abhängig. Das hier verwendete Doppler Lidar hat eine Wellenlänge von 2 μm. Das ausgesandte Licht wird somit an Aerosolen und größeren Teilchen gestreut und zum Teil reflektiert. Durch die Bewegung des Teilchens erfährt das Licht eine Frequenzverschiebung, aufgrund dieses Doppler-Effekts kann die radiale Windgeschwindigkeit des Teilchens, relativ zum Lidar, bestimmt werden. Um voneinander unabhängige Messwerte zu bekommen wird der Laserpuls in Entfernungsintervalle, so genannte range gates, aufgeteilt.

Die ersten Anwendungen der Lidar Technik für die Meteorologie fanden zu Beginn der 1970er Jahre mit CO_2 Lasern statt. Heutzutage werden unterschiedliche Lidar-Systeme eingesetzt, die aufgrund ihrer verschiedenen Wellenlängen, verschiedene Parameter der Atmosphäre messen können. Verbreitet sind heute neben dem Doppler Lidar noch das Raman Lidar (misst den Wasserdampf und Spurenstoffe mit Hilfe der Raman-Streuung) und das DIAL (Differential Absorption Lidar), welches ebenfalls Wasserdampf und andere Spurengase misst, aber mittels der Absorption des Laserlichts.

Im Juni 2004 wurde vom Institut für Meteorologie und Klimaforschung (IMK) am Forschungszentrum Karlsruhe (FZK)/Universität Karlsruhe ein neues kohärentes Doppler Lidar in Betrieb genommen. In den folgenden Monaten wurden eine Reihe von Messungen durchgeführt. Diese beinhalteten auch Vergleichsmessungen mit anderen Messgeräten des IMK. Außerdem wurden an Tagen mit Konvektion und konvektiver Turbulenz Messungen mit verschiedenen Scan Strategien des Lidars durchgeführt. Diese Messungen fanden im Forschungszentrum Karlsruhe, 12 km nördlich von Karlsruhe, statt. Für diese Diplomarbeit wurden Daten vom 2. und 5. August 2004 verwendet, welche mit zwei verschiedenen Scan Modi aufgezeichnet wurden. Für einige Untersuchungen wurden zudem Daten des 200 m Mastes des Forschungszentrums verwendet.

Das Hauptziel dieser Diplomarbeit war zum einen die Erfassung von charakteristischen Strukturen in der planetaren Grenzschicht mit und ohne Bewölkung an Tagen mit flacher und hochreichender Konvektion sowie der Vergleich der erhaltenen Daten mit den bekannten Theorien aus der Literatur. Es sollte festgestellt werden ob das Doppler Lidar in der Lage ist diese Charakteristika zu messen und ob sich diese Theorien

auf die bewölkte konvektive Grenzschicht anwenden lassen.

Für die Messungen am 5. August wurden sogenannte ppi-Scans (plan position indicator) mit Elevationswinkeln von 88°, 86°, 82°, 78° und 74° durchgeführt. Ein ppi-Scan besteht aus einer 360° Drehung in Azimutrichtung bei einer festen Elevation. Um aus den radialen Windgeschwindigkeiten eines ppi-Scans die drei Windkomponenten zu erhalten, wurde der VAD-Algorithmus (Velocity Azimuth Display) verwendet. Dabei wird die radiale Windgeschwindigkeit über den Azimutwinkel aufgetragen, aus der dabei entstehenden sinusförmigen Kurve kann die horizontale Windrichtung (Minimum) und die horizontale Windgeschwindigkeit (Amplitude) abgeleitet werden. Die w-Komponente ergibt sich aus der Y-Achsenverschiebung. Vorraussetzung für die Anwendung dieser Methode ist die relative Stationarität des horizontalen Windfeldes während eines ppi-Scans. Bei einer Dauer von ca. 1 Minute war dies für die vorliegenden Messungen gewährleistet. Die Messfrequenz betrug 1 Hz.

Um turbulente Strukturen am 5. August zu identifizieren, wurde durch Subtraktion des Anteils des Horizontalwindes die w-Komponente für jeden Strahl des Lidars berechnet. Somit standen ca. 550 Messwerte der vertikalen Windkomponente für jeden ppi-Scan zur Verfügung. Mit dem Mathematikprogramm Matlab wurden die Werte aus einem Block von 5 ppi-Scans in einer Draufsicht in einer Ebene in der horizontalen Entfernung zum Lidar dargestellt. Trotz der verschiedenen Elevationen wurde immer das gleiche range gate verwendet, da die Höhendifferenz zwischen den Elevationswinkeln geringer war als zwischen verschiedenen range gates. Mit einer Dreiecksinterpolationsmethode nach Delaunay wurden die Bereiche zwischen den Messringen interpoliert.

Die Ergebnisse waren nicht sehr zufriedenstellend. Zwei wesentliche Aspekte müssen bei der graphischen Darstellung berücksichtigt werden. Zum einen ist der Elevationswinkel bei den zwei innersten Ringen zu hoch, der Einfluss der horizontalen Windgeschwindigkeit auf die radiale Windmessung ist sehr gering und wird möglicherweise überschätzt und somit könnte die Berechnung der w-Komponente inkorrekt sein. Zum anderen, und wesentlich schwerwiegender, ist die Zeitspanne von ca. 5 Minuten, die für einen Block von fünf Ringen benötigt wird. Diese ist viel zu lang, als dass die Verschiebung durch den horizontalen Wind ignoriert werden könnte. Das Problem besteht darin, dass die horizontale Drift der Turbulenzelemente im Vergleich zum Horizontalwind nicht bekannt

ist. Daher sind weitere Messungen mit anderen Scan Modi nötig. Eine mögliche Messmethode könnte die Anwendung von rhi (range heihgt indicator) Scans orthogonal zur Windrichtung sein. Bei rhi-Scans wird die Elevation bei einem festen Azimutwinkel geändert. Dadurch driften die Turbulenzelemente am Lidar vorbei, somit wäre möglicherweise eine Relation zwischen horizontaler Windgeschwindigkeit und Drift der Turbulenzelemente zu finden

Die Messungen am 2. August wurden mit einem senkrecht blickenden Lidar, ohne Drehbewegungen mit einer Messfrequenz von 1 Hz, gemacht. Hierbei wurde direkt die Vertikalkomponente des Windes gemessen. Aus den Daten vom 2. August, konnte sowohl die Grenzschichtentwicklung als auch die vertikale Verteilung der vertikalen Windgeschwindigkeit und Turbulenz bestimmt werden. Mit Hilfe des Signal zu Rauschverhältnisses (SNR) konnte sowohl die Entwicklung der morgendlichen Mischungsschicht, als auch die vertikale Ausdehnung der Residualschicht und der ab Mittag voll entwickelten Grenzschicht detektiert werden. Unter der Annahme, dass innerhalb der Grenzschicht eine erhöhte Konzentration von Aerosolen vorhanden ist, kann das, im Vergleich zur freien Atmosphäre, bessere Rückstreuverhältnis als Indikator für die Ausdehnung der Mischungsschicht benutzt werden. In Verbindung mit den Daten für den Vertikalwind ist ein Pulsieren der anwachsenden Grenzschicht in den Morgenstunden zu erkennen. Vertikales Anwachsen der Mischungsschicht ist verbunden mit starken vertikalen Winden von zum Teil über 3 $m\,s^{-1}$. Ein solches Pulsieren wäre mit Radiosondenmessungen nicht zu erfassen gewesen.

Während der Mittags- und frühen Nachmittagsstunden zogen einzelne Wolken über das Lidar hinweg, diese wurden gesondert analysiert. Die Untersuchung der vertikalen Profile von Vertikalwind und Standardabweichung (σ_w) zeigte, dass diese sich ähnlich zu den bekannten Profilen aus der Literatur verhielten. In beiden Fällen war ein Betragsmaximum in der Mitte der Mischungsschicht zu finden. Für die bewölkten Zeiträume waren die Ergebnisse allerdings unterschiedlich. Für die ersten Wolken konnte eine Verschiebung der maximalen vertikalen Windgeschwindigkeit und von σ_w in den Bereich der oberen Grenzschicht bzw. der Wolkenbasis festgestellt werden. Bei der letzten Wolke wurde dies wiederum nicht festgestellt, somit dürfte es sich um eine Kumulus Wolke im letzten Stadium ihres Lebenszyklus gehandelt haben. In diesem Fall wird dann keine zusätzliche Energie durch

Verdunstung in der Wolkenbasis erzeugt und die Wolke löst sich rasch auf.

Bei der Untersuchung des Energiespektrums zeigte sich, dass der Inertialbereich gut aus den Lidardaten abzuleiten war. Weitere Auswertungen der Energiespektren zu den bewölkten und unbewölkten Zeiträumen zeigen, dass eine Verschiebung der Wellenlänge mit der maximalen Energie stattfindet. Bei der unbewölkten Grenzschicht ist im Bereich von $0,5 - 0,7\ zi$ (Grenzschichthöhe) die größte normierte Maximal-Wellenlänge anzutreffen. Im bewölkten Bereich, verschiebt sich dies. Die Wellenlänge der maximalen Energie wird kürzer, die Energie verschiebt sich somit in den kleinskaligen Bereich der Turbulenz. Der Einfluss der aktiven Kumulus Wolken reicht somit bis in die Mitte der Grenzschicht hinein.

Die Datenbasis für die bewölkte konvektive Grenzschicht ist jedoch noch sehr klein, weitere Messungen auf diesem Gebiet sind daher nötig. Die ersten Ergebnisse sind jedoch sehr vielversprechend, so dass sehr wahrscheinlich neue Informationen über die turbulenten Prozesse in der bewölkten Grenzschicht erlangt werden können. Weitergehende Informationen insbesondere über Feuchte- und Wärmeflüsse können mit der simultanen Messung verschiedener Lidar Systeme (z.B. Raman oder DIAL) kombiniert mit Daten vom Wolkenradar erlangt werden. Die Kombination von Feuchte-, Temperatur- und Winddaten in der konvektiven Grenzschicht und in der Wolkenbasis können zum besseren Verständnis der Prozesse in der bewölkten konvektiven Grenzschicht beitragen, und z.B. im Hinblick auf die Modellierung wichtige Informationen zur Parametrisierung liefern.

Die Leistung des CLR WindTracer lidars war sehr zufriedenstellend. Es ist besonders geeignet, Messungen in der mittleren und oberen konvektiven Grenzschicht vorzunehmen. Im Bereich bis ca. 450m Höhe kann das Lidar nicht messen, dort kann gegebenenfalls eine Ergänzung mit Mastdaten erfolgen, wie sie auch für diese Arbeit verwendet wurden. Die Messungen und Aufzeichnung der Daten während des Messzeitraums für diese Diplomarbeit funktionierten zuverlässig. Für diese Arbeit wurden Daten mit 1 Hz aufgezeichnet, es ist jedoch möglich die Messung auf 10 Hz zu erhöhen. Das Doppler Lidar ist daher ein ideales Instrument für die Messung der Windgeschwindigkeit mit einer sehr hohen zeitlichen und räumlichen Auflösung.

Contents

1 Introduction

The greatest part of human life takes place on the earths surface. We therefore are constantly surrounded by the air of the planetary boundary layer. The characteristic of this part of the atmosphere is its turbulent nature. Different than in a laminar flow, eddies of all sizes occur in a turbulent flow (Fiedler and Panofsky, 1970).

Turbulence especially that driven by convection is of great importance to the life on earth. Convective turbulence is responsible for mixing over the full height of the planetary boundary layer, especially concerning trace elements and humidity. In convective situations even an exchange of air and trace elements between planetary boundary layer and free atmosphere is possible through thermals overshooting and penetrating through the capping inversion.

The investigation and measurement of the planetary boundary layer and turbulence has been made throughout the last century starting as early as 1915 with studies undertaken by Taylor. The biggest problem to date when doing measurements in the boundary layer with in-situ instruments is that only small portions of the planetary boundary layer can be measured. Using meteorological towers, as for example those in Cabauw (Ulden and Wieringa, 1996), FZK (Barthlott, 2003) or BAO-Boulder (Kaimal and Gaynor, 1982), only up to 300 m of the boundary layer can be measured. Aeroplanes can measure in greater heights, but only in one height at a time and only for a short time period. Radiosondes can measure the whole boundary layer depth but give only a snap shot of the current condition and time intervals can be several hours.

To obtain continuous measurements of the whole planetary boundary layer with a high temporal and spatial resolution remote sensing instruments are needed. The use of lidars is therefore ideal for these purposes. First use of the lidar technique started in the 1970s with CO_2 lasers. Today different lidar systems operate at various wavelengths, allowing atmospheric measurements of several variables.

In June 2004 the Institut für Meteorologie und Klimaforschung (IMK) at the Forschungszentrum Karslruhe (FZK)/Universität Karlsruhe put a new coherent Doppler lidar into operation. In the following months a series of measurements was conducted. These measurements included

comparison measurements with other instruments from the IMK (Wieser et al., 2005). As well as measurements on days with convection and convective driven turbulences with the lidar operating various different scanning techniques. These measurements took place at the Forschungszentrum Karlsruhe (FZK) 12 km north of Karlsruhe.

For this diploma thesis data mainly from the second part of the measurements in August 2004 at the FZK were used, containing data from different days, conditions and scanning modes.

The main objectives of this work was to characterise convective structures in the boundary layer (sub cloud layer) on days with shallow and deep convection. The comparison of the derived data with known theories in the literature (e.g. Caughey and Palmer, 1979), in order to determine if and how good the Doppler lidar is able to acquire these characteristics and to determine if the known theories are applicable in a convective boundary layer.

2 Turbulence in the Atmosphere

Turbulence is a type of motion in fluids or gases. It has an irregular, complex and unpredictable nature, is strongly rotational and chaotic. No common definition for turbulence can yet be given. But widespread agreement of some characteristics of the turbulent flow exist, these were described by Lumely and Panosfky (1964):

1. The fluid velocity is a chaotic and apparently random function of both space and time.
2. The flow is strongly rotational and three-dimensional, with gradients occurring in all directions.
3. Any two marked particles that are free to move within a turbulent environment tend to become increasingly distant from each other as time goes on.
4. Turbulence is dissipative. The energy of turbulence tends to shift from large well-organised eddies (small wave numbers) towards smaller eddies and eventually into molecular motions.
5. Gradients are created in the turbulent flow by stretching of vortices.
6. Turbulent flows are diffusive and intermittent.

These attributes can be observed by shedding a drop of ink into a pan of water that has been allowed to settle quietly for a few minutes. Due to the insertion momentum and density differences, turbulence is generated in the vicinity of the drop, which is readily seen, especially if good lightning is available. At first one sees that the initially concentrated blob begins to separate into a number of blobs connected by fine dark filaments, which become more and more elongated within a few seconds. As the volume spreads further, the dense filaments disappear, and the whole mass gradually enlarges itself becoming more and more diffuse until eventually it becomes unidentifiable. It is quite readily seen that all of the attributes enumerated above are present in this evolution. The filaments that form initially constitute vortex lines that elongate as time goes on and in doing so concentrate their vorticity (and marked fluid particles) into ever thinner diameters, until somewhat later molecular

motions cause the spinning structure to be dissipated and to disappear (Blackadar, 1997).

The quantitative approach to the study of turbulent fluids was begun in 1895 by Osborne Reynolds. He separated the velocity components into two parts, a mean value ($\overline{u}$, $\overline{v}$ and $\overline{w}$) and a turbulent portion denoted by u', v' and w'. The turbulent velocity defined by Reynolds therefore can be written as:

$$u = \overline{u} + u', \quad v = \overline{v} + v', \quad w = \overline{w} + w'. \tag{1}$$

First studies of turbulence were done for laboratory turbulence, which differs from atmospheric turbulence. The two main differences are that in the atmosphere heat convection coexists with mechanical turbulence and that the rotation of the earth becomes important for many problems. In 1915 Taylor was presumably the first meteorologist to become interested in turbulence.

In the beginnings turbulent transport was modelled in analogy to molecular transport and was assumed to be proportional to the large scale gradient. The coefficient of the proportionality, denoted by K (exchange coefficient) was given separate designations depending on the property being transported. In the early theories (e.g. Roberts, 1923) a constant K was assumed, later it turned out to be inappropriate for the atmosphere. In the 1930s, H. Lettau (1939) in Germany wrote the first book on atmospheric turbulence including quantitative expressions for wind profiles and fluxes. Rossby and Montgomery (1935) broke the tradition of a constant K. They produced the first realistic description of the distribution of wind in the whole planetary boundary layer. At about the same time a group of scientists around O. G. Sutton produced the first method of diffusion estimation, based on Taylor's (1921) diffusion theorem. The work was used well into the 1960 by the engineering community.

In the 1940s scientist in the Soviet Union started to take interest in the statistical structure of turbulence. Kolmogorov (1941) developed a theory of spectral forms. Monin and Obukhov (1954) developed a powerful technique for combining theories of mechanical and convective turbulence, the *Monin-Obukhov similarity theory*. This technique still

forms the foundation for the analysis of the surface layer, the lowest 10% of the turbulent boundary layer.

In the 1950s American scientists, influenced by the work of the statistician John W. Tukey, started to study the statistical properties of turbulence. Also in the 1950s large atmospheric experiments over nearly ideal terrain started. The first major experiment took place at O'Neill, Nebraska, in 1953 (Lettau and Davidson, 1957) concentrating on measurements of fluxes and profiles throughout the whole boundary layer, leading to the discovery of the low-level jet. The data was later also used to do studies on the convective unstable boundary layer (Carson, 1973). Around the same time C. H. B. Priestley (1959) in Australia suggested the existence of a free convection layer.

The 1960s saw the combination of the work of English, Soviet and American scientists in a series of articles and the book of Lumley and Panofsky (*Structure of Atmospheric Turbulence*, 1964). Further important field experiments were undertaken in this decade. In Australia W. Swinbank (1963) concentrated on fluxes whereas in the Kansas experiment directed by Haugen, Kaimal and Wyngaard (Haugen et al., 1971) the emphasis was on statistical properties such as spectra and cospectra. The results gained in the Kansas experiment still form the basis of applied work at this time. Also in the 1960s, the effects of roughness change and surface temperature change on atmospheric flow became better understood. V. Tatarskii of the Soviet Academy of Sciences published the first book on the interaction of electromagnetic waves and sound with atmospheric turbulence. This volume is still the basic in the study of remote sensing and of wave propagation through the atmosphere.

In the 1970s the major progress involved the extension of theory and observation to higher levels. Important field experiments over smooth and rough terrain took place in Australia, the Soviet Union and North America, involving measurements throughout the turbulent mixing layer. The Minnesota experiment in 1973 (Kaimal et al. 1976) and measurements during 1976 in Ashchurch (Caughey and Palmer 1979) provided data for the depth of the convective boundary layer. Deardorff (1972) and others introduced mixed-layer scaling which was successful in accounting for many of the properties of the daytime boundary layer.

The 1980s saw further complex-terrain studies. Major progress was made in theory and observation of flow across sea-land boundaries, gravity flow

and flow over hills. Especially the ASCOT experiments (**A**tmospheric **S**tudies in **Co**mplex **T**errain) from 1979 to 1984 (Clemets et al., 1989) provided information about drainage flows in mountain valleys. The MESOKLIP experiment (Fiedler and Prenosil, 1980) combined complex-terrain studies with mesoscale climate development. Diffusion experiments were made over cities and various types of complex-terrain. For these experiments more and more remote sensing instruments such as sodars, lidars and radars were used and combined with in-situ measurements. Especially lidar measurements became more important during the 1980s (Neff, 1990). In the same decade the investigation of convective structures and the cloud toped boundary layer took place (Driedonks and Dynkerke, 1989).

The 1980s and 90s also saw a significant increase of computer power which opened the possibility of turbulence modelling to a much wider field of applicants. Major advances in the knowledge of the boundary layer structure haven taken place due to the numerical modelling. But despite all the efforts there are still large gaps especially concerning higher order closer theories. Also heterogeneous surfaces and stable layering hold unanswered questions.

3 General description

3.1 Measurement site

The Forschungszentrum Karlsruhe (FZK) is situated 12 km north of the city of Karlsruhe in southern Germany. The coherent Doppler lidar of the Institut für Meteorologie und Klimaforschung (IMK) at the FZK was situated in the north eastern part of the FZK at $8°26'20''$ E and $49°06'00''$ N at 110 m above sea level. The 200 m mast which provided data for the lower part of the atmospheric boundary layer is situated at the south westerly tip of the FZK approx. 1.4 km away from the lidar (Fig. 1).

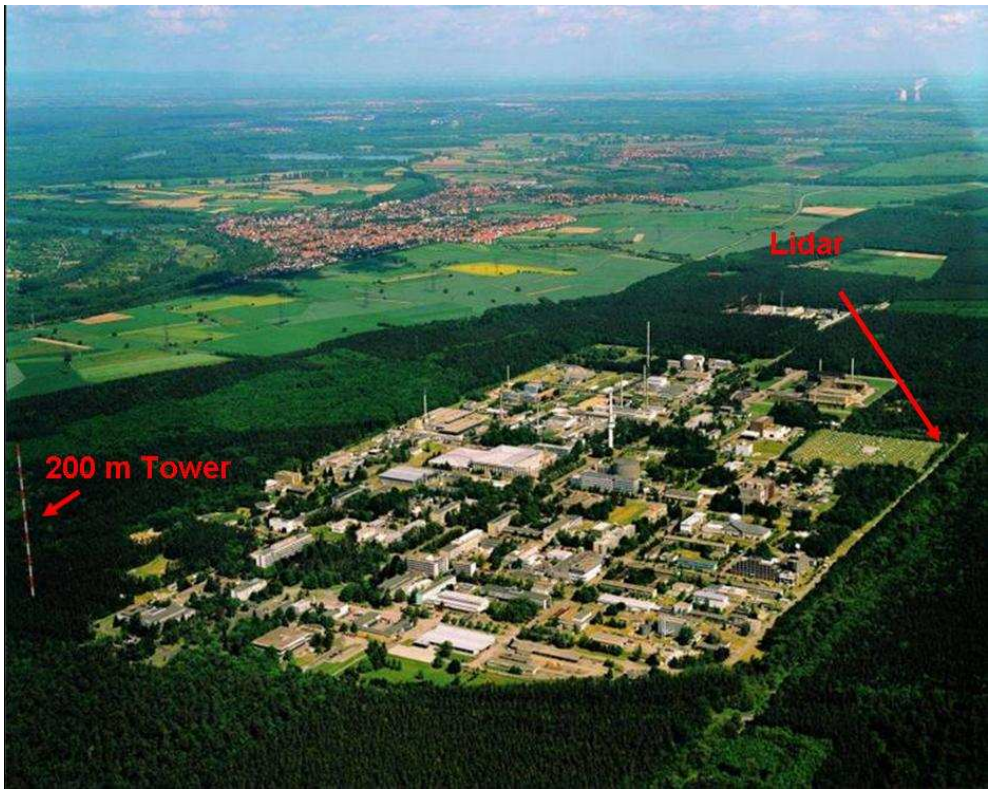

Figure 1: Aerial picture of the FZK, with the lidar in the north east, the instrument field and the 200 m mast in the south westerly corner.

The research centre is surrounded by woodland. The site of the lidar is grassland open to the south west and closed in by trees on the north east. The main wind direction normally is from the south west due to the channelling effect of the Rhine valley (Kalthoff and Vogel, 1992). The 200 m tower is surrounded by trees, so the lower heights of measurement are within the forest. The global radiation is recorded next to the tower

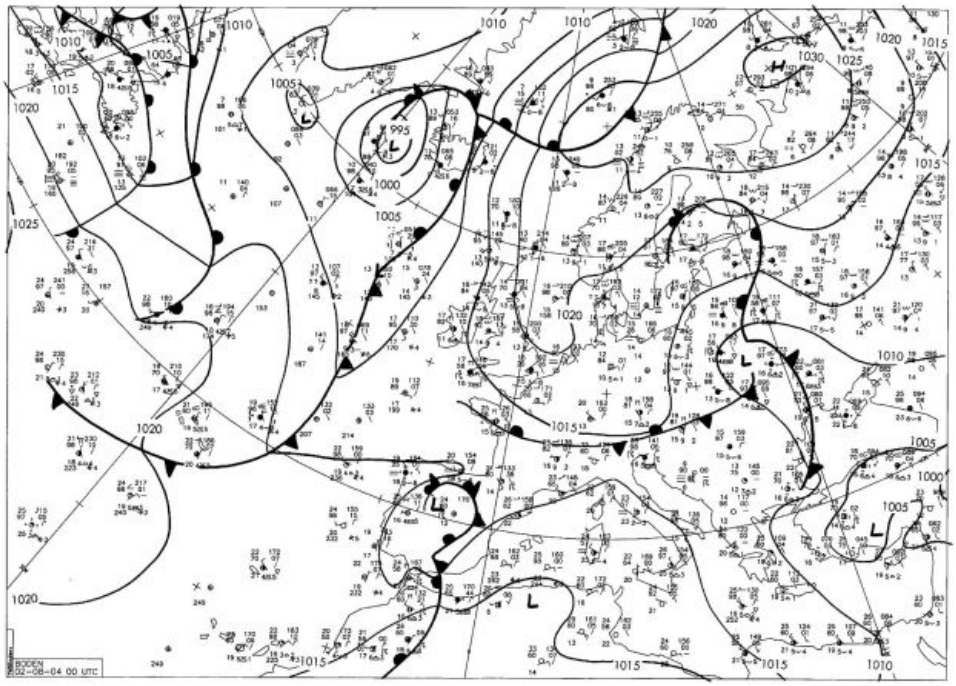

Figure 2: Surface pressure in Europe on August 2, 2004

on a field, in the early morning hours the data can be influenced by the shadows of surrounding trees, but during the day there is no interference.

3.2 Weather situation

After installing the lidar in June 2004 measurements were undertaken throughout the summer and autumn until October 2004. First measurements where done with the lidar group from the Arizona State University in order to obtain a data set for the comparison with other instruments such as a radar profiler, the 200 m tower, tethersondes, radiosondes and a sodar. In the following different scan strategies and instrument settings were tested. The data collected during this part of the summer was mainly used for this diploma thesis.

Data from two days was looked at more closely. This was firstly August 2, 2004 with the lidar operating a vertical stare. This data is described in chapter 7 and 8. The weather in Central Europe was influenced by a high pressure system over northern Scandinavia and a low pressure system over Eastern Europe (Fig. 2). A new low pressure system was developing just west of Iceland. Germany was in the lee of a cold front

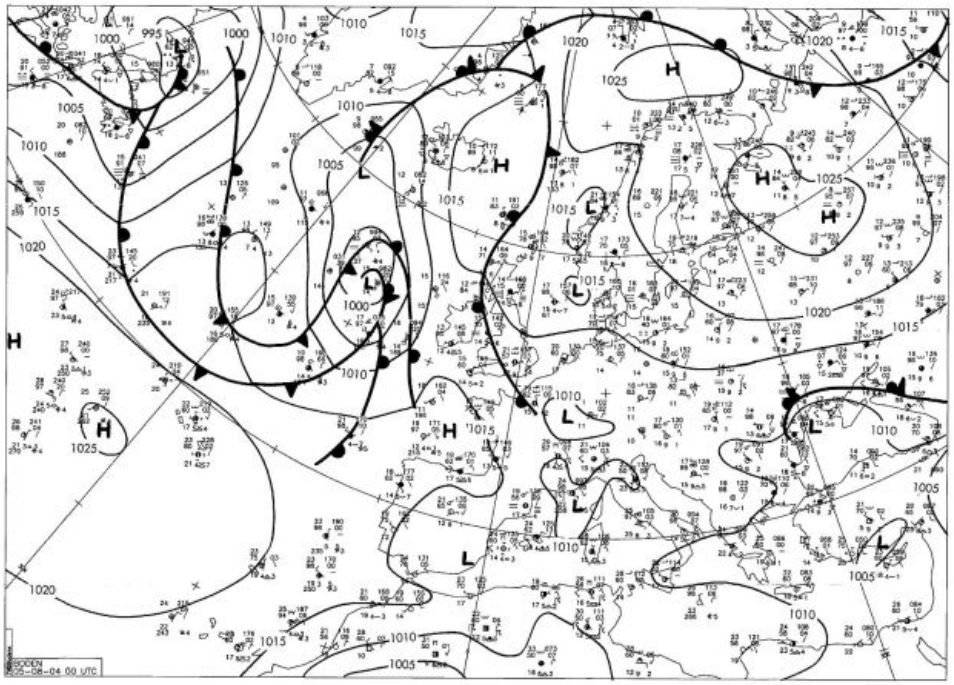

Figure 3: Surface pressure in Europe on August 5, 2004

that had passed over the day before from the north. A high pressure system near the ground was slowly developing in Central Europe. During the day the winds at the FZK came from easterly directions, turning to north for a couple of hours during the late afternoon. In all the horizontal wind speeds were rather low at $4 - 5\ m\,s^{-1}$ in $100\ m$ above ground. No or just scattered clouds were recorded with sunshine of 13.6 hours and a maximum temperature of $31.6°\ C$.

The second day was August 5, 2004 with the lidar operating **p**lan **p**osition **i**ndicator (ppi) scans at five different elevations. The data is described in chapter 6. The weather had not changed significantly during the days of August 3 and 4. The Scandinavian high had moved south into Eastern Europe eroding the low pressure system (Fig. 3). The Iceland low had deepened and moved out onto the Atlantic. In Central Europe a surface near low pressure system started to develop but was eroded by the high pressure over Eastern Europe soon afterwards. The winds picked up a little, now being at $5 - 6\ m\,s^{-1}$ and coming from the east during the whole day. No significant cloud cover could be recorded. Sunshine was recorded for 12.7 hours and the maximum temperature rose to $37.4°\ C$.

4 LIDAR - Light Detecting And Ranging

The lidar belongs to the group of active remote sensing instruments. The abbreviation LIDAR stands for Light Detecting and Ranging. Thus every lidar operates a laser, with which it probes the atmosphere. Different wavelengths allow the measuring of different characteristics. Most common lidars are for example Doppler lidars, as was used for this work, which can measure wind speeds due to the doppler shift of the laser light reflected by aerosols, Raman lidars which measure the water vapour and trace gases in the atmosphere, using the raman scattering effect, and differential absorption lidars (DIAL), measuring water vapour and other gases through absorption of the laser light.

Since only small portions of the laser light travelling away from the lidar will be reflected back to the lidar into the atmosphere and can then be recorded (Fig. 4) high power lasers are necessary. Therefore pulsed lasers are used.

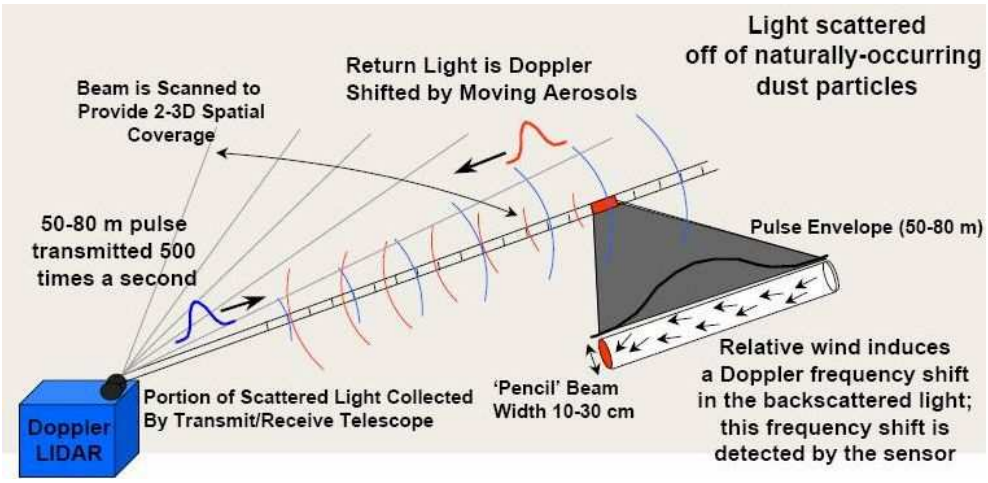

Figure 4: Operation principle for a Doppler lidar (CLR Photonics, 2002)

4.1 Different laser types

For a Doppler lidar the laser wave length has to be in a region of the atmospheric window, so the light will not be absorbed by water vapour or other atmospheric gases for example CO_2. Desirable would be a laser in the eye safe region i.e. a wave length above 1.4 μm. On the other hand the wave length should not be too big, as the light has to be scattered by aerosols.

In the past different types of laser systems have been developed. First lidar systems were based on CO_2 lasers. One of the first systems was developed in the late 1970s at the NOAA Wave Propagation Laboratory (Post et. al 1981 and Post and Cupp, 1990). The major drawbacks of CO_2 laser systems are the frequency instability due to turbulence in the gas flow, the size of the gas cells and the high power consumption.

Therefore solid-state lasers were used more and more for Doppler lidar applications. Probably the first Doppler lidar using a solid-state laser was developed at Stanford University in 1987 (Kane et al. 1987). This system was operating a pulsed, flash pumped Neodym (Nd):Yttrium Aluminum Garnet (YAG) laser. But the wave length of this laser was not eye safe and very sensitive to atmospheric turbulence, which meant that further improvements had to be made. At the Max-Planck-Institute for Meteorology (MPI) a Nd:YAG laser at 1.2 μm was developed. This system allowed simultaneous measurements of water vapour (differential absorption lidar – DIAL) and wind speed (Linne and Bösenberg 2003). But this laser was still not eye safe.

Other solid-state lasers are Ytterbium(Yb):YAG lasers combined with periodically poled Lithium Niobate (PPLN). A wave length of 1.55 μm was reached (Sridharan et al. 2003), allowing measurements in the eye safe region. Also fiber lasers have been tested for Doppler lidars, but the pulse energy was very low, so that measurements were limited to a range of 300 m (Pearson et al. 2002).

A breakthrough in the search for eye safe lasers came with the discovery and composition of Thullium (Tm) and Holmium (Ho). Using YAG as a host material very good performances have been achieved (Bollig et al. 1998). The first 2 μm coherent Doppler lidar system based on Tm:YAG was demonstrated by Henderson et al. (1991). At the NOAA Environmental Technology Laboratory a 2 μm system was developed and optimised for the high resolution wind measurements in the lower troposphere. The design of the transmitter and receiver of this so called High Resolution Doppler Lidar (HRDL) is shown in Figure 5 and described by Grund et al. (2000). The Doppler lidar used by the IMK was developed using the same technique as the HRDL.

In addition to lasers using aerosol backscatter, lidars using a laser in the short range spectrum (e.g. 355 nm, also eye safe) have been developed in recent years (Flesia et. al, 2000 and Gentry et al., 2000). These

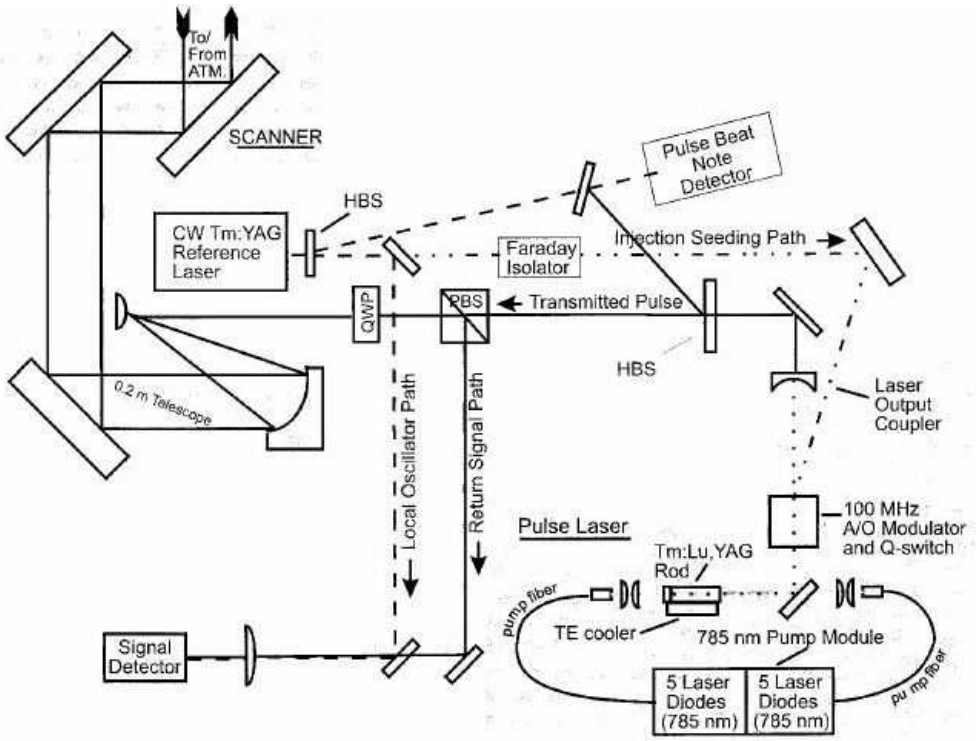

Figure 5: HRDL transmitter schematic (Grund et al., 2000).

lasers scatter on molecules rather than aerosols. Molecule-backscatter lidars can be used for wind measuring in areas with no or low aerosol concentration, such as the Southern Hemisphere or mid-oceanic regions. Molecule scattering is ideal for satellite-based wind measurements.

4.2 The Doppler lidar technique

The heart of every lidar system is the laser. It's technical specifications such as wavelength, pulse repetition frequency, sampling rate etc. decide which parameters can be measured. At the other end is the receiver, which is responsible for detecting the backscattered light. Time and spatial resolution as well as the measuring range depend on its configuration.

For Doppler lidars every laser beam is divided up into a number of range gates (Fig. 4). This is necessary to get a certain number of measurements to perform a fast fourier transformation converting the frequency to wind speed. Other lidar systems can operate without range gates as they do not have to perform a fast fourier transformation. Due to the time difference between emitting and receiving the laser pulse the distance of the reflecting aerosol to the lidar can be calculated. In this way every

value can be assigned a specific range gate.

To measure wind speeds the difference in frequency of the original pulse and the returned light is measured. This so called Doppler shift (hence the name Doppler lidar), after the Austrian mathematician and physicist Christian Doppler (1803-1853), is induced by the velocity of the particles towards or away from the lidar. This shift in frequency can be directly transformed to radial velocity of the particles. The Doppler frequency shift is

$$\Delta\nu = \frac{-2v_r}{\lambda} \tag{2}$$

with λ being the wavelength and v_r the radial velocity. For an operating wavelength of 2 μm the frequency shift is approx. 1 MHz per $m\,s^{-1}$.

A lidar can only measure along the path of the laser beam, this means that for example wind components orthogonal to the beam can not be measured. There are methods (e.g. the VAD algorithm) to calculate the three dimensional wind vector, as described in chapter 5. To get a signal the Doppler lidar with an eye safe laser (wavelength $>$ 1.4 μm) needs aerosols in the atmosphere to return a portion of the light but on the other hand too many aerosols or water drops scatter and attenuate the light so much, that a correct signal can not be received.

Usually Doppler lidars have a scanner which enables them to operate various scan modes and not just measure with fixed beams. There are two basic types of scans that are common for ground based lidar applications. One is called a ppi-scan (**p**lan **p**osition **i**ndicator) and does an azimuth sweep of 360° at a fixed elevation (Rinhart, 1991). This scan type will be mainly used later in this work. The ppi scans used for this work were obtained rotating the scanner with a speed of $6°s^{-1}$ in the azimuth direction. This way one ppi scan takes one minute and consists of roughly 550 individual beams.

The second common scan type is the rhi-scan (**r**ange **h**eight **i**ndicator), this scans a slice of the atmosphere over the zenith at a fixed azimuth angle.

4.3 The CLR Photonics Doppler lidar

The CLR Photonics Wind Tracer a coherent Doppler lidar comes in its own shelter (Fig. 6), which includes all necessary equipment to operate the lidar system, such as the transceiver, the control units, real time signal processor and the data storage. On top of the container a two axis scanner is fixed, which directs the laser beam by two planar mirrors into the atmosphere, a video camera is also included. A UPS (Uninterruptible Power Supply) provides short term (5-10 minutes) backup power to all the subsystems. This enables the lidar to operate continuously through short power losses. After 15 minutes without power the lidar will shut down automatically.

The single most important unit in the container is probably the MAG 1A transceiver. Within it the laser pulse is created and emitted, and the returning signal is received and then transmitted to the signal processing subsystem. The transmitter consists of three parts (Fig. 7). The local oscillator (LO) or master laser, a continuous wave (cw) laser, which provides a stable frequency reference standard. Secondly the pump laser for the laser transmitter. The transmitter or slave laser converts the light of the pump laser to the frequency region of interest. The slave laser is controlled by the master laser using the injection seeding technique.

The CLR Photonics Wind Tracer Doppler lidar uses a pulsed laser with a Pulse Repetition Frequency (PRF) of 500 Hz. This means that every 2 milliseconds a laser pulse of 425 ns is transmitted into the atmosphere which is $50-80$ m long and $10-30$ cm wide, depending on the distance from the lidar.

To acquire data the data acquisition system stores a 'copy', the so called Monitor pulse, of the laser pulse being transmitted. This 'copy' holds information on frequency and time of the transmitted laser. Shortly afterwards the atmospheric returns are recorded in the Signal Block (Fig. 8). The RF or Q-Switch is responsible for triggering the laser pulse. The data then is analysed using the Monitor Block as reference to determine radial velocity and distance of aerosols.

The system has a sampling rate of 10 nanoseconds, this corresponds to a sampling distance of 1.5 m. To perform a fast fourier transformation a minimum of 48 sampling points are needed. Normally the system operates with 60 points. To receive a reliable value the acquisition system

Figure 6: The CLR Photonics Wind Tracer a coherent Doppler lidar, at its site at the FZK.

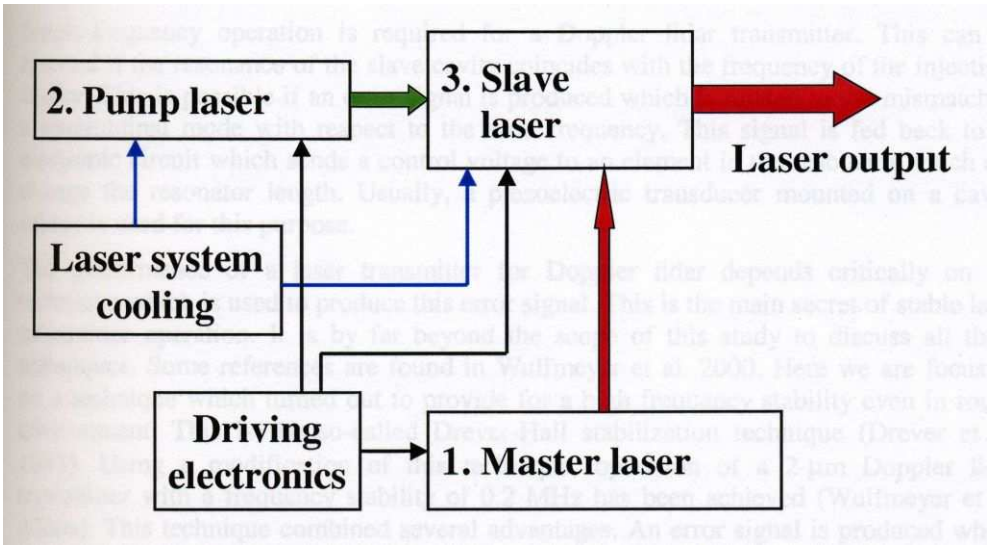

Figure 7: Set up of the Doppler lidar laser transmitter (Wulfmeyer et al., 2003)

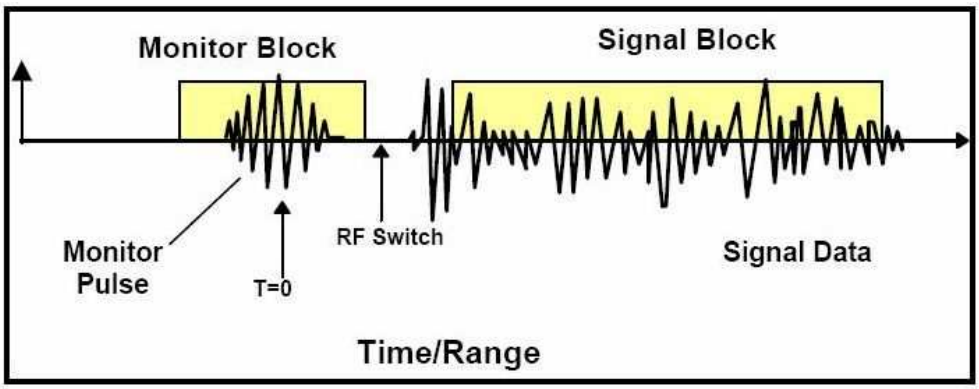

Figure 8: Data sampling with Monitor Block and Signal Block (CLR Photonics, 2002)

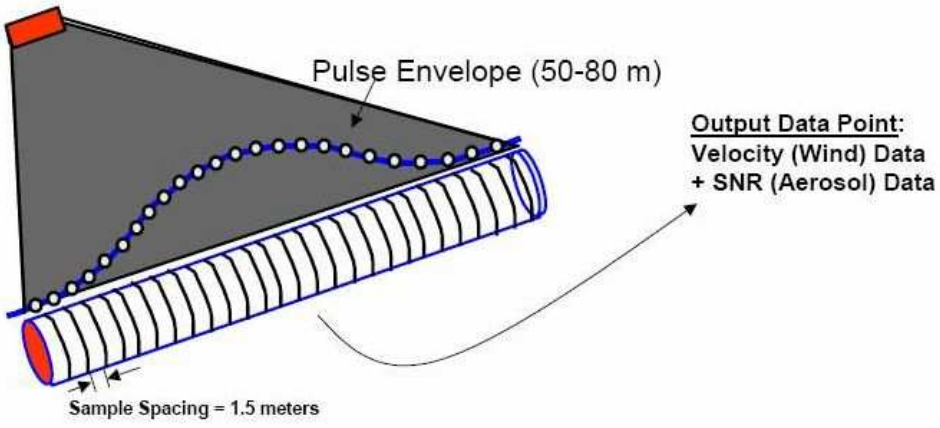

Figure 9: Data acquisition by performing a fast fourier transformation over the whole range gate. Each range gate consists of a number of data points (CLR Photonics, 2002).

performs a fast fourier transformation over a complete range gate, performs a fit and uses the maximum gained from the fitted data (Fig. 9). The length and the position of the range gates can be set up as needed for the measurements.

The wavelength of the laser used by the WindTracer is 2 μm, which means that the laser light is in the near infrared and therefore invisible for the naked eye. The light scatters on particles that are $0.5 - 1$ μm in diameter and larger. With the wavelength being larger than 1.4 μm the laser is considered to be in the 'eye safe' region.

The receiver is situated in the same module as the laser and receives the reflected laser light. It then transmits the signals to the Analog Front End (AFE). The AFE has two processing bandwidth modes one with 50 MHz and one with 100 MHz. By changing between these modes a measurement range of ± 20 $m\,s^{-1}$ or ± 40 $m\,s^{-1}$ can be chosen. In the AFE the signal is filtered and amplified and then sent on to the Real Time Advanced Signal Processor (RASP-VME). Here the conditioned signals are processed to generate range-resolved Doppler spectra, from which radial velocity, spectral width and signal to noise ratio (SNR) are derived. Normally only the products of the Real Time Advanced Signal Processor are stored. The system however has the possibility to also store the original data for reprocessing or off-line processing purposes, but this takes up too much disk space, so they are generally discarded.

The two axis scanner covers a whole hemisphere with azimuth angles from 0 to 360° and elevation from -5 to 185°. The scanner resolution

Table 1: The MAG 1A Transceiver

Laser	
Wavelength	2.0225 μm (eye safe)
Pulse energy	2 mJ
Pulse width	425 ns
Pulse repetition frequency	500 Hz
Receiver	
Bandwidth	50/100 MHz
Sampling frequency	100 MHz
Resolution	8 bit
Scanner	
Beam diameter	8 cm
Azimuth (range, step, speed)	360°, 0.01°, 25° s^{-1}
Elevation (range, step, speed)	190°, 0.01°, 25° s^{-1}
Output	
Range gates	120
Range (min, max)	400 m, $>$ 8500 m
Range resolution	$80 - 100$ m
Velocity range	± 20 / ± 40 $m\,s^{-1}$
Velocity resolution	0.5 $m\,s^{-1}$
Update frequency (LOS)	10 Hz

is 0.01° in azimuth and elevation and can scan with a speed of up to 25° s^{-1}. Through bigger window in the scanner (Fig. 6) the laser is directed, behind the smaller window the video camera is situated.

5 The Velocity Azimuth Display Algorithm

As described in chapter 4 the Doppler lidar can only measure wind speeds along the path of the laser beam. This means for a vertical looking lidar it measures the vertical wind speed component w, the other two components u and v can not be measured. Measuring with a fixed beam one can not determine the single wind speed components without additional information.

To calculate all three wind components from the radial wind velocity of a fixed beam information of two wind components near the beam at the desired range gate are needed. The obvious drawback is, that additional information at every range gate would be needed.

For measurements that include scanning other methods are available. One possibility would be to use three different lidars positioned in a triangle, which then measure the same area at the same time. With radial velocities from three different directions all three components can be calculated. The fact that lidar instruments are still today not often used and are quite expensive, together with the relative short range of these instruments, this method is rarely if ever used.

The most common used method comes from the radar meteorology and is called the **V**elocity **A**zimuth **D**isplay (VAD) algorithm (Browning and Wexler, 1968 and Lhermitte and Atlas, 1961). The idea is to retrieve the three wind components u, v and w from a single radar or lidar operating a ppi scan (see chapter 4.3). To do this it has to be assumed that the horizontal wind is homogenous and constant in time for the duration of one ppi scan. If the ppi scan is then plotted from 0 to 360° on the x-axis and the radial velocity on the y-axis, a sinus formed wave of the radial velocity will be received (Fig. 10). The phase then gives the wind direction (with the minimum being where the wind comes from). The amplitude gives the horizontal wind speed (Fig. 11). From these two values u and v can be calculated. The w component can be taken from the off-set on the y-axis.

This provides an average wind vector for range gate of one ppi scan. For turbulence discussions an average w component is not ideal. For this reason the influence of horizontal wind was subtracted from the measured radial wind velocities, leaving the vertical wind component for

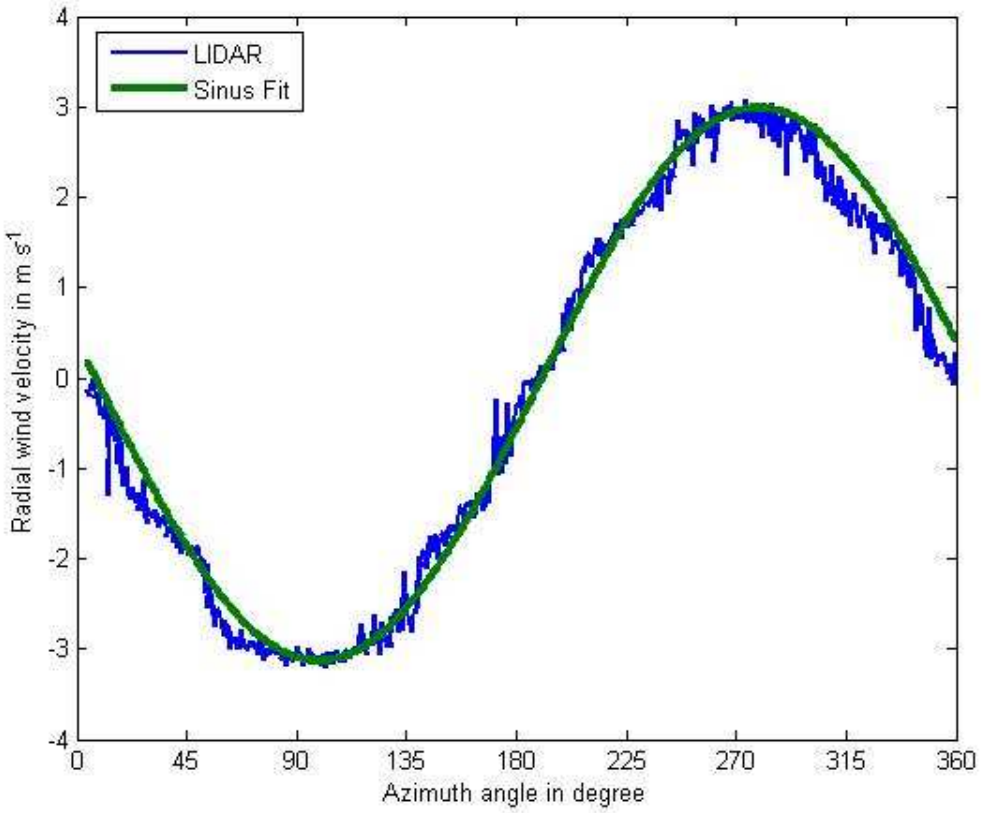

Figure 10: Radial wind velocity of a ppi scan at an elevation of 74° at 08:05 UTC on the 5^{th} August 2004 for range gate 15.

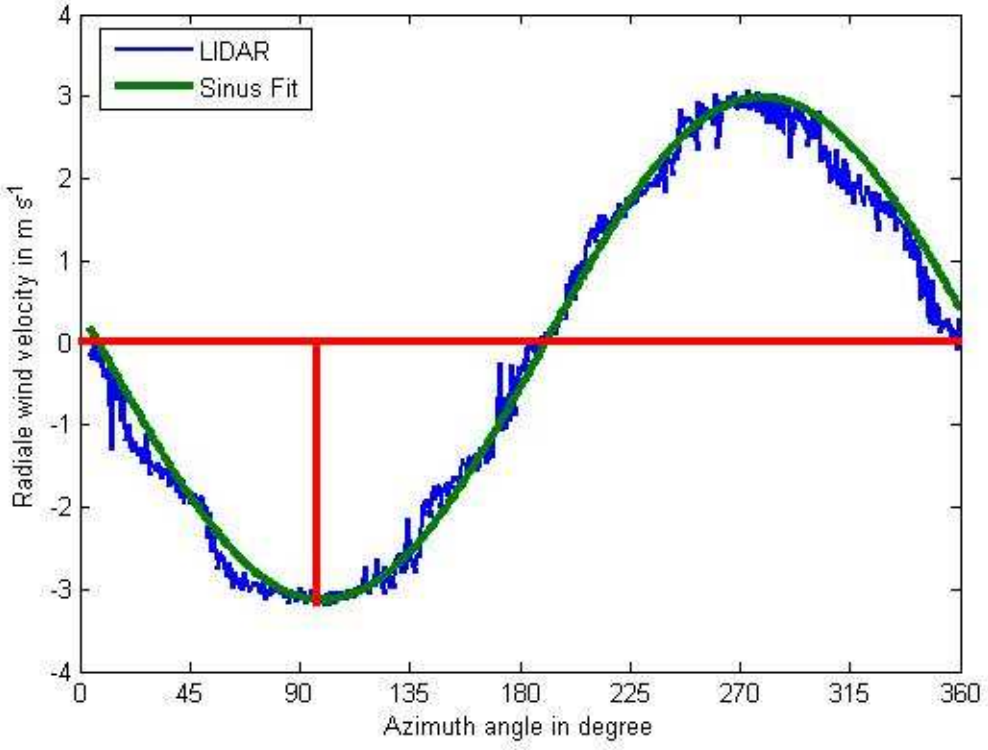

Figure 11: Radial wind velocity of a ppi scan at an elevation of 74° at 08:05 UTC on the 5^{th} August 2004 for range gate 15. The Red line marking the direction of the horizontal wind

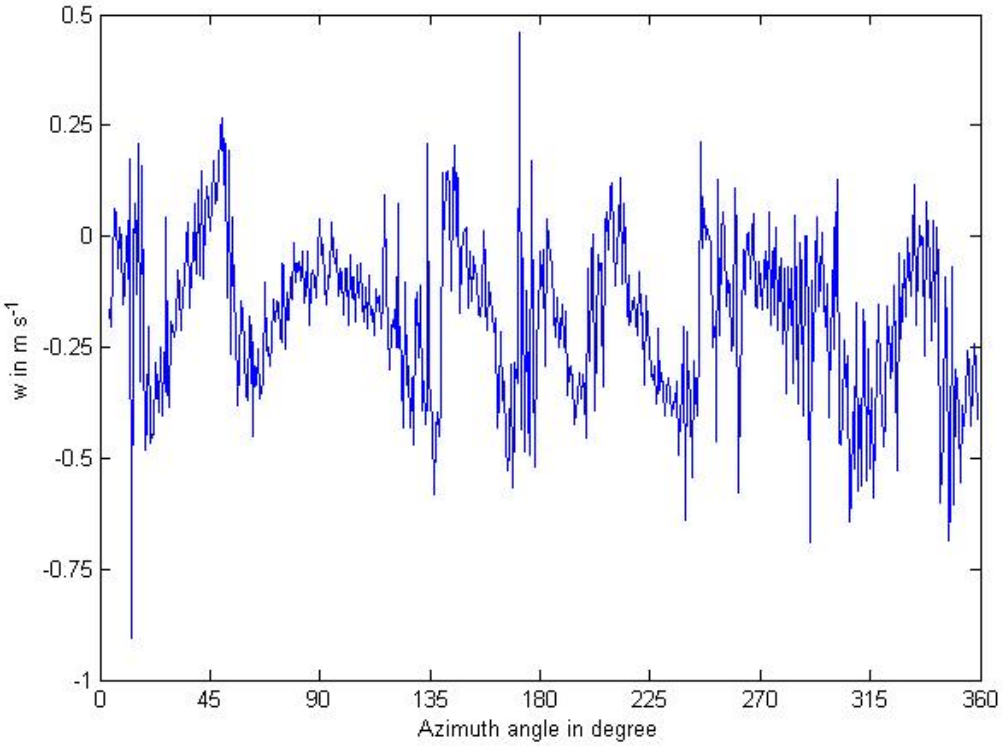

Figure 12: Vertical wind speed for a ppi scan after subtracting the influence of horizontal wind on the radial wind velocity.

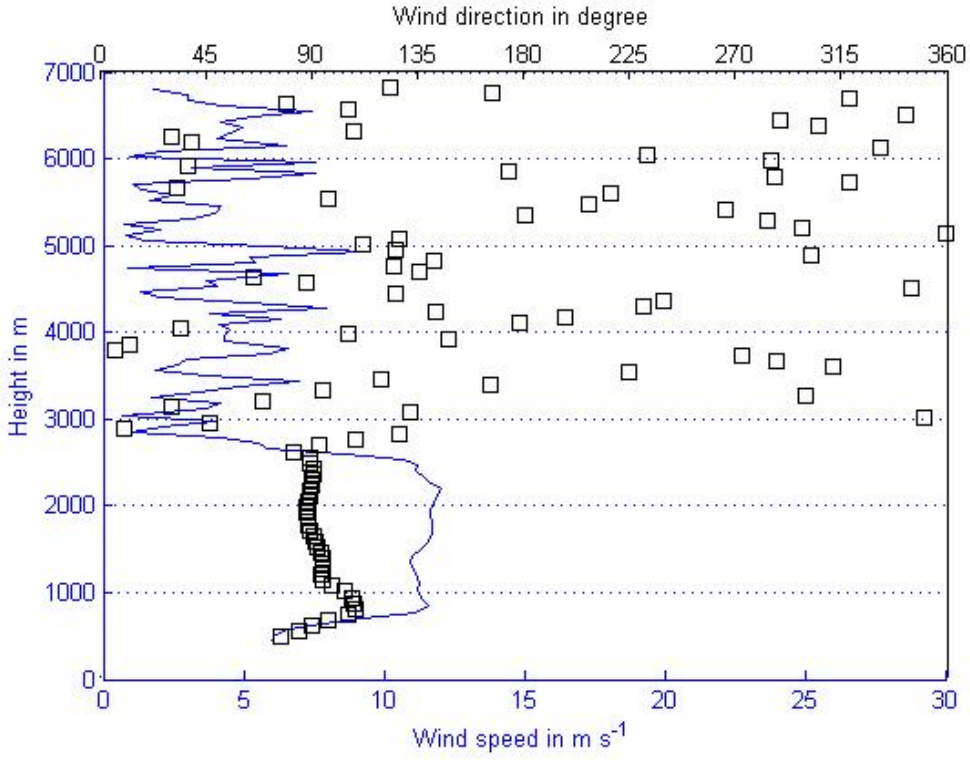

Figure 13: Vertical profile of horizontal wind speed (solid line) and direction (squares).

every single beam. This gives a distribution of the vertical wind at one range gate for the ppi scan. Figure 12 shows this for the morning of August 5 2004.

As described above the horizontal wind speed and direction is gained for every range gate of a ppi scan. As every range gate is at a different height a vertical profile of wind speed and direction can be obtained (Fig. 13).

6 Graphical display of turbulent structures

The measurements from the August 4 to August 8, 2004 at the Forschungszentrum Karlsruhe where used in this chapter. The idea was that with a series of scans turbulent structures could be identified, first manually later perhaps automatically, and followed on their way through the atmosphere. For this purpose a series of ppi scans was performed. One complete set consisted of 5 ppi scans at elevations of 88, 86, 82, 78 and 74°. The scanning speed was 6° per second, which results in one minute per ppi scan or five minutes for the whole set. The recording rate was set at 10 Hz so each ppi scan consist of approx. 550 individual measurement (beams). Due to the programming of the scanner some values at the beginning and end of each ppi scan were not used.

The measurements produced sets of radial velocities. Using the VAD algorithm (see chapter 5) mean values for u, v and w for every ppi scan were calculated. To evaluate turbulence a mean w value over one minute is not very good and has the drawback of having only one value for the whole ppi scan. With a low elevation angle and at greater heights the diameter of one ppi scan can span several hundred metres. In the example given later in the text the diameter at an elevation of 74° is 400 m. To achieve a better spatial resolution the w component for each beam was calculated by subtracting the mean horizontal wind from the radial wind velocity of every beam leaving just the w component. This way for every ppi scan at every range gate and every beam an individual w component was received. The clear advantage using this method is that a high time and spatial resolution of the vertical wind is received. Problems could occur when the horizontal wind does not comply with the conditions stated in chapter 5.

Every ppi scan was done with a different elevation, which means that the height of the range gates is different for every scan. For the used elevations the height in range gate 6, which will be used later in this chapter, ranged from 711 m for an elevation of 74° to 739 m for an elevation angle of 88°. The height of range gate 7 for an elevation angle of 74° is 776 m. Thus at this height using the same range gate the height difference is only 28 m compared to 37 m when using data from two range gates.

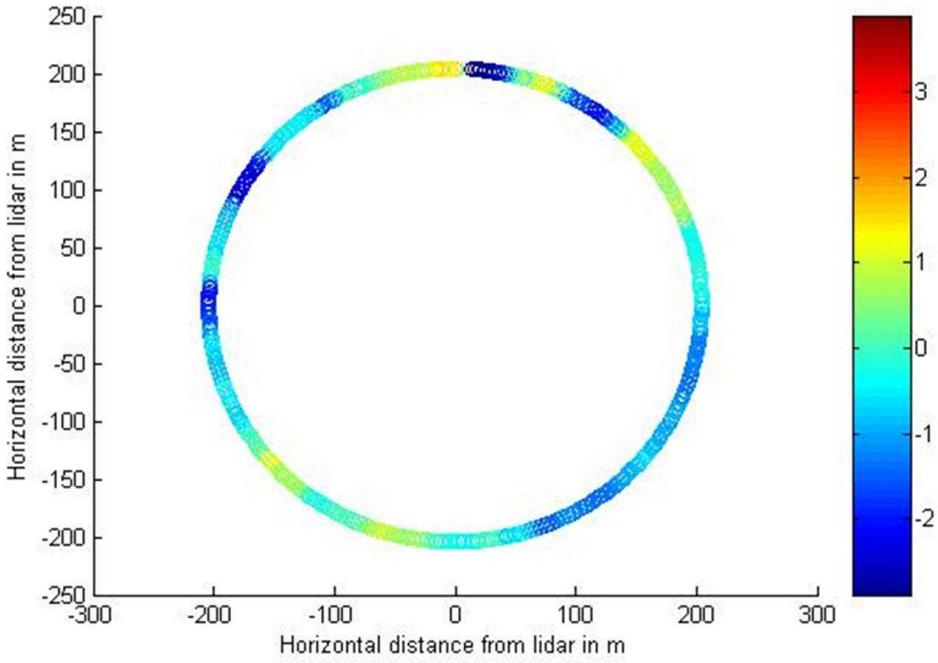

Figure 14: Vertical wind speed in $m\,s^{-1}$ for one ppi scan, at 74° elevation, August 5th 2004 at 12:10 UTC

6.1 Plan view of vertical winds

The question of how to display the vertical winds was to be answered next. A display as shown in Figure 12 is alright for one ppi scan, but here a set of 5 scans has to be displayed, including the spatial distribution, as every scan has a different distance from the lidar. A plan view for the ppi scans was chosen (Fig. 14), this way not only the values (colour) but also the spatial information could be displayed. Figure 15 shows all five scans in one plot.

The plots in Figure 14 and 15 show the vertical wind component where it was measured. To identify turbulent structures more information of the space in between the single scans is needed. For this reason an interpolation was done. A grid of 600x600 points was created and for every point a w value was calculated. For the interpolation the MATLAB function griddata with the triangle-based linear interpolation was used. The interpolation method is based on the Delaunay triangulation of the data that uses Qhull (University of Minesota, 1993).

In Figure 16 the result of the interpolation process is displayed. Some structures can clearly be identified. Especially in the centre near the lidar, where more data is available, structure with upward motion and

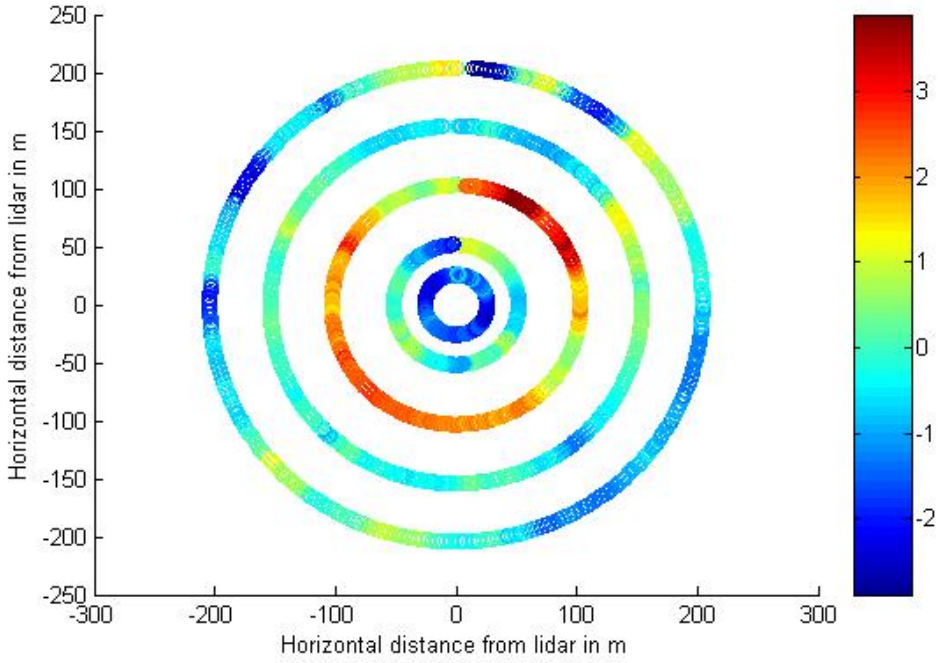

Figure 15: Vertical wind speed in $m\,s^{-1}$ for five ppi scans, elevation between 88 and 74°, August 5th 2004 at 12:10 UTC

areas of down drafts can be registered. Towards the edges at distances of more than 200 m from the lidar, the data is extrapolated and can not be used for interpretation. The regions outside the black ring in figure 16 have to be excluded as these values are only due to interpolation effects.

6.2 The influence of the horizontal wind

Displaying the vertical wind component as done in section 6.1 assumes that the structures do not change position during the duration of the 5 scans. As it is very unlikely that no movement occurs in the atmosphere for 5 minutes the, influence of the horizontal wind has to be taken into account. To do this a horizontal drift was calculated for every scan.

An average horizontal wind speed and direction was calculated from the scans at 82, 76 and 74°, at the respective range gate. Because of the small contribution of the horizontal wind on the radial velocity at elevations 88 and 86° of only 2.2 and 4.4% these values were not used for calculating the average horizontal wind. The position of every scan was now calculated including the drift induced by the horizontal wind. This gives a set of five rings spread along the axis of the mean wind direction (Fig. 17). Even for those times when the mean wind speed

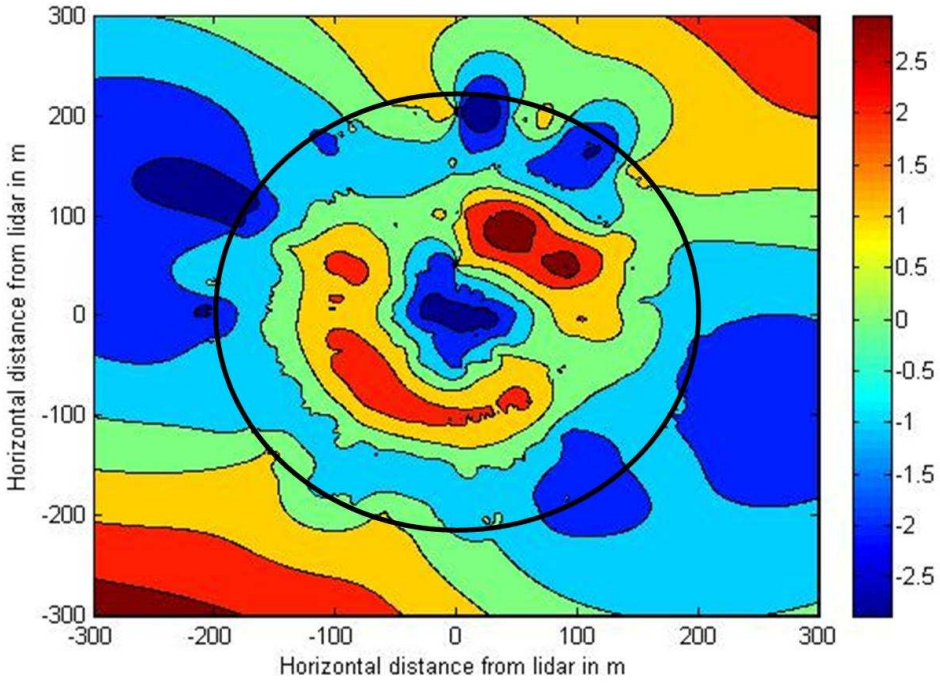

Figure 16: Interpolation of the vertical wind of five ppi scans on a 600x600 grid. Solid black ring indicates the outmost ppi scan of the lidar. Vertical wind speed in $m\,s^{-1}$.

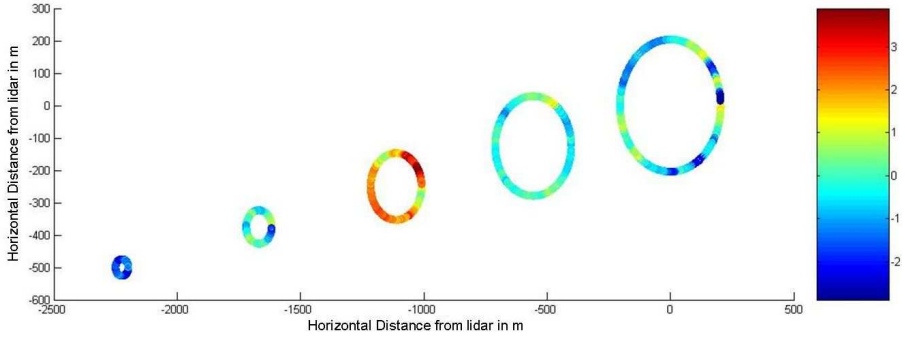

Figure 17: "Drift" of five ppi scans of the vertical wind. Vertical wind speed in $m\,s^{-1}$.

at the investigated height was relatively low ($< 7\ m\,s^{-1}$), the distance between the individual scans was so big that not even the two scans from the lowest elevation angle (76 and 74°) covered partly the same area.

To complete the discussion an interpolation was done for the drifted scans, using the same method as above but with a bigger grid (Fig. 18). As expected the results are not very realistic, as the distance between the scans and therefore the single measurements is far too large so no sensible interpolation could be performed.

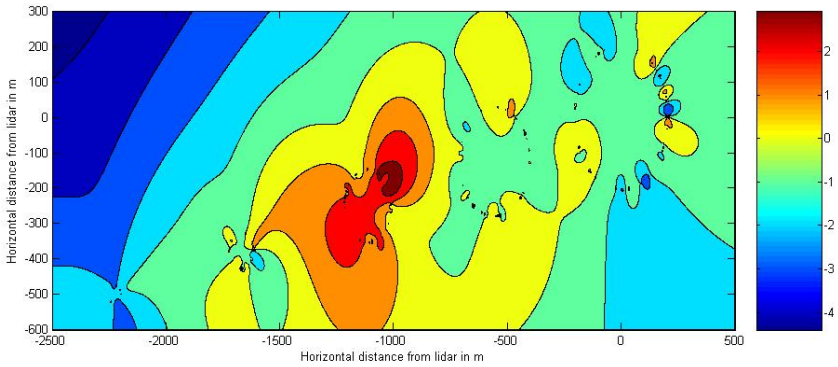

Figure 18: Interpolation of the "drift" of five ppi scans of the vertical wind. Vertical wind speed in $m\,s^{-1}$.

6.3 Other scan strategies

When displaying turbulent structures the following considerations have to be taken into account. The time for the individual scans should be as short as possible. The horizontal scan speed of 6° per second is far to slow, a speed of approx. 20° per second should be tried. Also the elevation angles have to be reconsidered. The data from two elevations nearest to the zenith (88° and 86°) is to be treated with extreme caution, as it is questionable if the application of the VAD algorithm is justified with high elevations like this. The w component is calculated by subtracting the horizontal wind speed, but as mentioned above at these elevations the influence of the horizontal wind speed is below 5%, so that the measured radial velocity is dominated by the w component. This holds the risk when using the data that the horizontal wind speed is overestimated. Also the area covered by these two scans is very small and the risk of using incorrect values is bigger than the information gained. Therefore only elevation angles less than 80° should be used.

The knowledge of the horizontal drift of the turbulent structures is very important. The scanning time for a sensible number of ppi scans is far too long that the drift could be neglected. It is not certain whether the structures travel with the same speed as the horizontal wind. One thought that stands against this is that eddies can have a diameter of more than one hundred metres in vertical direction, the wind shear over this length is so large, that if the eddies would always travel and at all heights with the average horizontal wind speed at that height they would be torn apart very quickly, as the wind speed varies at different heights.

Perhaps a completely different scan strategy would be more successful.

Doing rhi scans orthogonal to the main horizontal wind direction, letting the structures drift past the lidar would be an alternative. This would also mean that no horizontal wind components are measured, so only the vertical wind would contribute to the radial wind velocity.

For this scan strategy the main horizontal wind direction has to be measured regularly, e.g. every 10 min when significant changes occur or every 30 min when the mean wind direction is stable. In the mean time rhi scans orthogonal to the horizontal wind direction can be performed. For a higher temporal resolution only a half rhi scan could be done. This would be practical if e.g. the view to one side is blocked by buildings or vegetation. To get a larger amount of data a complete rhi scan is preferable. This way the atmosphere to both sides of the lidar can be measured, with the drawback of a lower temporal resolution.

A 'one sided' rhi scan would only need to be operated from roughly 15° elevation to 75°. To measure at lower heights is not necessary as the contribution of the vertical wind is below 15% to the radial wind velocity and decreases to zero with 0° elevation, hence the values would be unstable and very vulnerable to slight shifts of the horizontal wind. Depending on the measurement sight low elevations can be obscured by buildings or vegetation. Above 75° elevation the horizontal range of the lidar decreases significantly. In a normal boundary layer the lidar can measure up to a height of approx. 2500 m, which would mean that data with a maximum horizontal distance from the lidar of 670 m can be recorded for an elevation angle of 75°. Depending on the area of interest even lower elevations could be enough.

The temporal resolution will increase significantly with this 'one sided' rhi scan. With a scanning speed of 6° per second a rhi scan can be performed every 10 seconds. Increasing the scanning speed up to 20° per second would result in a rhi scan every 3 seconds.

With this scanning strategy two main objectives could be realised:

1. The shifting speed of convective structures in relation to the mean horizontal wind speed could be obtained, using Taylors hypothesis of the "frozen turbulence".

2. The change of the axis inclination can be tracked.

The site of the CLR Doppler lidar at the FZK would probably only allow a 'one sided' rhi scan. As described in chapter 3 the lidar is at the northeastern end of an open field. The view towards the southwest and west is unobstructed, but towards the northeast and east the site is surrounded by trees allowing only measurements at higher elevations.

7 Lidar Measurements in the Planetary Boundary Layer

7.1 The Planetary Boundary Layer

The main area of measurement for the Doppler lidar is the planetary boundary layer (PBL)(Fig. 19), sometimes called the atmospheric boundary layer, which is directly influenced by the Earths surface. This is due to the small exchange between planetary boundary layer and free atmosphere, the air in the planetary boundary layer normally contains a lot more particles and aerosols than air in the free atmosphere, as most of the emissions into the atmosphere take place near the Earths surface. There are generally two classes of the atmospheric boundary layers, the convective boundary layer with turbulence driven mainly by thermal convection and the stable boundary layer where turbulence is generated by horizontal wind shear.

During the summer the planetary boundary layer has a vertical extent of up to approx. 2 km. But its height is subject to diurnal change. During the night a stable nocturnal boundary layer with a vertical extent of up to 300 m exists. After sunrise the convective boundary layer starts to grow in height and reaches its maximum at mid day. After sunset the energy for thermal convection is no longer present, so turbulence decays and the development of the nocturnal boundary layer starts, leaving a residual layer marking the extents of the vanished planetary boundary layer. In winter hardly any diurnal changes occur to the boundary layer.

The top of the nocturnal boundary layer is marked by an inversion zone, which has to be broken up before thermal driven convection can extend higher up into the planetary boundary layer. This normally takes place in the morning hours some time after sun rise, providing enough energy is present at the surface to initiate convection. At the top of the planetary boundary layer is the so called entrainment zone, where an entrainment of clear air from the free atmosphere takes place. But the exchange is normally very small due to another inversion a this point. Only if due to the conditions in the planetary boundary layer air quantities driven by buoyancy past this capping inversion, a significant exchange between planetary boundary layer and free atmosphere then takes place. This is often combined with the development of cumulus clouds at the top of the

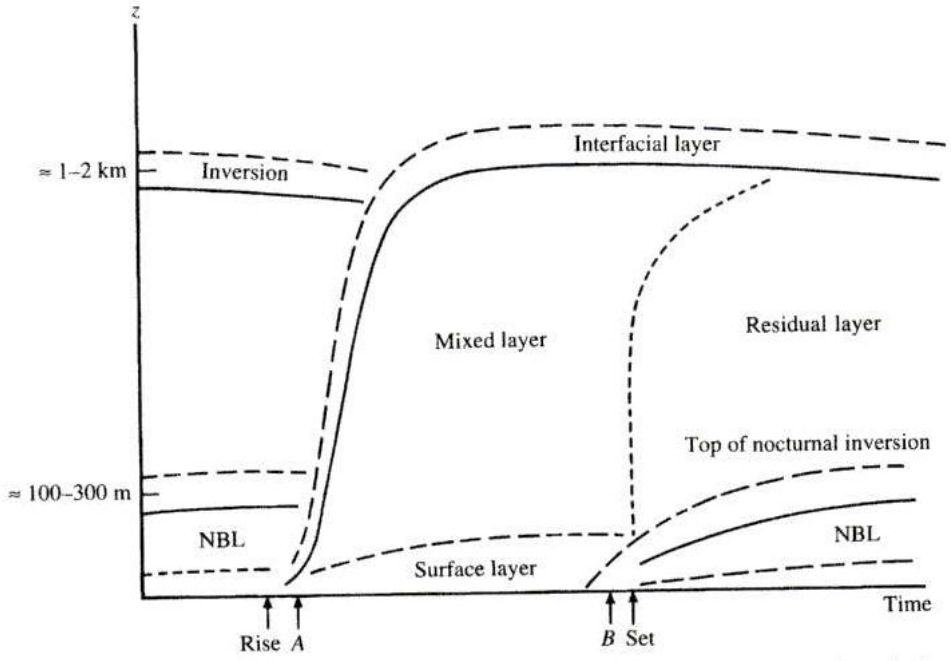

Figure 19: Diurnal development of the Planetary Boundary Layer (Garratt, 1992)

planetary boundary layer reaching up past the inversion zone. Providing enough CAPE is available convective driven thunderstorms can develop.

7.2 Different Measurements in the Planetary Boundary Layer

As described above the concentration of aerosols is likely to be much higher within the planetary boundary layer than above (Flamant and Pelon, 1996). This means that a higher signal to noise ratio (SNR) and a higher aerosol backscatter is to be expected within the planetary boundary layer. Additionally vertical wind speeds should also be higher and more turbulent within the planetary boundary layer. Considering this, a description of the planetary boundary layer concerning its temporal development (especially the vertical extent) and turbulent vertical wind speed can be made.

7.2.1 Boundary Layer Height Detection

The height of the boundary layer can be measured by different instruments. One of the most common and easiest is by the use of radiosondes. As described above the top of the nocturnal and the fully developed boundary layer is marked by an inversion zone. The temperature profile

of a radiosonde ascent shows these regions clearly. The major disadvantage using radiosondes is that only a snap shot of the atmospheric condition is taken and that gaps of sometimes several hours between measurements exist, e.g. the height of the boundary layer (z_i) shows are great spatial and temporal variation which can not be measured by radiosondes only by remote sensing instruments with a high temporal resolution like a lidar. Additionally the usage of radiosondes is expensive and labour intensive. Measurements from towers normally do not reach high enough to detect the planetary boundary layer height during the day. Measurements from aeroplanes are very expensive and often restricted on where they can fly. Ideal instruments therefore are active remote sensing instruments to which the lidar belongs.

For boundary layer height detection remote sensing instruments (e.g. lidar or ceilometer) mostly use the difference in aerosol concentration in the mixing layer and the free atmosphere. Sometimes automatic detection with formulas is used but often simple drops in aerosol concentration is used for boundary layer height detection (Boers and Elorante, 1986). One possibility used described by Steyn et al. (1999) is to fit the measured backscatter profile to an idealised profile. Others (Hooper and Eloranta, 1986) use a derivation method to obtain peaks in the aerosol concentration, these layers often indicate the top of the planetary boundary layer.

For measuring the planetary boundary layer height with the CLR Wind Tracer Doppler lidar the laser beam was fixed in an upward looking position. This way the vertical wind component w could be measured directly and a profile of the planetary boundary layer right above the lidar was created. A recording rate of 1 Hz was chosen, which means that for one value 500 single laser shots were averaged. This rate showed to be practical, as turbulent structures could be detected easily but the sampling rate was not too short and the quality of the measurement was still very good. First measurements were made on August 2, 2004 at the Forschungszentrum Karlsruhe. To determine the boundary layer height the signal to noise ratio was used. The atmospheric backscatter is calculated from the signal to noise ratio and holds no additional information to the question of boundary layer height.

The nocturnal boundary layer has a vertical extend of $100 - 300\ m$, this height can not be measured by the lidar, first values are obtained at approx. $400\ m$. This means that the nocturnal boundary layer can

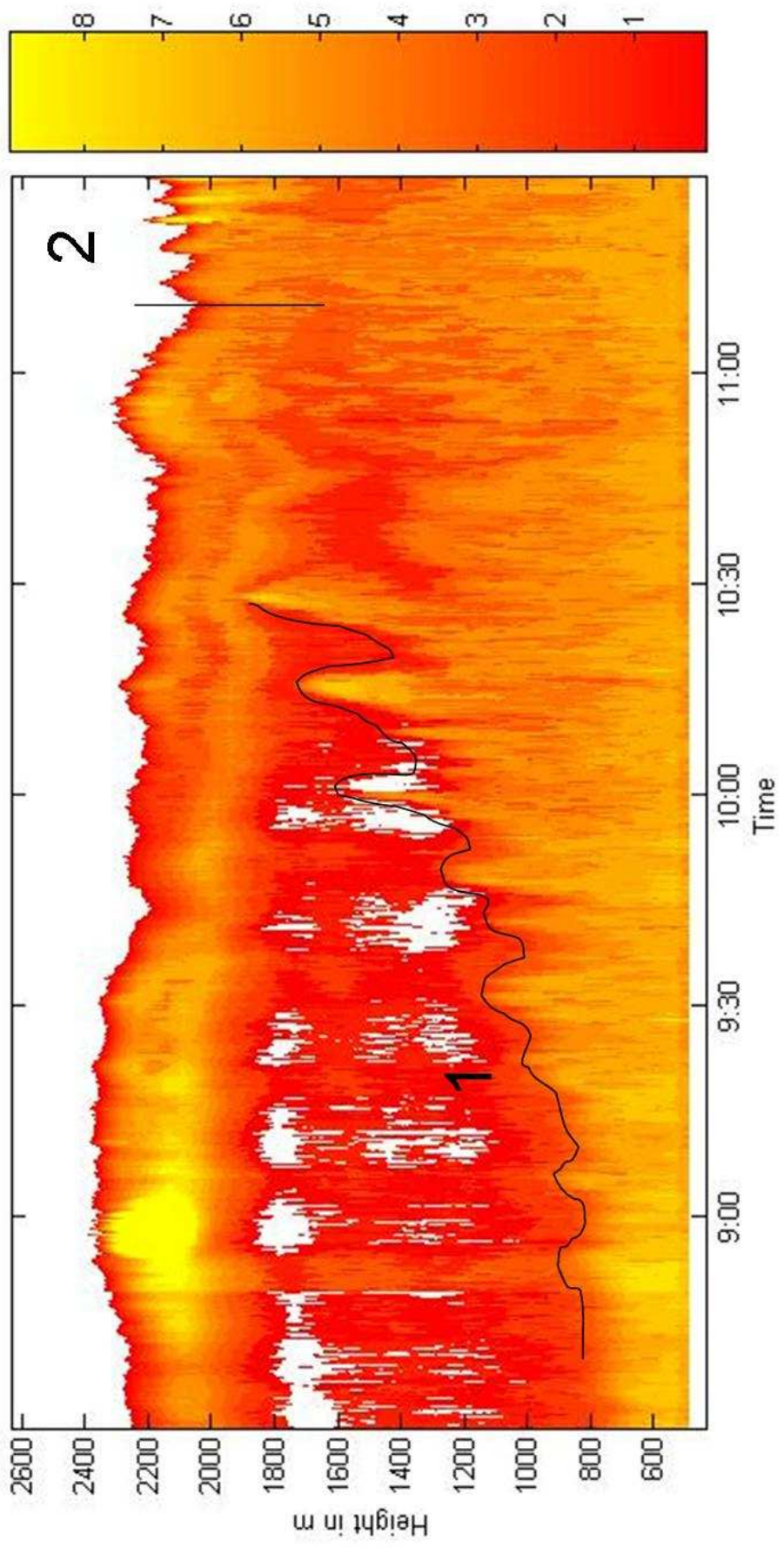

Figure 20: Signal to noise ratio for vertical lidar measurements on August 2nd 2004 from 8:30 UTC to 11:30 UTC. Position 1: pulsation of the growing mixing layer, position 2: mixing layer reaches the top of the residual layer.

not be measured during the night, only the growth of the mixing layer out of the remainders of the nocturnal boundary layer after the surface inversion is broken up (at 6:00 UTC) can be detected.

A typical profile of the signal to noise ratio in the boundary layer in the morning hours, with a growing mixing layer, has a first maximum in the very first range gates at approx. 600 m agl., then relative low values for most of the residual layer and a second maximum at the top of the residual layer (Fig. 20). The top of the planetary boundary layer is marked by a sharp drop of the signal to noise ratio within a few range gates. As the boundary layer develops in the course of the morning, between 9:00 and 10:30 UTC, the lower maximum is transported higher up into the atmosphere. This growth of the mixing layer is coupled with strong upward winds. This results in a 'pulsation' of the growing mixing layer (position 1 of Fig. 20).

Between 10:30 and 11:30 UTC very high vertical wind speeds exist (see chapter 8 and the convection is present within the whole residual layer. At about 11 UTC the mixing layer reaches the top of the residual layer so the planetary boundary layer is now fully developed (position 2 of Fig. 20). The height of the planetary boundary layer is about 2200 m above ground. with thermals reaching up to 2300 m above ground. The height of the boundary layer starts varying after it is fully develop. This variation can not be recorded with radiosondes.

The numerical values for the mixing layer and boundary layer height are subject to daily changes. This means that the threshold for the signal to noise ratio has to be adjusted for every day. If there are no bigger changes in the air mass these values are the same during the whole day. On August 2 the nocturnal boundary layer and the growing mixing layer was characterised by an $SNR > 3$, for the top of the planetary boundary layer a drop of the signal to noise ratio below -10 was set. According to the lidar manual (CLR Photonics, 2002) a signal to noise ratio of -10 is the lowest value at which reliable data can be obtained.

Some areas, especially in the first one and a half hours, are displayed in white. This is because the value at these points is below zero and therefore not in the scaling range. At 9:00 UTC a significant increase in the signal to noise ratio at heights between 2000 and 2200 m shows up. This is most likely a cloud, but is not created through convection and therefore will not be looked at in detail.

7.2.2 Cloud Detection

The light of the laser does not only reflect on aerosols, but on any reflecting object $> 2\ \mu m$ which includes rain drops and cloud droplets. Reflectivity on water drops is very good. On the other hand attenuation of the laser light within clouds or under foggy conditions is also very big, which means that lidar measurement e.g. during a rain shower is not possible.

But the increase of reflectivity, which also leads to a better signal to noise ratio means that it is possible to detect clouds with a lidar (Carswell et. al, 1995). The same measurements as were used before to detect the boundary layer height are now used to detect clouds within the boundary layer. In Figure 21 several areas of a very high signal to noise ratio ($>$ 9) can be identified. The duration of this high signal to noise ratio is in three cases approx. 8 minutes (11:58-12:06, 12:20-12:28 and 12:45-12:53 UTC), with a shorter block of approx. 3 minutes from 12:32-12:35 UTC. These periods are identified with solid black lines in Figure 21, indicating the duration of the clouds and the cloud bases. Duration as well as the height indicate that these objects can be clouds.

As no radio sonde ascents are available for this day in Karlsruhe the cumulus condensation level can not be calculated. But the lifting condensation level (lcl) can be calculated using the following equation:

$$lcl = a(T - T_d) \tag{3}$$

where $a = 0.125\ km\ ^{\circ}C^{-1}$ T and T_d are the near surface temperature and dewpoint, respectively (Stull, 1995). This gives a rough idea in which height clouds can be expected, although this day is more likely to have clouds caused by convection than by forced lifting processes. Using the 4 m data from the 200 m tower at the Forschungszentrum Karlsruhe the lifting condensation level calculates to 2066 m above ground. Another indication for clouds is the global radiation on this day, also recorded at the 200 m tower. Figure 22 shows the global radiation for August 2. Several sharp drops on the global radiation indicate the passage of clouds between the instrument and the sun. Especially around midday and in the afternoon several cloudy periods are present. Some of these coincide very well with the times the lidar registers high signal to noise ratio values, these areas have been shaded in Figure 22.

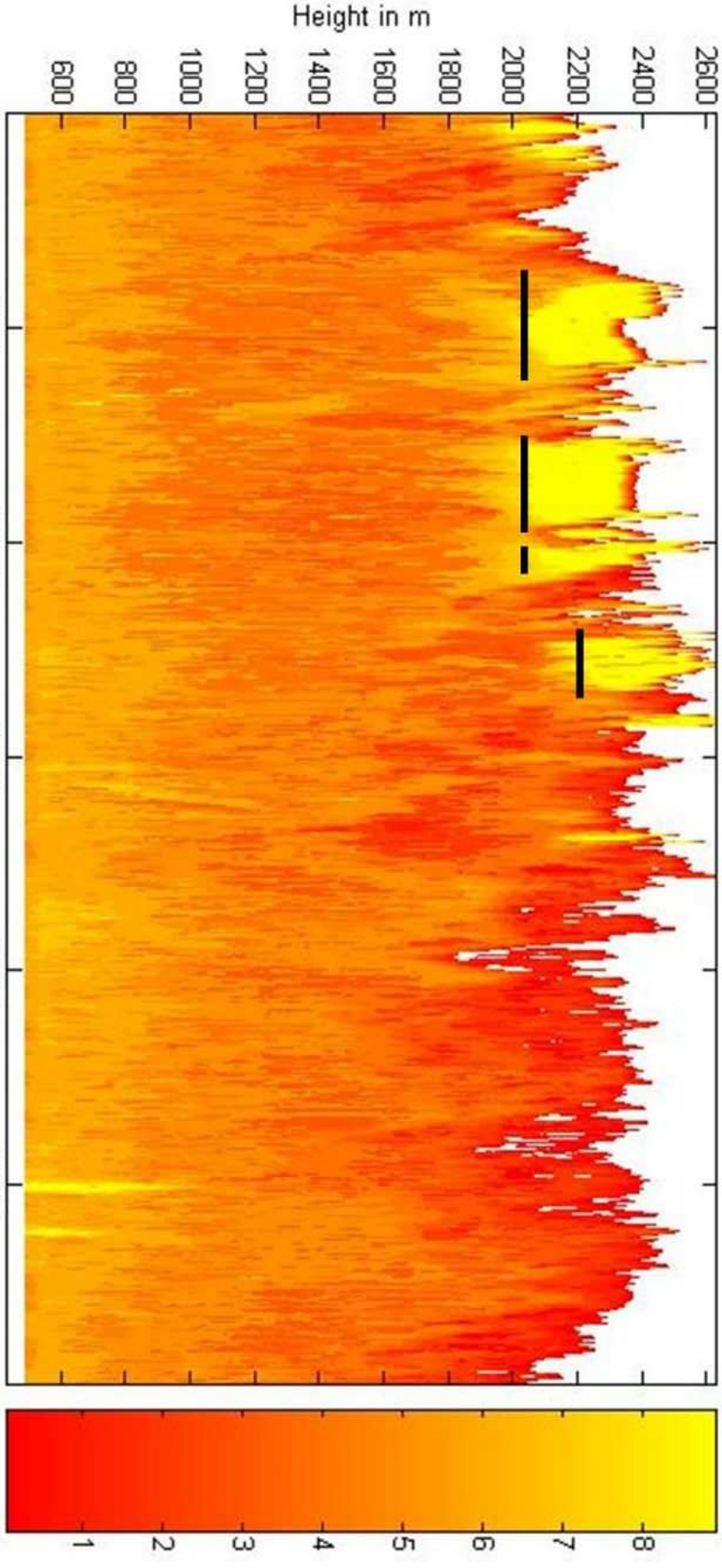

Figure 21: Signal to noise ratio for vertical lidar measurements on August 2nd 2004 from 11:30 UTC to 14:30 UTC. Black lines indicate cloud base and temporal extend.

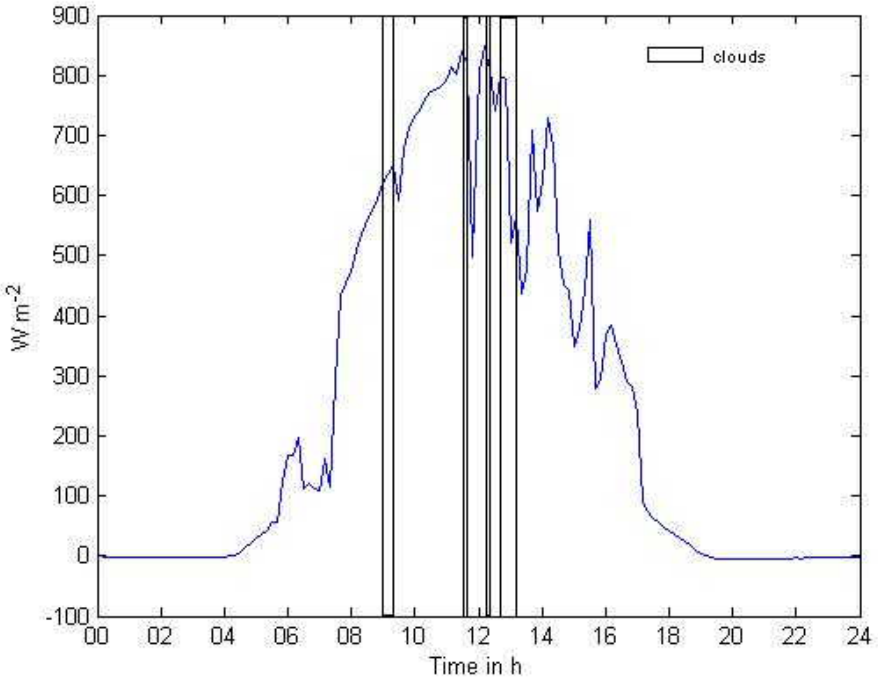

Figure 22: Global radiation August 2nd measured at the 200 m tower at the Forschungszentrum Karlsruhe, time in 10 min from midnight. Boxed in areas indicate clouds detected by the lidar.

For the identification of the clouds a sudden increase in the signal to noise ratio was registered. A $SNR > 8$ was used as a threshold for this day. This means that in the time between 11:30 and 13:00 UTC (Fig. 21) three major clouds were detected passing over the lidar. At 11:55, 12:15 and 12:45 UTC all three having a duration of approx. 8 minutes. The base of the clouds are at approx. 2000 m, this is a very good agreement with the value calculated for the lifting condensation level. At 12:30 UTC a smaller cloud passed over the lidar. During the rest of the afternoon no further clouds can be detected.

Figure 21 also shows that the Doppler lidar can not only detect the cloud bases by the increase in the signal to noise ratio it can also look into the clouds for some range gates (approx. 200 - 300 m). With this, vertical wind speeds and turbulence can be measured in the lower part of the cloud. Combining these measurements with e.g. cloud radars would enable a new look at processes in convective clouds.

The top of the boundary layer increases in height after the clouds passed over the lidar. These clouds were probably cumulus clouds with their bases in the top part of the boundary layer, reaching beyond the capping inversion. Thus they transport mass from the boundary layer into the

free troposphere and also increase the boundary layer height (see also chapter 8). In the afternoon after 14:00 UTC when no further clouds pass by the top of the boundary layer slowly drops again to heights of 2200 m and below.

8 The vertical wind velocity on a convective day

For this chapter the same measurements were used as in section 7.2.1. With the laser pointing upwards the vertical wind component w is directly measured, so no algorithm has to be used to determine this component. On the other hand no information on the remaining two components u and v are acquired. With this measurement technique a data set of the vertical wind with a high temporal and spatial resolution is recorded. The measurement is done with 1 Hz and a range gate resolution of 80 m. Measurements started at 8:30 UTC on August 2nd 2004 with this setup and continued to 8:30 UTC on August 3rd. The system was setup to record the data in one hour files. In all of the following figures the height is above ground.

8.1 The nocturnal boundary layer

During the night and early morning when the nocturnal boundary layer with a stable stratified surface inversion exits the vertical motion diminishes and $|w|$ is for long periods below 0.5 $m\,s^{-1}$ which is the velocity resolution of the lidar (Fig. 23). During the night when no energy from radiation is available vertical wind can only be produced by horizontal wind shear but on the days of measurement the horizontal wind was not strong enough to produce sufficient wind shear. The artefact between 2000 and 2500 m are due to very low signal to noise ratio ($SNR < -10$), so these velocities have to be ignored (see section 7.2.1).

8.2 The developing mixing layer

After sunrise the ground starts to heat up, the surface layer becomes unstably stratified and the sensible heat flux becomes positive. This provides energy for convection. With this energy thermals start to develop and convective turbulence starts to erode the nocturnal boundary layer. The surface inversion has a ΔT of 2.25 $°C\,per\,100\ m$ and extends the height of the 200 m tower. According to the tower data the surface inversion is broken up at 6:00 UTC and the development of the mixing layer can start.

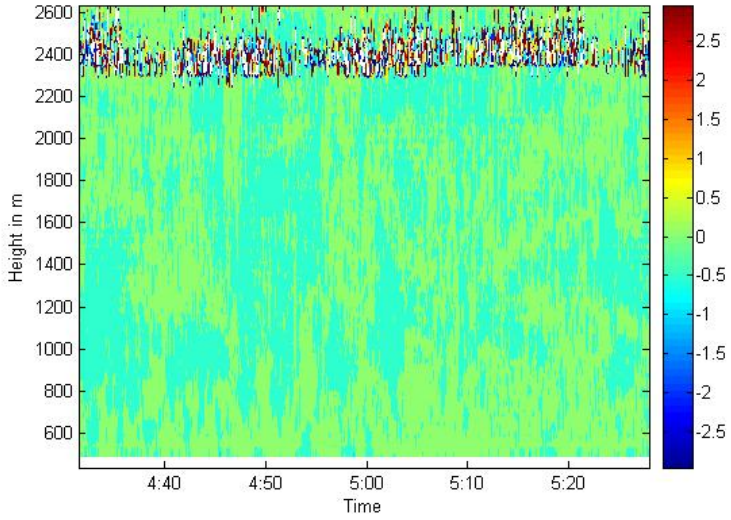

Figure 23: Vertical wind speed w in $m\,s^{-1}$ in the NBL, on 3rd August 2004 from 4:30 to 5:30 UTC

The growth of the mixing layer (see section 7.2.1 and Fig. 20) corresponds very well with the vertical wind (Fig. 24). Individual upward bursts of the growing planetary boundary layer can be allocated to strong vertical winds. Above the mixing layer the vertical winds remain at the same very low values as during the night, whereas within the mixing layer vertical wind speeds of up to 3 $m\,s^{-1}$ are measured.

In the mixing layer areas of strong upward drafts are followed by equally strong downward winds. This indicates that the developing planetary boundary layer is strongly turbulent. The nocturnal boundary layer is so low that it can not be detected by the lidar. During the first hours of measurement until 10:00 UTC significant wind speeds are present only in the very lowest range gates of up to 1000 m.

From 10:00 UTC onwards the mixing layer grows rapidly and reaches its maximum at around 11:00 UTC. The vertical wind speeds also increase and exceed frequently the 3 $m\,s^{-1}$ during this time. In addition significant down drafts occur with wind speeds also reaching 3 $m\,s^{-1}$.

In Figure 24 some thermals appear to have a slightly tilted vertical axis. In this time plot the thermals have a 'forward' tilted axis, which would mean that the axis are tilted 'backwards' against the horizontal wind. Some thermals have an extend of up to 2000 m. However no statement can be made if these vertical plumes that show up in the time plot are single thermals with a defined axis or if warm air rising from the

surface just fans out with time. Due to the measurement technique no information on the horizontal wind in these height is available. With a suitable scan strategy as described in section 6.3 it might be able to detect the spatial variation of these thermals.

8.3 The fully developed planetary boundary layer

In the fully developed planetary boundary layer vertical wind speeds exceed $\pm 3\ m\,s^{-1}$ frequently and up and downdrafts alternate rapidly (Fig. 25). Especially in the time from 11:30 to 13:00 UTC large areas of high wind speeds occur. During the time when clouds are present (see chapter 7.2.2 and marks in Fig. 25) vertical wind speeds increase even further and reach a maximum near the cloud base and the lower part of the clouds. In and above the clouds white areas show up, this is because the measured wind speed is outside the displayed range. But as explained in section 7.2.2 the signal to noise ratio is too low as that these values can be correct wind speeds.

The last cloud from 12:45 to 12:53 UTC is significantly different from the first two major clouds. No increase in wind speed can be detected underneath or in the lower part of the cloud. This is due to the life cycle of a convective cloud (Garratt, 1992). In the developing stage a convective cloud draws energy from condensation in the cloud base and strong upward winds are present. To the end of the life cycle no more energy from the boundary layer is transferred into the cumulus cloud and the feeding vertical winds die down. The cycle takes approx. one hour. The third major cloud is probably in this last stage before dissolving.

In the following hours turbulence is present throughout the whole planetary boundary layer but slowly decays in the afternoon (Fig. 26). The vertical wind and with it the turbulence dies down completely after the turbulent heat flux at the surface becomes negative at 17:20 UTC and the energy for convective driven turbulence is no longer provided (Fig. 27).

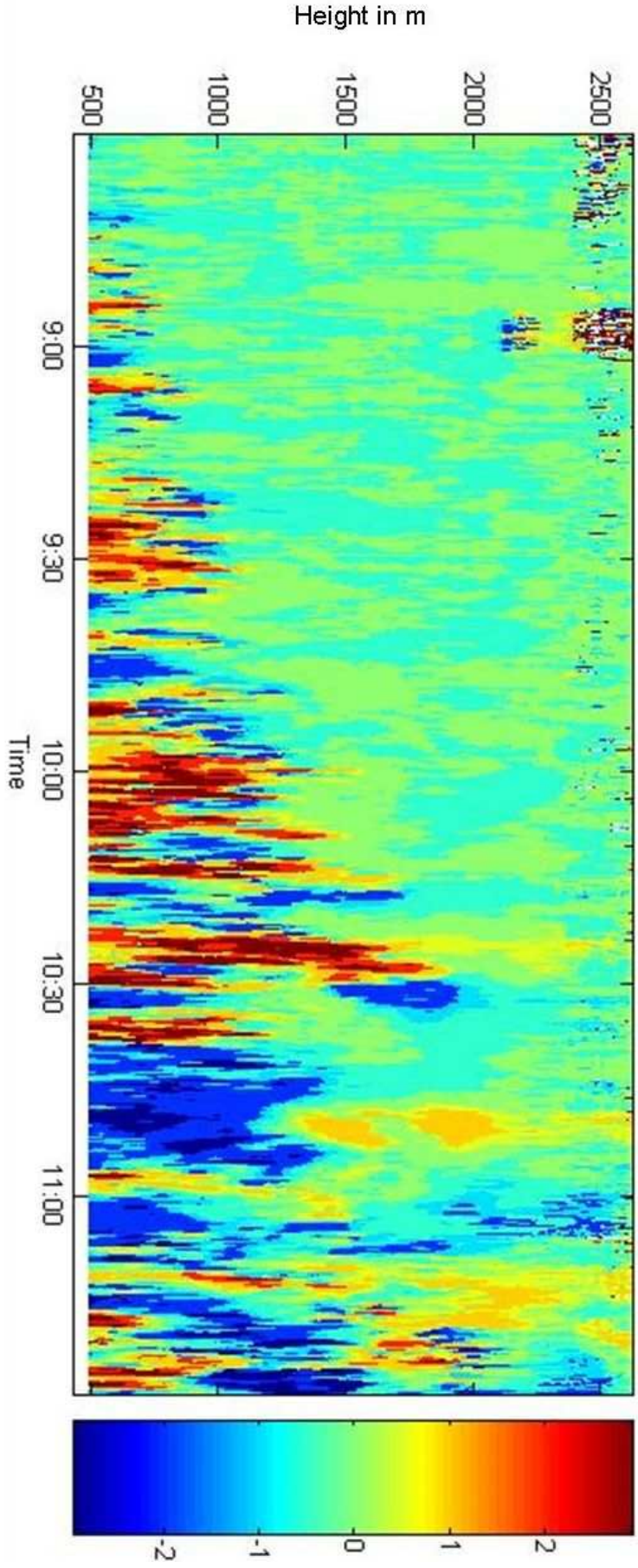

Figure 24: Vertical wind speed w in $m\,s^{-1}$ on August 2, 2004 from 8:30 to 11:30 UTC.

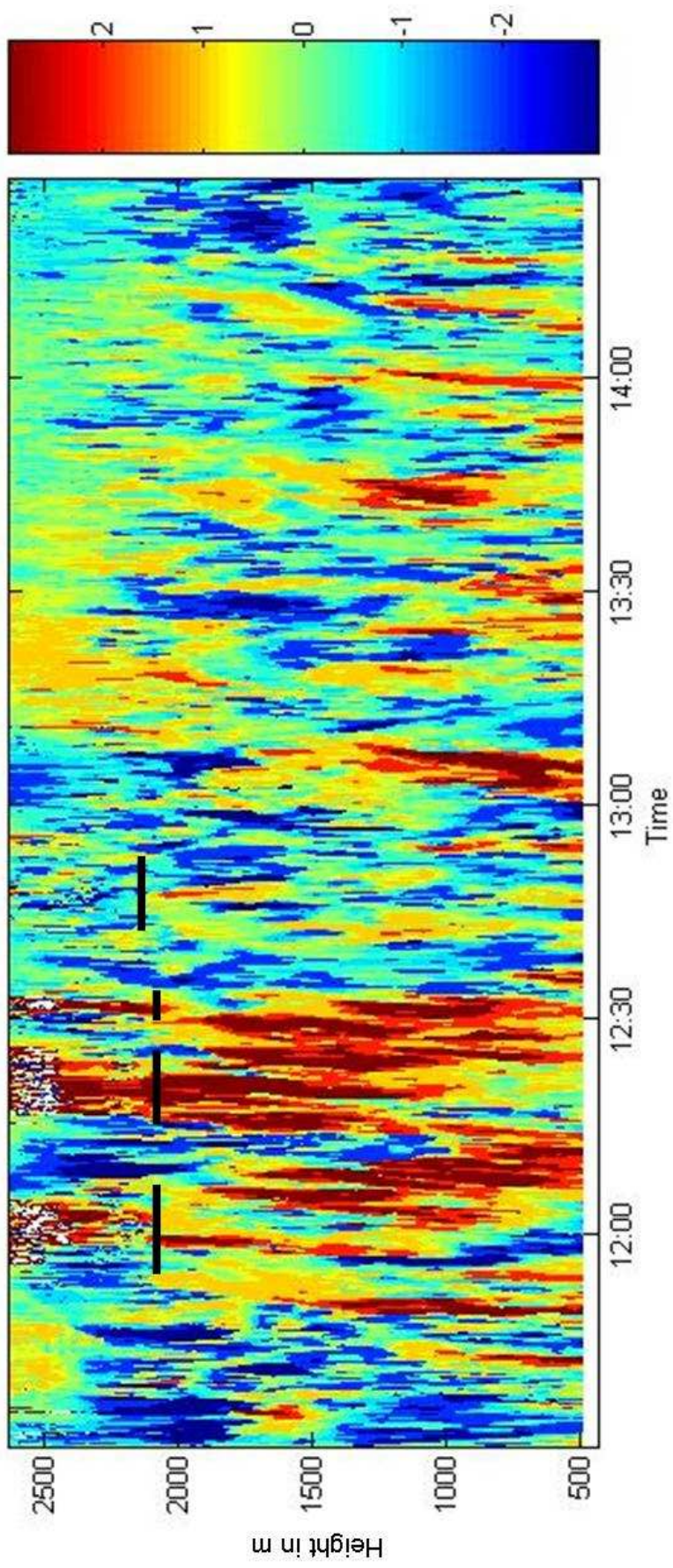

Figure 25: Vertical wind speed w in $m\,s^{-1}$ on August 2, 2004 from 11:30 to 14:30 UTC. Solid Black lines indicate the duration of the clouds and the height of the cloud base.

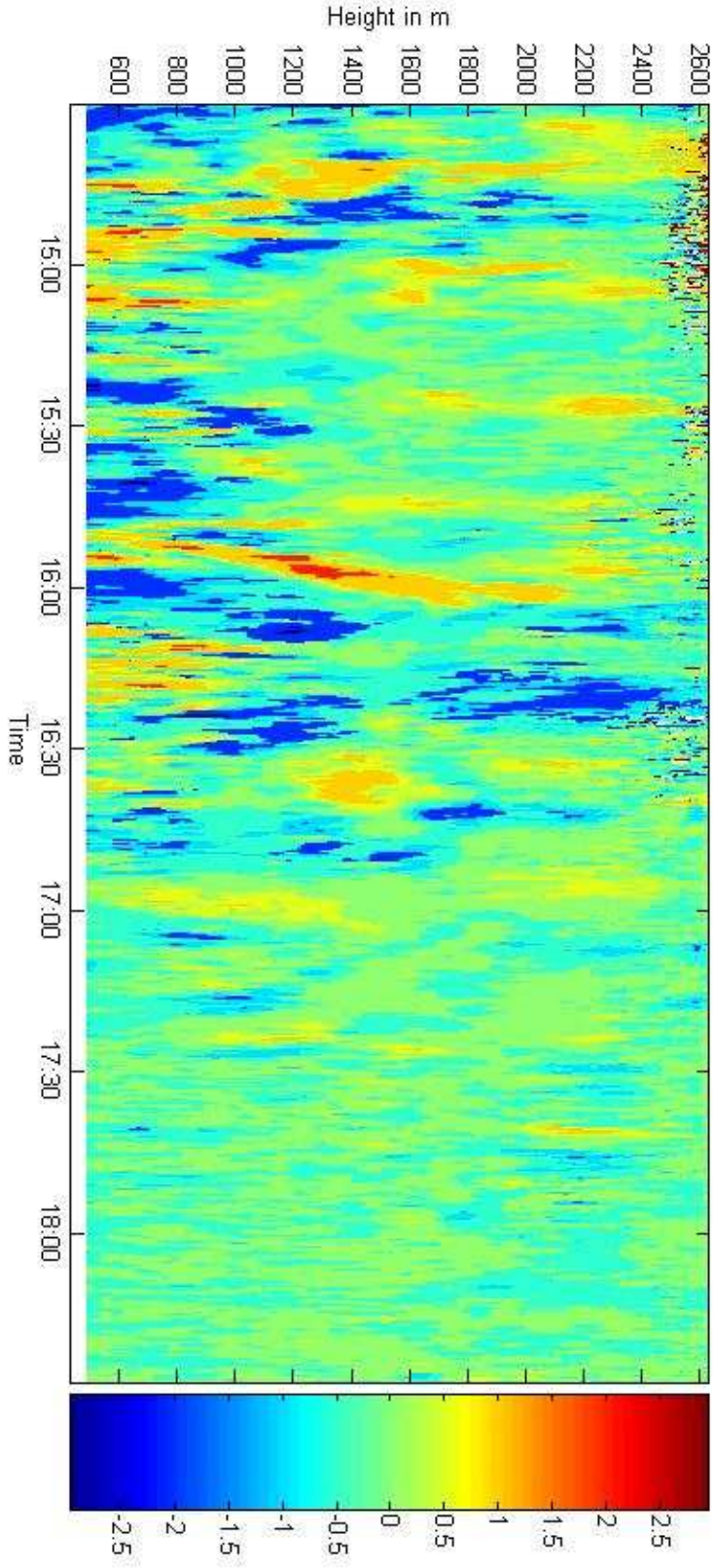

Figure 26: Vertical wind speed w in $m\,s^{-1}$ on August 2, 2004 from 14:30 to 17:30 UTC.

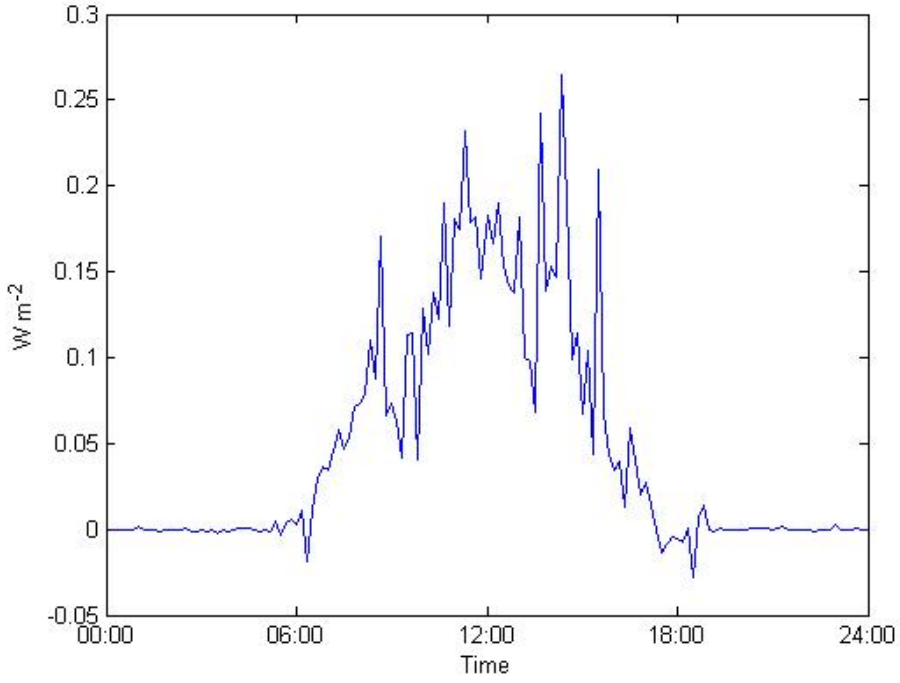

Figure 27: Kinematic heat flux measured at the 200 m tower at the FZK in a height of 4 m on August 2, 2004. Time in UTC.

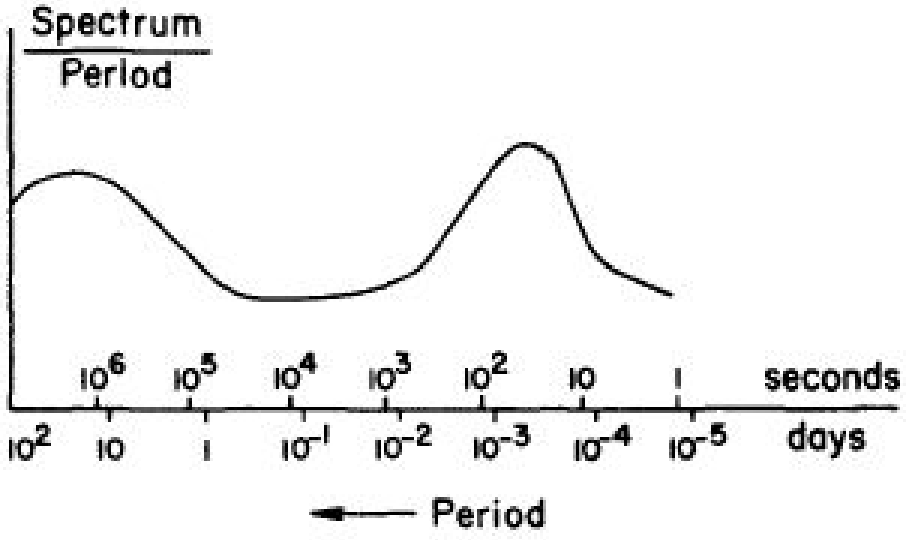

Figure 28: Schematic frequency spectrum, after Fiedler and Panofsky (1970).

8.4 Profile of the vertical wind and its standard deviation

In the previous section the spatial and temporal development and distribution of the vertical wind field was described. This helps to get an overview of the development of convective turbulence. In this section profiles of the vertical wind field and standard deviations will be looked at. Standard deviations over a period of mostly 10 minutes will be compared. The standard deviation can be seen as an information for turbulence (see section 8.4.2).

8.4.1 Vertical Profiles of vertical wind velocity

The profiles for the vertical wind are made up of 10 minute averages, this is a common time scale to average wind speeds for turbulence analysis in the planetary boundary layer. The 'spectral gap' after Fiedler and Panofsky (1970) (Fig. 28) shows that with a ten minute average most of the turbulent part of the atmospheric spectrum is included.

The first profiles between 8:30 and 9:30 UTC show that in the residual layer of the nocturnal boundary layer hardly any vertical wind speed is present, the values vary below $\pm 0.2\ m\,s^{-1}$, which is below the detection limit of the lidar of $\pm 0.5\ m\,s^{-1}$. Only in the lowest range gates are slightly bigger values present (Fig. 29). One exception has to be made for profile 3. As mentioned before a cloud passed over the lidar during this time, this explains the increase in vertical motion at the top of the

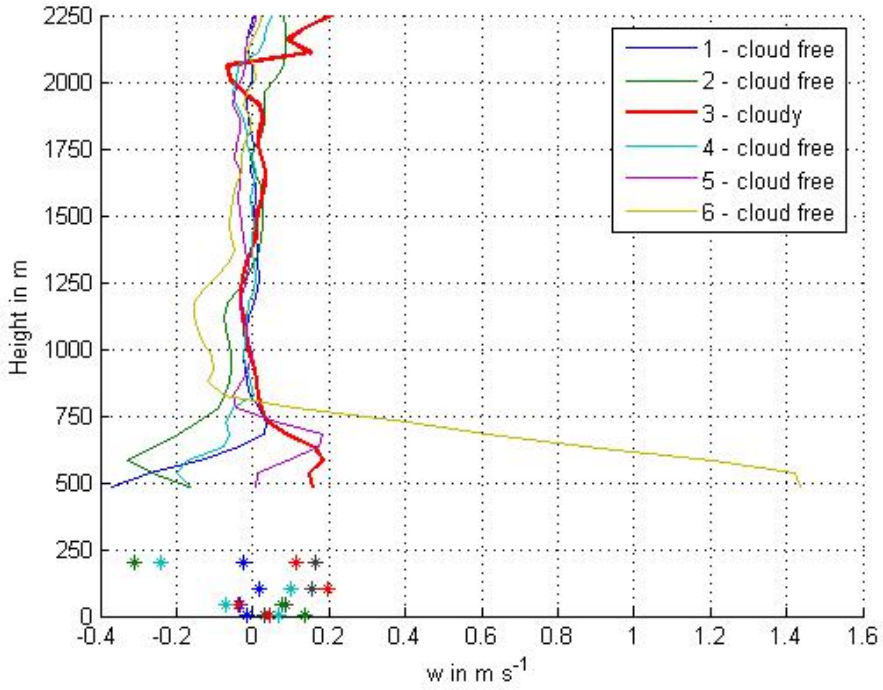

Figure 29: Profile of vertical wind speed w on August 2, 2004 from 08:30 to 09:30 UTC. Lidar data (solid lines) and data from the 200 m tower of the FZK (asterisks).

residual layer for this profile. In this and the following figures the lidar data (solid lines) are complemented with data from the 200 m tower of the FZK (asterisks).

During the next hour the vertical wind speeds increase up to 2 $m\,s^{-1}$ and the region with significant wind speeds extends higher up into the atmosphere (Fig. 30). But for large regions there is still no vertical wind. Between 10:30 and 11:30 UTC wind turbulence livens up (Fig. 31) and now convection is present in the whole of the mixing layer. The averaged wind speeds still do not exceed $\pm 2\ m\,s^{-1}$, but the difference between the individual 10 minute averages increases and up to 2250 m and higher wind speeds of $\pm 0.5\ m\,s^{-1}$ exist.

During the period from 11:30 to 12:30 UTC the highest averaged wind speeds of the day are recorded. For this period the averaging time was set to 8 minutes because two bigger clouds pass over the lidar during this time and both have a temporal extent of approx. 8 minutes, also the time between the clouds was roughly 8 minutes. In order to study the effect of clouds in the boundary layer this 8 minute interval was chosen. This also means that no tower data can be used, as this is only available as 10 minute mean values.

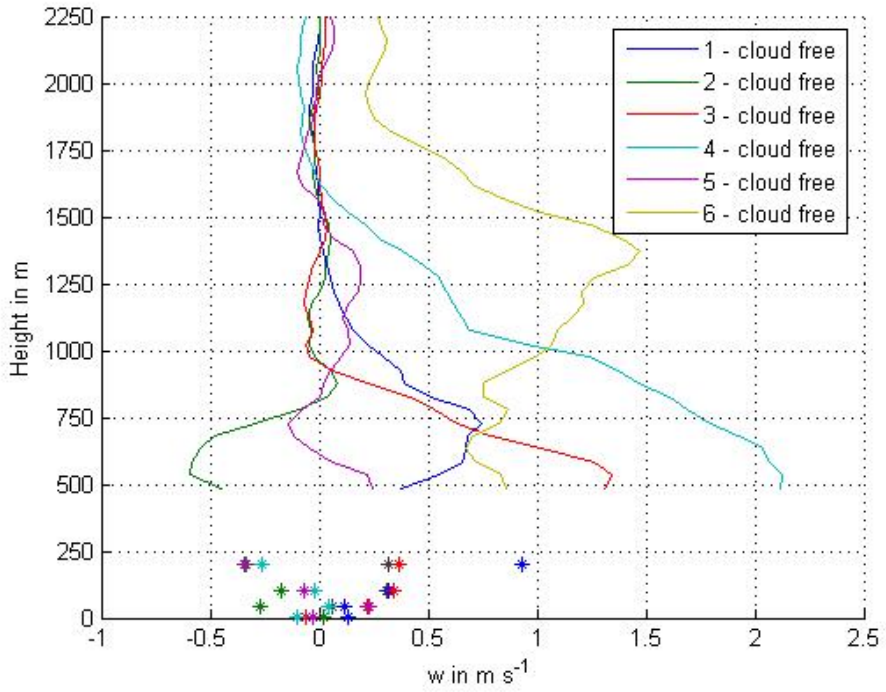

Figure 30: Profile of vertical wind speed w on August 2, 2004 from 09:30 to 10:30 UTC. Lidar data (solid lines) and data from the 200 m tower of the FZK (asterisk).

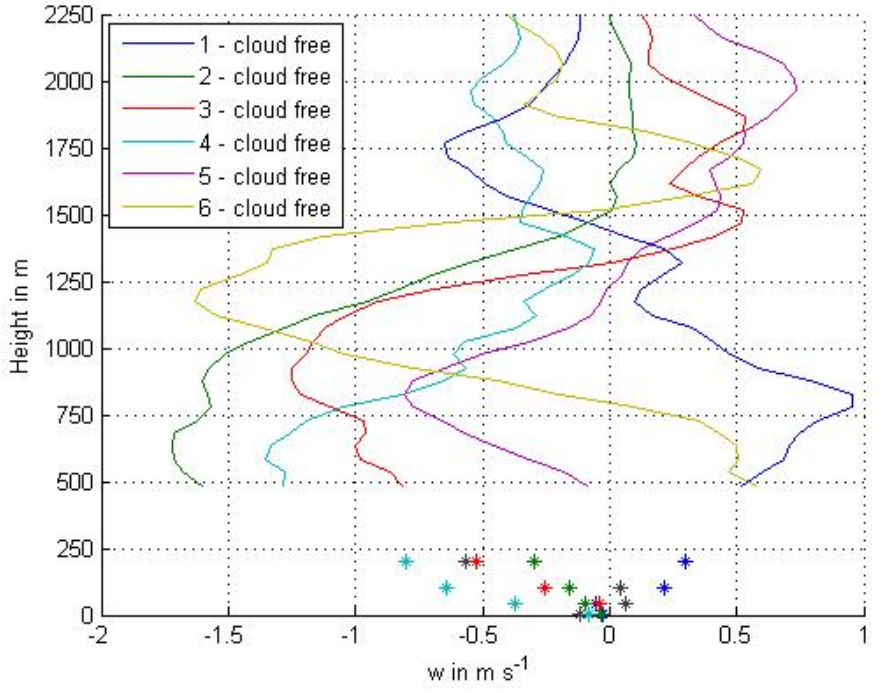

Figure 31: Profile of vertical wind speed w on August 2, 2004 from 10:30 to 11:30 UTC. Lidar data (solid lines) and data from the 200 m tower of the FZK (asterisks).

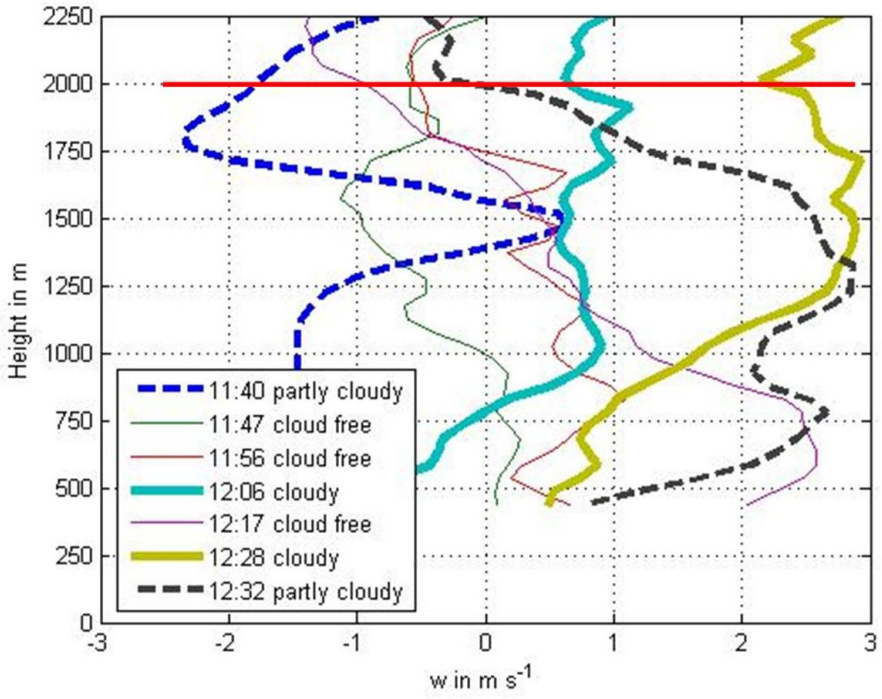

Figure 32: Profile of vertical wind speed w on August 2, 2004 from 11:30 to 12:30 UTC. The cloud base is indicated by the red solid line, based on SNR measurements.

A normal vertical wins speed profile has its highest value in the middle of the boundary layer. At the Earth surface the air can obviously not go downwards, so vertical wind speeds will come to zero. At the top of the planetary boundary layer in general an inversion stops the air from below travelling beyond the planetary boundary layer top, so vertical wind speeds decrease here as well (see section 7.2.2). In the previous figures this could be clearly seen. For the period when clouds pass over the lidar the upper lid for the rising air obviously no longer exists, or is broken up through convective activities when latent heat is released by condensation at the cloud base resulting in buoyancy force (Garrett, 1992).

Strong vertical winds prevail throughout the upper half of the planetary boundary layer (Fig. 32). But for the two periods when clouds pass over the lidar, the profile is significantly different from the other periods. The vertical wind is nearly height constant from 1000 m, which is approx. $z_i/2$, into the cloud base, for the profiles from 11:58-12:06 and 12:20-12:28 UTC. The cloud base is indicated with a solid red line, based on SNR measurements. However there are significant differences in the absolute values between the two profiles. With these strong vertical winds an increased exchange between planetary boundary layer and free

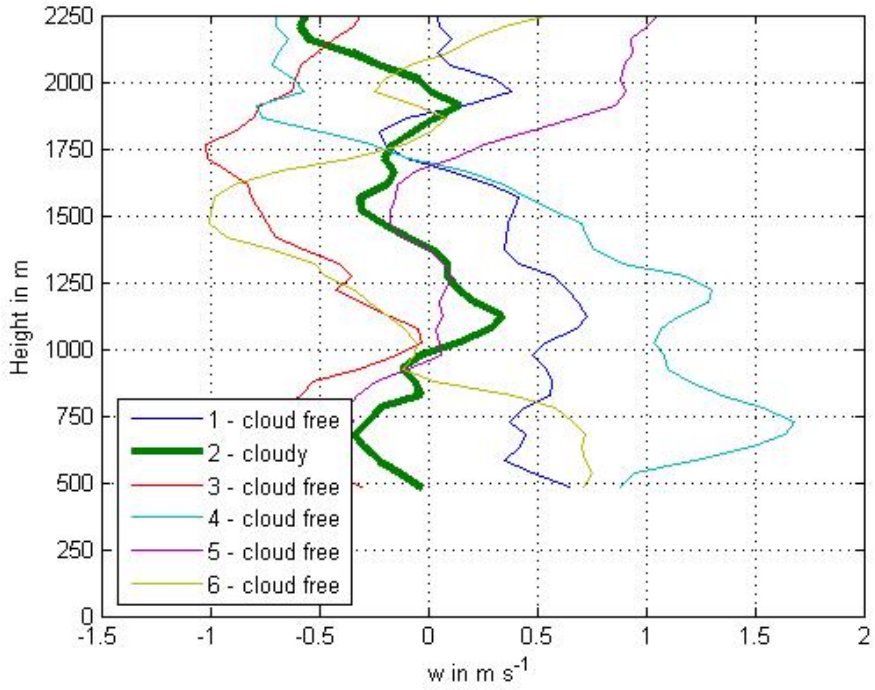

Figure 33: Profile of vertical wind speed w on August 2, 2004 from 12:30 to 13:30 UTC.

atmosphere is possible. For the cloud free periods the upward vertical wind speed reaches its maximum in the middle of the planetary boundary layer, decreases towards the top and the downward motion dominates at the top of the boundary layer, marking the so called entrainment zone.

For the third major cloud from 12:45-12:53 UTC the vertical wind changes with height (Fig. 33). This means that there is no further energy input into the cloud from the boundary layer. For the rest of the day the profiles are similar to those already described. The maximum (upward or downward motion) is in the middle of the planetary boundary layer (e.g. Fig. 34), the lower part of the boundary layer can not be detected with the lidar, but other measurements mainly with towers show that the vertical wind speed decreases towards the surface. At the top of the planetary boundary layer vertical wind speeds also reach a minimum in force.

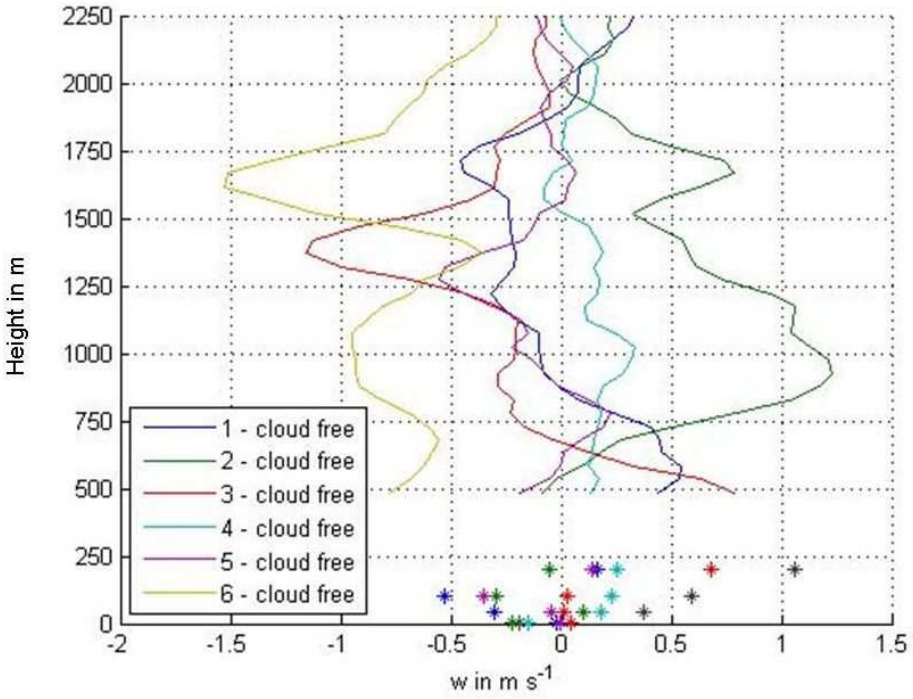

Figure 34: Profile of vertical wind speed w on August 2, 2004 from 13:30 to 14:30 UTC. Lidar data (solid lines) and data from the 200 m tower of the FZK (asterisks).

8.4.2 Standard deviation of the vertical wind

As mentioned briefly above the standard deviation σ is a very good indication for the turbulent character of a measurement series. The standard deviation is defined as:

$$\sigma_x = \sqrt{\frac{1}{N-1}\sum_{i=1}^{N}(x_i - \overline{x})^2}. \tag{4}$$

The standard deviation is therefore the mean of the sum of deviations between the single measurements and their mean value. This formula has a similar form as the turbulence quantity defined by Reynolds (see section 2). Reynolds defines the turbulence quantity as being the deviation of the single measurement from the mean value.

Sometimes the variance instead of the standard deviation is used. The variance is the standard deviation squared:

$$\sigma_x^2 = \frac{1}{N-1}\sum_{i=1}^{N}(x_i - \overline{x})^2. \tag{5}$$

Using the Reynolds definition for turbulence the variance can be written as follows:

$$\sigma_x^2 = \overline{x'^2}. \tag{6}$$

So the variance is the mean turbulence squared.

The variance of the vertical wind σ_w^2 is part of the Turbulent Kinetic Energy (TKE), which is defined as (Stull, 1988):

$$e = \frac{1}{2}\left(\sigma_u^2 + \sigma_v^2 + \sigma_w^2\right) \tag{7}$$

With the data of the lidar measurements only the σ_w^2 part of the TKE can be retrieved. For convective mixing layers the σ_w^2 component is normally dominant over the other two.

When dealing with energy budgets the variance is used as it is part of the energy (see the TKE). The disadvantage is that unit is squared, e.g. the variance of the wind velocity has the unit $m^2 s^{-2}$, which makes it difficult to to compare it to the original measured value.

The standard deviation on the other hand has the same unit as the measured value. As the main focus will be on the vertical wind and its turbulence mostly the standard deviation will be used, except for some comparisons with literature where variances will be used.

As for the vertical wind the turbulence is affected by the Earths surface as a lower boundary in the planetary boundary layer. Near to the ground eddies are small as their size is limited by their height (the radius of an eddy can not be bigger than the height of the eddy above the ground) but they grow larger in diameter the higher they get (Blackadar, 1997). Another limiting factor of eddies is the capping inversion of the planetary boundary layer. As transport through this layer is very little eddy sizes become smaller near the top of the mixing layer.

This means for the vertical distribution of the standard deviation that a maximum in the middle of the mixing layer should be expected, as here vertical wind speeds and turbulence are largest (Caughey and Palmer, 1979). As before the standard deviation was calculated using 10 minutes of measurements corresponding to the mean values of the vertical wind used in 8.4.1, except for those periods when clouds were present, where again 8 minute intervals were chosen.

In Figure 35 the hour from 9:30 to 10:30 UTC is displayed. In section 7.2.2 the rise of the mixing layer height was described and can be seen clearly in the height change of the maximum of σ_w. Not only the height changes from 500 m to 1000 m but also the maximum value increases from around 1 $m\,s^{-1}$ to nearly 2 $m\,s^{-1}$. The lower values in Figure 35 (asterisks) and in the following figures are taken from the 200m mast at the Forschungszentrum, the colours correspond to the same time intervals as the lidar measurements.

In the following hours (except the time when clouds are present, which will be looked at separately) the maximum of σ_w is around 700 to 1000 m (e.g. Fig. 36), with the boundary layer top being at approx. 2200 m.

The interesting part of the day is again the time between 11:30 and 12:30 UTC when clouds pass over the lidar (Fig. 37). Again here a time

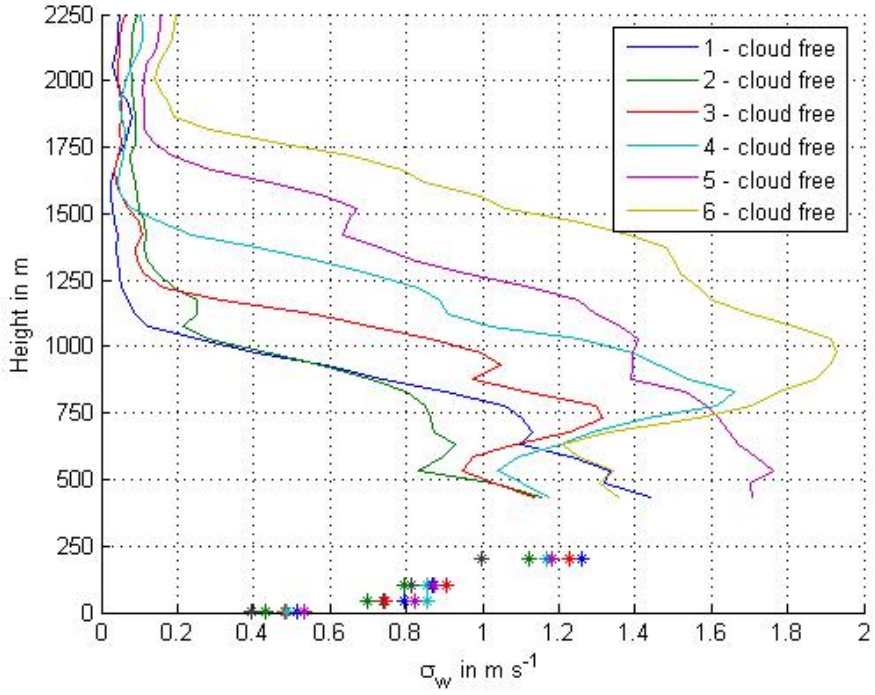

Figure 35: Profile of σ_w on August 2, 2004 from 09:30 to 10:30 UTC. Lidar data (solid lines) and data from the 200 m tower of the FZK (asterisks).

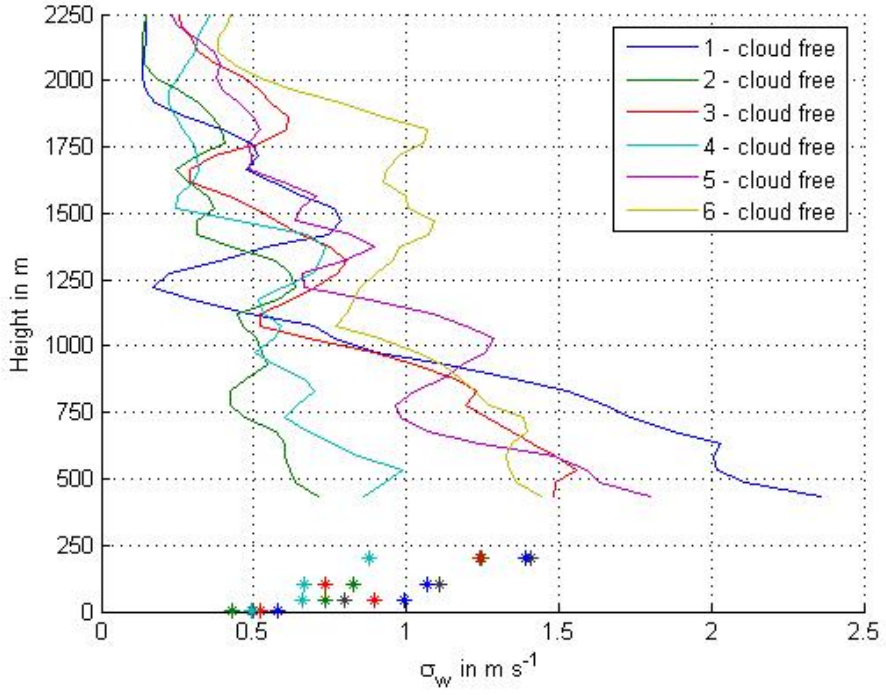

Figure 36: Profile of σ_w on August 2, 2004 from 10:30 to 11:30 UTC. Lidar data (solid lines) and data from the 200 m tower of the FZK (asterisks).

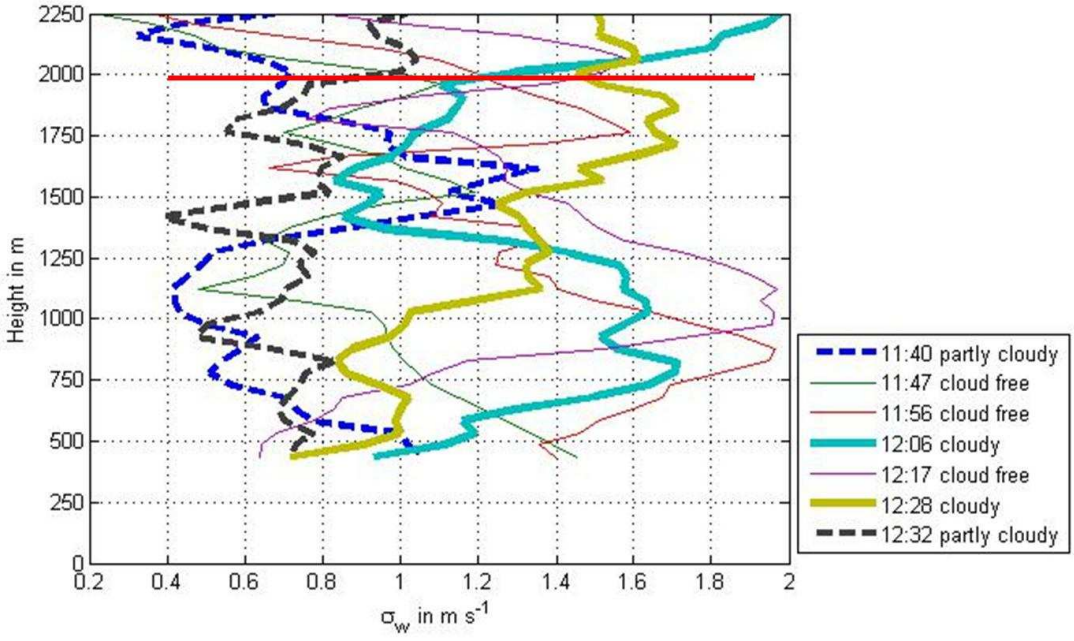

Figure 37: Profile of σ_w on August 2, 2004 from 11:30 to 12:30 UTC. The cloud base is indicated by the red solid line, based on SNR measurements.

interval of 8 minutes was chosen. For the intervals when no clouds are present σ_w has the typical vertical distribution with a maximum near the middle of the planetary boundary layer, and a significant decrease towards the top of the boundary layer.

The times when clouds are present show a very different picture. Here the maximum of σ_w is not in the middle of the boundary layer but at the top underneath and in the lower parts of the clouds. This means that not only the vertical winds have a maximum at the cloud base, transporting mass into the clouds and out of the boundary layer, but also these processes are highly turbulent.

8.4.3 Normalised σ_w

The profiles of σ_w give an idea how much and where turbulence is present in the atmosphere. But to compare different situations at different times or different days these profiles are limited in use. For this purpose σ_w and the height of the profiles have to be normalised.

The height (z) is normalised with the height of the boundary layer (z_i). Doing this a comparison with different boundary layer heights can be

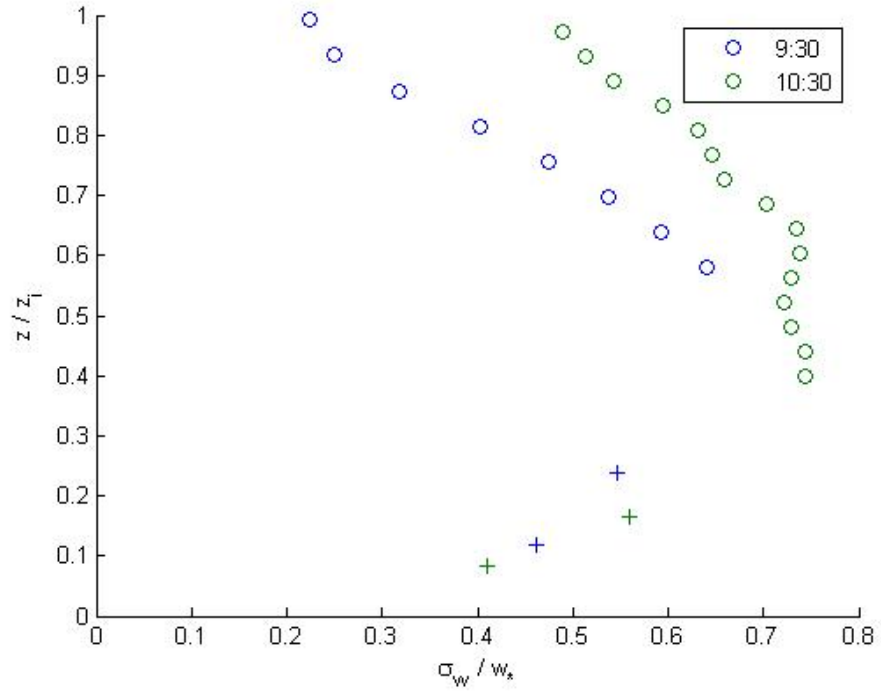

Figure 38: Profile of $\sigma_w/w_\star$ on August 2, 2004 from 08:30 to 10:30 UTC. Lidar data (circles) and data from the 200 m tower of the FZK (crosses)

made. The σ_w is normalised with $w_\star$ the turbulent velocity (Deardorff, 1970).

$$w_\star = \sqrt[3]{\frac{gz}{\Theta}\,\overline{w'\Theta'}} \tag{8}$$

where Θ is the potential temperature, $w'\Theta'$ represents the turbulent heat flux at the surface, g is the gravity constant and z the height of the boundary layer. Doing this σ_w is normalised by the turbulent input from the ground. The data used for $w_\star$ is taken from the 200 m mast at a height of 40 m which is about 10 m above the canopy layer.

The data was divided up into three sets and the resulting profiles looked at separately. This time σ_w was calculated using data from one hour, this was done because most data in the literature has an averaging time of one hour as well. The three cases were two hours in the morning with a developing boundary layer, several hours during midday and in the early afternoon with a fully developed planetary boundary layer and the third case with two hours when clouds were present.

In Figure 38 the two profiles of the developing mixing layer are shown.

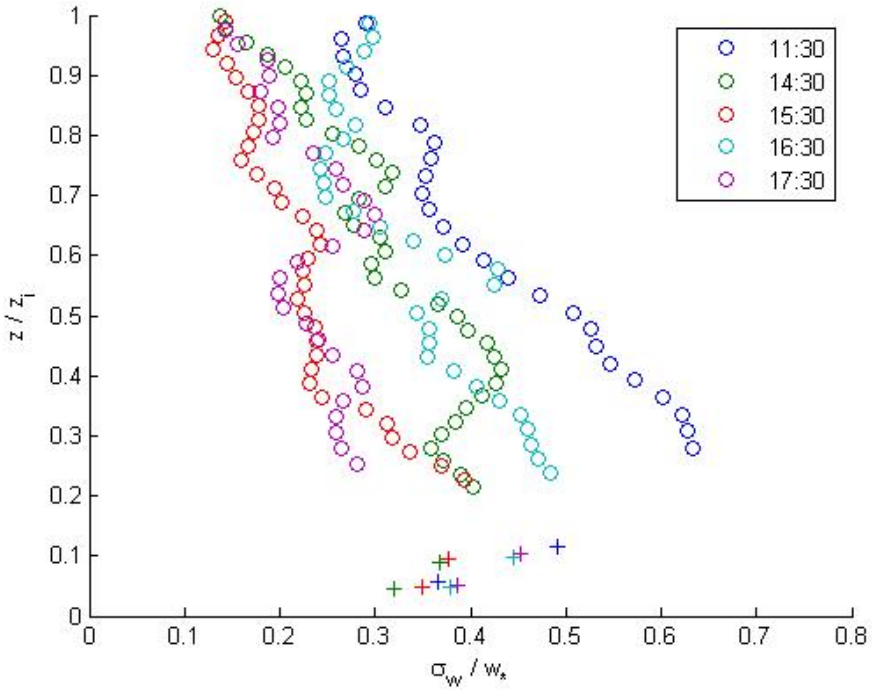

Figure 39: Profile of $\sigma_w/w_\star$ on August 2, 2004 with a fully developed mixing layer. Lidar data (circles) and data from the 200 m tower of the FZK (crosses)

The circles represent the lidar measurements the crosses show the data from the 200 m tower. For the boundary layer height the average of every hour was used. Both profiles clearly show a maximum in the σ_w distribution in the middle of the boundary layer at $z_i \approx 0.5$. The theoretical maximum of the $\sigma_w/w_\star$ quotient is 1 as $w_\star$ is the convective turbulent input from the ground. The maximum $\sigma_w/w_\star$ that is reached is approx. 0.8. The $\sigma_w/w_\star$ value decreases towards the top of the planetary boundary layer but does not reach zero which indicates that some turbulence is still present at the top of the developing boundary layer.

The second case studied are the profiles with a fully developed mixing layer and no clouds present (Fig. 39). Two things are different compared to the first case, the maximum of $\sigma_w/w_\star$ is not at 0.5 z_i but a little lower between 0.2 and 0.4 z_i also the maximum value get smaller the later in the afternoon the measurement is taken. This means that the turbulence in the atmosphere decreases quicker than the input from the ground. The atmosphere gets stable at 17:40 UTC. At the top of the boundary layer values between 0.1 and 0.3 $\sigma_w/w_\star$ are reached.

The third case includes two profiles when the boundary layer is fully developed and clouds pass over the lidar (Fig. 40). For the time when the

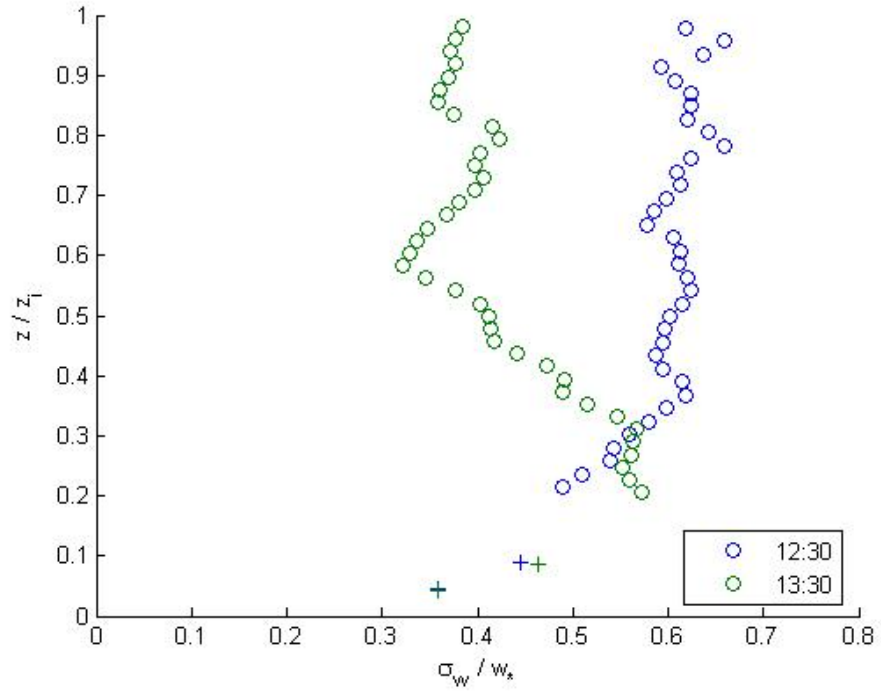

Figure 40: Profile of $\sigma_w/w_\star$ on August 2, 2004 from 11:30 to 13:30 UTC. Lidar data (circles) and data from the 200 m tower of the FZK (crosses)

developing clouds pass over the lidar the profile of the normalised σ_w is significantly different than the profiles before and after. This profile has no longer a clear maximum in the middle or lower part of the boundary layer, but instead increases towards the top of the boundary layer.

The profile from 12:30 UTC shows an increase of $\sigma_w/w_\star$ to approx. 0.63 at 0.4 z_i. Above the value of $\sigma_w/w_\star$ remains nearly constant around 0.6 right up to the top of the boundary layer, increasing even a little further at the very top of the planetary boundary layer. The profile from 13:30 UTC however has a maximum of 0.57 at 0.3 z_i but then decreases more or less constantly to the top of the boundary layer. This profile is comparable to the profiles in non cloudy conditions. This again is an indication that the cloud during this hour is at the end of its life cycle.

The normalised profile of σ_w is strongly dependent on the condition of the clouds in the boundary layer. Apparently decaying clouds do not influence the turbulence in the boundary layer. On the other hand developing cumulus clouds at the top of the boundary layer have a very strong impact on the distribution of turbulence in the planetary boundary layer. However these are only two cases with very little amount of

clouds. It is therefore necessary to do more measurements and analysis of a cloud topped convective planetary boundary layer to get more stable results. Measurements with the WindTracer Doppler lidar have been done during the CSIP (Blyth and Bennett, 2005) campaign in southern England in summer 2005. Some data sets with convective cumulus clouds in the boundary layer were obtained. But time was too short to include these data into this work.

8.4.4 Comparison with literature

In the previous sections the profiles of the standard deviation of the vertical wind σ_w were displayed. In the past σ_w profiles have been obtained from other experiments and therefore some results shall be compared in this section.

The most commonly used data is that gathered in the field experiments in Ashchurch, Worcestershire during July 1976 (Caughey and Palmer, 1979) and the so called Minnesota experiment from 1973 (Izumi and Caughey, 1976). These experiments still today form the basis of work on atmospheric boundary layer.

Caughey and Palmer (1979) combined the data from the two experiments mentioned above. Although the data was gathered over different terrain, no significant error which could be tracked to the surface condition was registered. The display of the σ_w profile is some what different than that used in this work, therefore the important profiles shall be displayed again this time using the scaling as was used by Caughey and Palmer. The main difference is that $\sigma_w^2/w_\star^2$ was used instead of $\sigma_w/w_\star$. Also for the abscissa a logarithmical scaling is used.

In Figure 41 the vertical profile of the normalised vertical velocity variance on the basis of the above mentioned data is displayed. The dashed line is from the work of Willis and Deardorff (1974), it represents the average of two cases in a laboratory experiment. For comparison into the plots of the lidar data this line was drawn based on the formula given by Kaimal and Finnigan (1994):

$$\frac{\sigma_w^2}{w_\star^2} = 1.8 \left(\frac{z}{z_i}\right)^{\frac{2}{3}} \left(1 - 0.8\frac{z}{z_i}\right)^2 \tag{9}$$

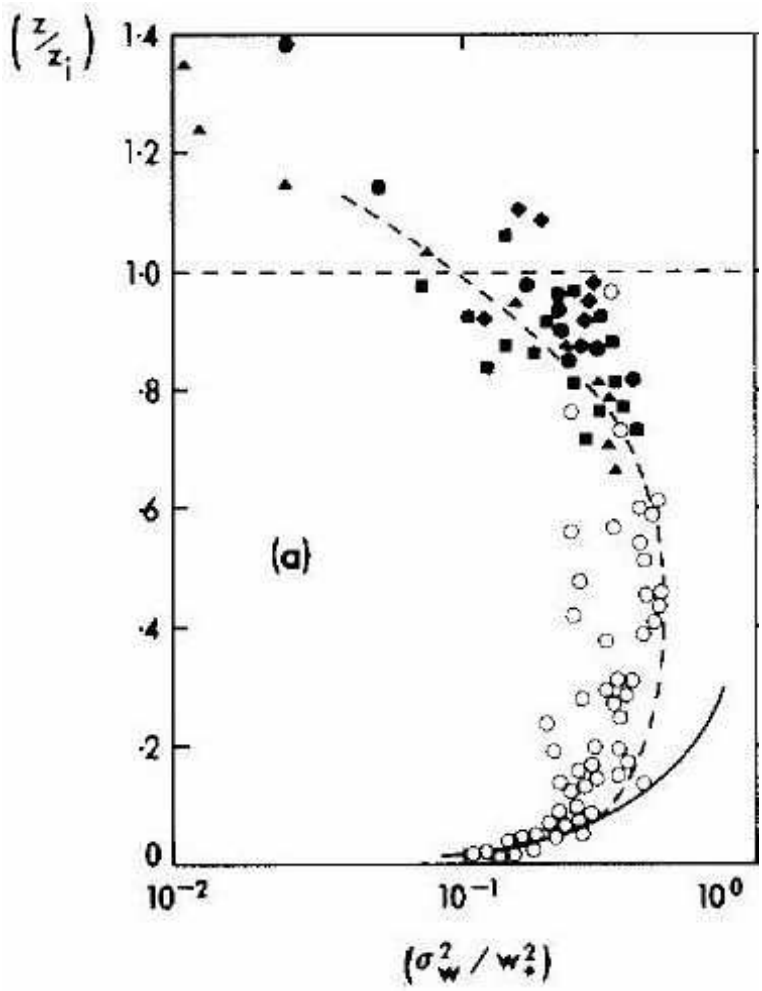

Figure 41: Normalised vertical velocity variance $\sigma_w^2/w_\star^2$. The solid line is the free convection prediction, the dashed line is from the work of Willis and Deardorff (1974) and represents the average of two cases in a laboratory experiment (Caughey and Palmer, 1979).

The solid line in Figure 41 is the free convection prediction:

$$\frac{\sigma_w^2}{w_\star^2} = 1.8 \left(\frac{z}{z_i}\right)^{\frac{2}{3}} \tag{10}$$

As before three different stages of the boundary layer will be looked at, starting in the morning with the developing boundary layer (Fig. 42). The first two hours show a very good agreement with the plotted line. Only in the top third of the boundary layer the data of the second hour is a little higher than the corresponding line, but still the general form of the profile is similar.

In the fully developed boundary layer the concordance between the plotted line and the measured values is not as good as in the morning hours.

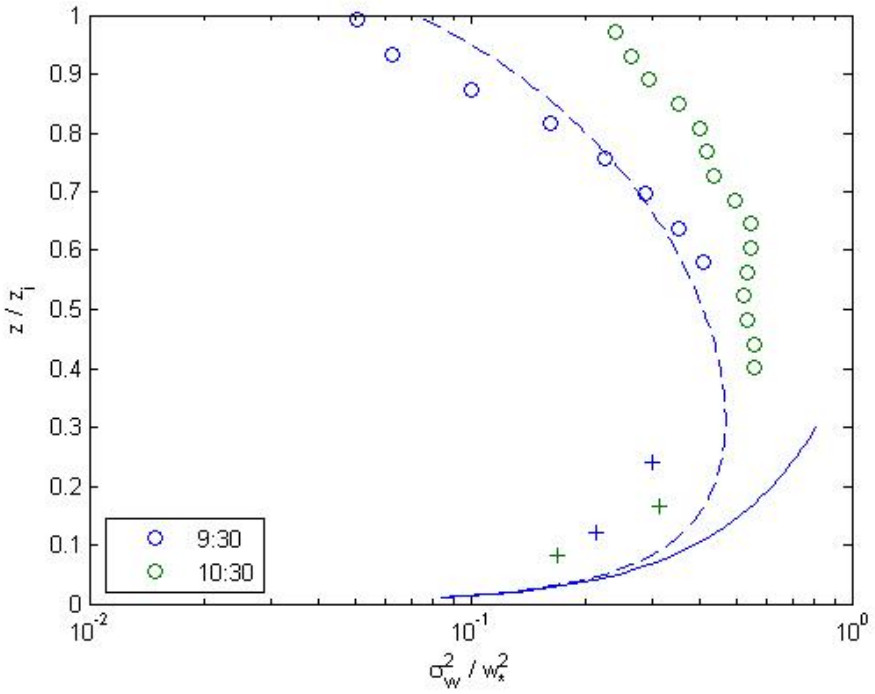

Figure 42: Profile of $\sigma_w^2/w_\star^2$ on August 2, 2004 from 08:30 to 10:30 UTC, in a developing mixing layer. Lidar data (circles) and data from the 200 m tower of the FZK (crosses). Solid line free convection prediction, dashed line from Willis and Deardorff (1974).

Although the profiles vary in the x-direction they show a similar devolution, with a maximum just below the middle of the mixing layer and then a steady decrease to the top of the boundary layer (Fig. 43). The line Willis and Deardorff found in their laboratory experiments has its maximum at 0.3 z_i, about the same height as the measured profiles. The decrease towards the top of the boundary layer then is a little faster compared to the measured lidar profiles. Although the concordance between the profile of Willis and Deardorff and the lidar measurements is not so good as in the morning hours, comparing Figure 43 with Figure 41 shows that in Figure 41 the measured values are lower than the dashed line, similar to the lidar measurements. And that in the upper boundary layer some measurements are larger than the dashed line of Willis and Deardorff.

The third comparison is that for a convective boundary layer with clouds present (Fig. 44). These are the two profiles at midday using data from 11:30 to 13:30 UTC. An agreement with the Figure from Caughey and Palmer can only be found in the lowest part of the planetary boundary layer up to roughly 0.3 z_i. From thereon the two lidar profiles develop significantly different than the lines of Willis and Deardorff. Other than

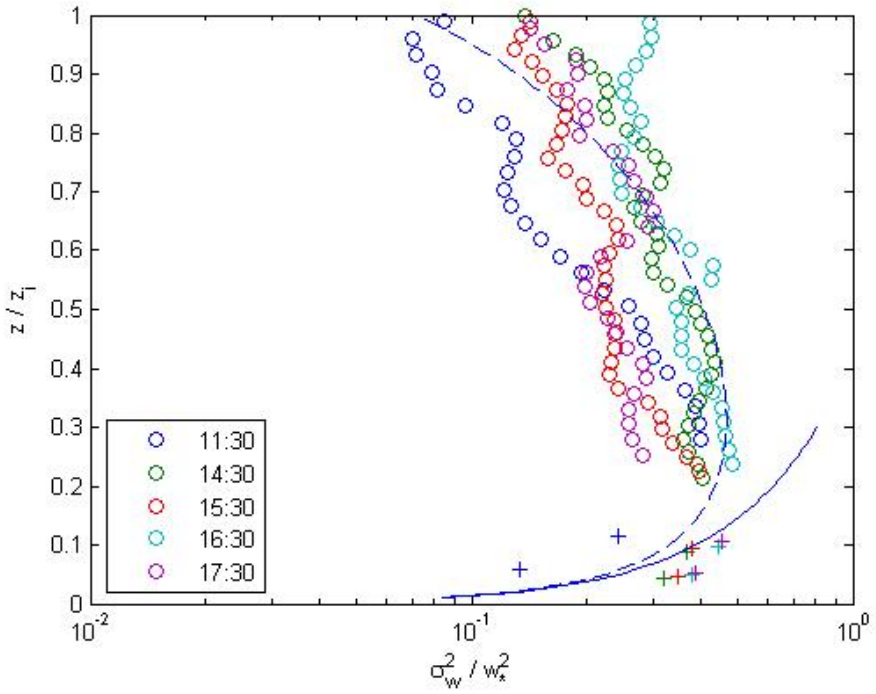

Figure 43: Profile of $\sigma_w^2/w_\star^2$ on August 2, 2004, in a fully developed mixing layer. Lidar data (circle) and data from the 200 m tower of the FZK (stars). Solid line free convection prediction, dashed line from Willis and Deardorff (1974).

the profiles before and the profiles in the literature, these two profiles do not decrease towards the top of the boundary layer, but instead are constant from the middle of the mixing layer.

The measured profiles of the normalised variance is strongly dependent on the condition the planetary boundary layer is in. The data found in the literature generally is only for well developed boundary layers without clouds. Therefore the comparison between literature data and lidar data for the developed boundary layer without clouds is very good. The lidar data shows similar profiles as e.g. the data acquired in Minnesota and Ashchurch. The agreement with the laboratory profiles of Willis and Deardorff is not so good, but the data gained in Minnesota and Ashchurch shows the same differences. A better agreement show the profiles for the developing mixing layer. No data in the literature was found. Hardly any agreement with laboratory data exists for cases when clouds are present in the fully developed planetary boundary layer. It seems that the laboratory data is fine for the developed mixing layer, even better for the developing mixing layer but not applicable for cloudy periods.

Some methods for modelling the cloud topped boundary layer are de-

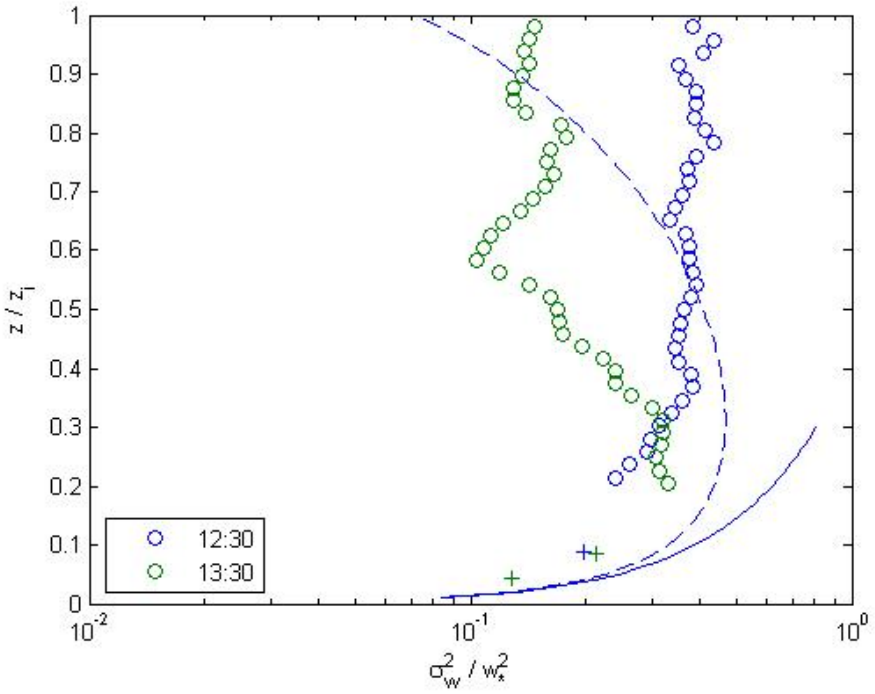

Figure 44: Profile of $\sigma_w^2/w_\star^2$ on August 2, 2004 from 11:30 to 12:30 UTC, in a fully developed mixing layer, with clouds present. Lidar data (circle) and data from the 200 m tower of the FZK (stars) Solid line free convection prediction, dashed line from Willis and Deardorff (1974).

scribed e.g. in Garrett (1992). But these parameterisations are mostly for fluxes, especially concerning humidity fluxes and distribution within the convective boundary layer. With the measured data from the Doppler lidar only the vertical motion is available. This means that no fluxes can be calculated, for this further measurements, e.g. with Raman or DIAL lidars to obtain humidity and temperature data is necessary. The combination of these different lidar systems and cloud radar would enable measurement of fluxes in the cloud topped boundary layer.

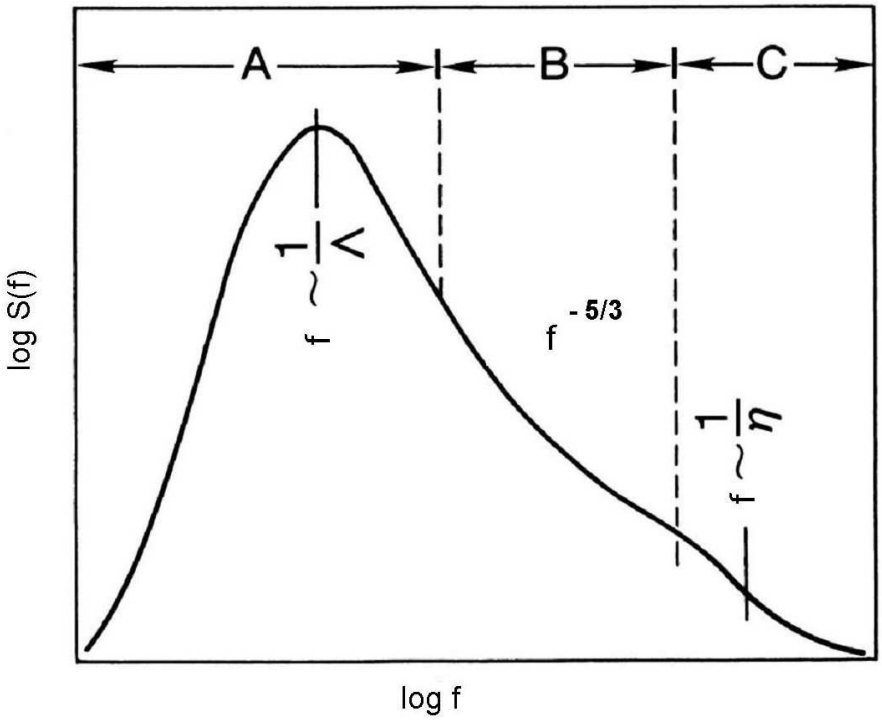

Figure 45: Schematic of energy spectrum in the atmospheric boundary layer showing distinct regions of energy production (A) and dissipation (C) and the inertial subrange (B). Λ is the integral scale of turbulence and η is the Kolmogorov microscale (after Kaimal and Finnigan 1994).

9 Energy spectra of turbulence

9.1 The power spectrum

In the power spectrum the variance of a quantity is displayed according to the size of the eddies. The spectral energy density $S_A(f)$ specifies the share of the discrete infinitesimal frequencies f in the total variance of the spectra. $S_A(f)$ in stationary conditions corresponds to the part of the total variance of a fourier transformed time series (Stull, 1988):

$$\sigma_A^2 = \int_f S_A(f) df \tag{11}$$

Three main ranges exist in a spectrum (Fig. 45):

Energy-containing range (A): In this frequency range energy is created by buoyancy and shear. The integral scale Λ describes the size

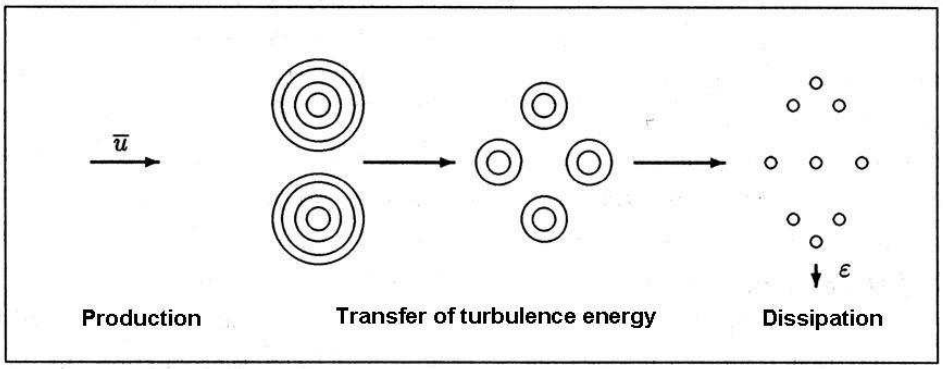

Figure 46: In the energy cascade kinetic energy from the horizontal flow is withdrawn and dissipated through ever smaller eddies into turbulent energy and finally into inner energy (heat) (adapted from Etling, 1996).

and typical diameter of eddies, where the main part of energy is present and most turbulences occur (Kaimal and Finnigan 1994). The lower frequencies have the largest influence on the total variance.

Inertial subrange (B): Here no further production of energy takes place and no energy is lost due to dissipation. In the inertial subrange energy is transferred from small frequencies to higher frequencies (Fig. 46). In this range the turbulence is isotropic which means that the turbulent elements have no favoured direction. According to Kolmogorov (1941) the energy density decreases with $f^{-\frac{5}{3}}$ towards higher frequencies. Multiplying the energy spectrum with the frequency results in a -2/3 decrease. Doing this the unit is then $m^2\, s^{-2}$, the same as for the energy. This well known power law for the inertial subrange is the basis for calculation of theoretical model spectra.

Dissipation range (C): At very high frequencies the remaining eddies disintegrate and the kinetic energy is converted to internal energy through molecular friction. The Kolmogorov micro scale (Foken, 2003)

$$\eta = \left(\frac{\nu^3}{\varepsilon}\right)^{\frac{1}{4}} \tag{12}$$

shows the dimension of the eddies when they dissipate.

When calculating the spectrum averaging times and measurement frequencies have to be chosen carefully. On one hand the averaging time

has to be long enough so that all relevant factors are included, on the other hand the time period should be not too long so that stationarity is given, e.g. averaging over a whole day is normally no use as diurnal changes can come into play. Additionally the sampling frequency has to be high enough to ensure that processes with small frequencies are resolved.

A connection between frequency and eddy size is made with the Taylor hypothesis. The main physical statement is that the life time of the turbulent structure is larger than the time it takes to pass by the measuring instrument (frozen turbulence). From this the following two equations result:

$$\lambda = \frac{U}{f}, \qquad k = \frac{1}{\lambda} = \frac{f}{U} \tag{13}$$

were λ is the wave length in m, U is the mean horizontal wind speed in $m\,s^{-1}$, f is the frequency in Hz and k is the wave number in $1/m$.

9.2 Spectra of the vertical wind

The vertical wind velocity data from vertically pointing lidar measurements discussed in the previous chapters are used in this section to determine power spectra. For calculating the power spectra an averaging time of one hour was chosen, which is generally seen as the response time of the boundary layer. Also a height averaging was performed. Three height areas were defined in accordance to the height of the boundary layer. These intervals were chosen to be $0.2 - 0.5\ z_i$, $0.5 - 0.7\ z_i$ and $0.7 - 1\ z_i$. Doing this it was hoped, that a change in the spectrum relative to the height would appear (Kaimal et al., 1976).

The fast fourier transformation of the time series was done using numerical recipes routines (Press et al., 1992). The linear trend was removed, the spectrum was normalised with the variance and finally multiplied with the frequency.

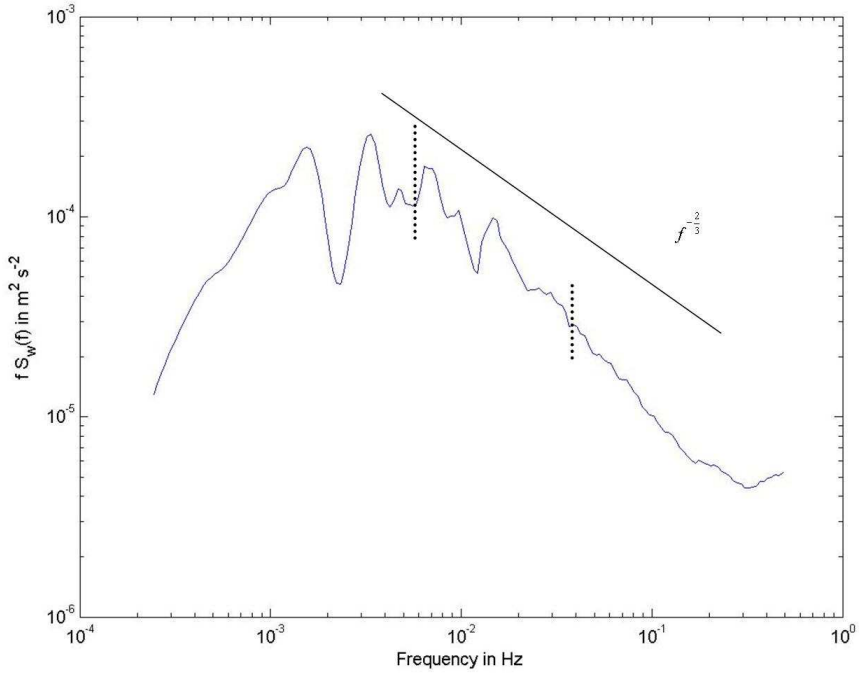

Figure 47: Power spectrum from August 2, 2004 11 UTC, for height range 0.7 $z_i - 1$ z_i. The dotted line marks the interval of the inertial subrange where a decrease of $f^{-\frac{2}{3}}$ takes place.

9.2.1 The inertial subrange

One of the interesting parts of the power spectrum is the inertial subrange were the energy is transferred from low to high frequencies. If the data acquired by the Doppler lidar complies with the theory of Kolmogorov an inertial subrange with a decrease of $f^{-\frac{2}{3}}$ should be found, as the spectrum was multiplied with the frequency.

The examples in fig 47, 48 and 49 taken at the same time but at different heights show this inertial subrange very clearly. In the highest range (Fig. 47) the inertial subrange is from $6 \cdot 10^{-3}$ to $4 \cdot 10^{-2}$. In the middle range (Fig. 48) it is from $4 \cdot 10^{-3}$ to $2 \cdot 10^{-2}$ and in the lowest range (Fig. 49) from $6 \cdot 10^{-3}$ to $3 \cdot 10^{-2}$. Towards higher frequencies the drop is faster than the $f^{-\frac{2}{3}}$ law. This is because the lidar can not resolve all of the small eddies. The temporal resolution would enable to detect these eddies but the spatial resolution with a range gate length of 80 m is too big. Some power spectra show an increase in the highest frequency regions, this is due to measurement errors and random noise.

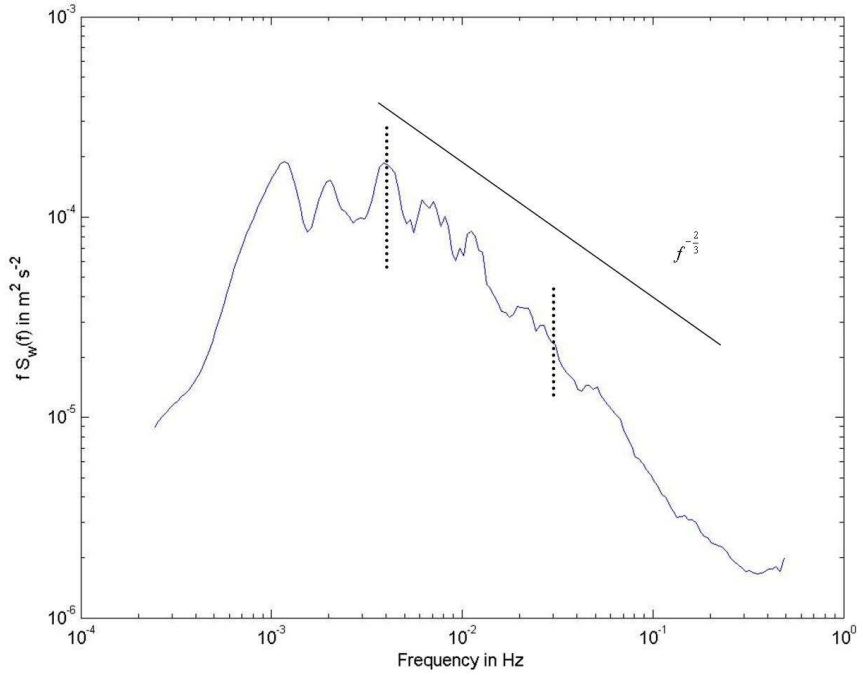

Figure 48: Power spectrum from August 2, 2004 11 UTC, for height range $0.5\ z_i - 0.7\ z_i$. The dotted line marks the interval of the inertial subrange where a decrease of $f^{-\frac{2}{3}}$ takes place.

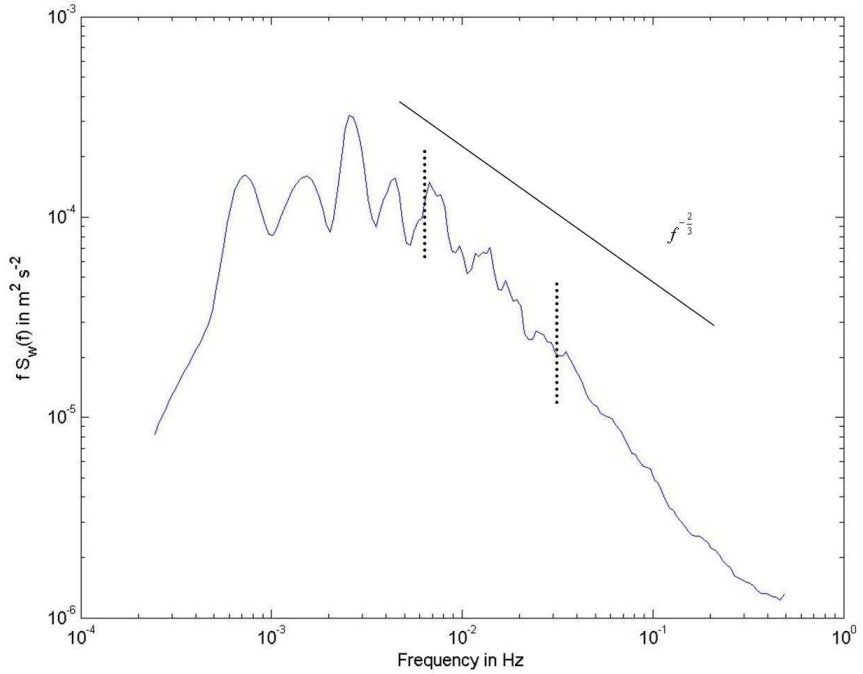

Figure 49: Power spectrum from August 2, 2004 11 UTC, for height range $0.2\ z_i - 0.5\ z_i$. The dotted line marks the interval of the inertial subrange where a decrease of $f^{-\frac{2}{3}}$ takes place.

9.2.2 Energy maximum

The energy spectrum has an energy maximum in the energy containing range (A), see Figure 45. This maximum in the energy producing part of the spectrum is height dependent. Especially in the lowest parts of the planetary boundary layer a significant shift in the position of the maximum can be detected (Fig. 50), not only position but also in the amount of energy.

Figure 50 also shows that the shift for the vertical component (c) is much more significant than that for the horizontal components (a, b). The biggest shift for the vertical component is in the lowest part of the planetary boundary layer for $z_i < 0.2$. Measurements in this region are mostly done by tower mounted instruments. The Windtracer Doppler lidar can not measure in these low regions. In a fully developed boundary layer, measurements start at approx. 0.2 z_i. In the morning hours for example no measurements below 0.5 z_i could be performed.

A study to determine whether the maximum in the lidar data behaves similar to that in the Figure of Kaimal et al. (1976) is therefore not very promising. The figures 47 to 49 show no sign of a systematic increase or shift of the energy maximum.

In the work of Caughey and Palmer (1979) concerning the Minnesota experiment and that at Ashchurch, they discovered, that for regions above 0.8 z_i the category for the height range 0.2 z_i to 1.0 z_i defined by Kaimal et al. (1976) was not appropriate. To study this further they chose the variation of peak wavelength in the spectrum of the vertical velocity component (Fig. 51). This was done throughout the boundary layer so the lidar data measured at the FZK can be compared better with this than with the Figure of Kaimal et al. (1976).

In order to see if the spectra measured by the CLR Doppler lidar behaved similar to those of Caughey and Palmer two cases were studied. As described in section 7.2.2 during two hours of measurement clouds passed over the lidar. For this reason the spectra of the fully developed boundary layer were divided into a cloudy and cloud free period, as described in section 8.4.3. Additionally the spectra were averaged over those two periods, providing two sets of spectra divided up into the three height intervals mentioned above. Then the peak wavelength of every interval

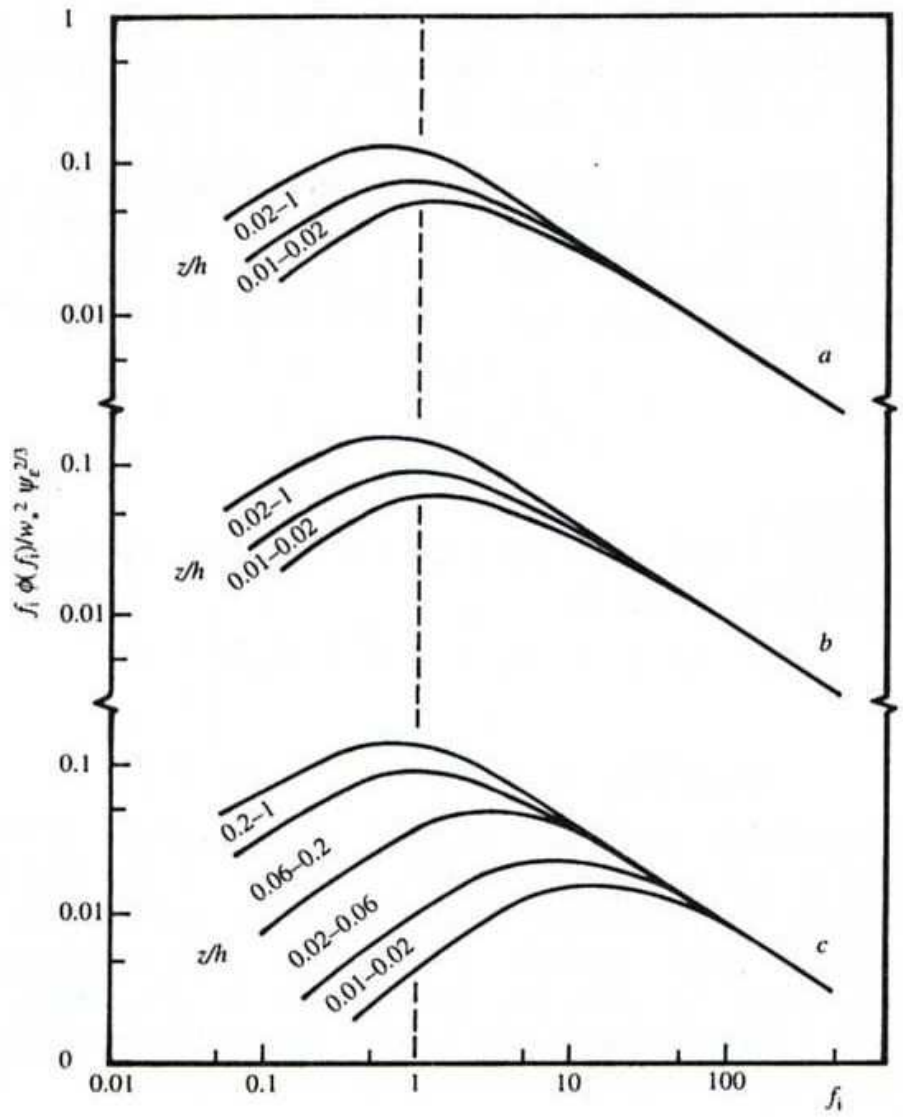

Figure 50: One-dimensional velocity spectra in the mixed layer, suitably nondimensionalised according to mixed-layer scaling arguments, and plotted as function of the normalised frequency $f_i = nh/u$. The ranges of values of z/h are indicated. (a) u-component spectrum, (b) v-component spectrum, (c) w-component spectrum. After Kaimal et al. (1976).

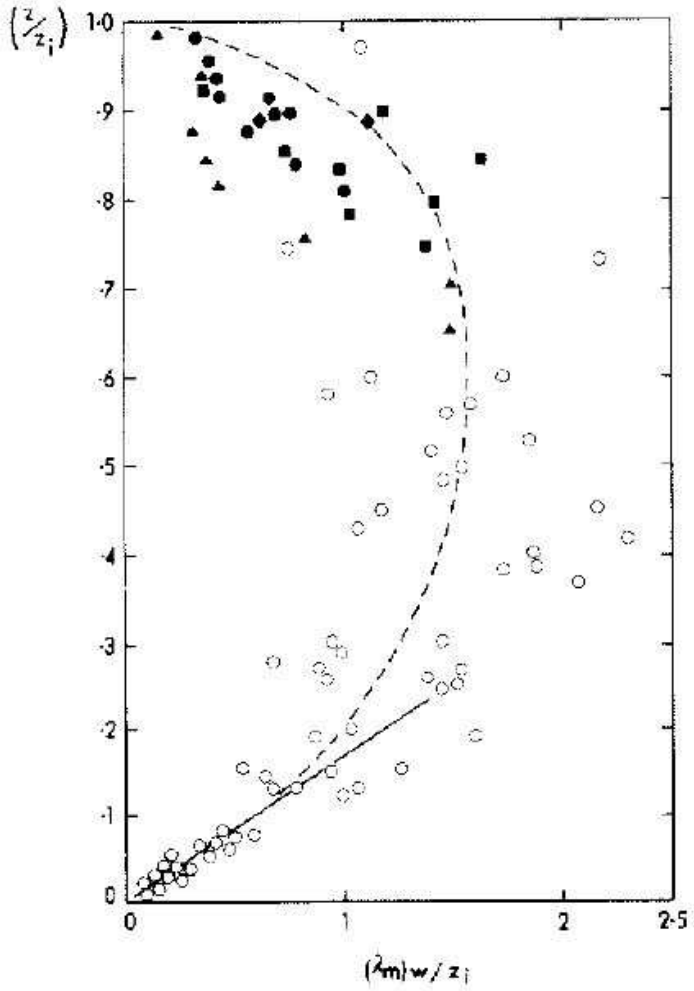

Figure 51: The variation of normalised peak wavelength for the vertical velocity component with z/z_i. The solid line represents the free convection prediction, $(\lambda_m)_w/z_i = 5.9z/z_i$ and the dashed line, representing the relationship $(\lambda_m)_w/z_i = 1.8z_i(1 - exp(-4z/z_i) - 0.0003exp(8z/z_i))$, provides a fairly good fit to the data in the range $0.1z_i \leq z < z_i$ (Caughey and Palmer, 1979).

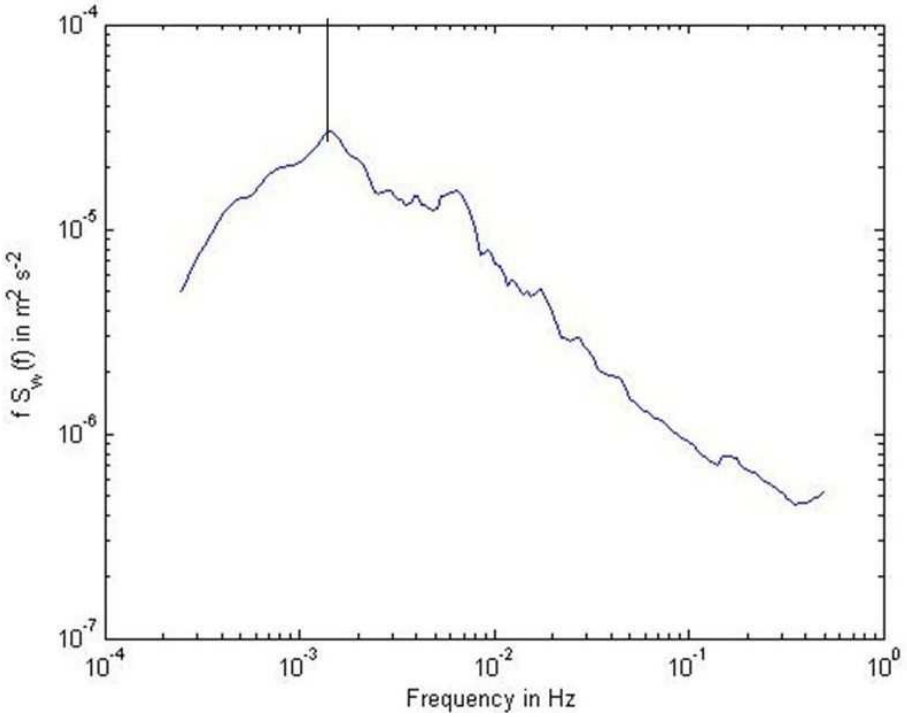

Figure 52: Power spectrum for height interval $0.7\ z_i - 1\ z_i$ for cloud free period.

was detected by visual interpretation. Finally the peak wavelength was normalised with the boundary layer height z_i.

In the figures 52 to 54 the results for the cloud free periods can be seen. The spectra in the cloud free conditions show a significant shift of the energy maximum in the frequency. In the highest interval from $0.7 - 1\ z_i$ The second largest peak wavelength with a frequency of $1.5 \cdot 10^{-3}\ Hz$ or a normalised wavelength of 0.68 is found. In the range from $0.5 - 0.7\ z_i$ the greatest peak wavelength is detected at a frequency of $8 \cdot 10^{-4}\ Hz$ complying to a normalised wavelength of 1.27. And finally the smallest wavelength is found in the lowest interval $(0.2 - 0.5\ z_i)$ at a frequency of $2.1 \cdot 10^{-3}\ Hz$ with a normalised wavelength of 0.48. This complies very well with the data from Caughey and Palmer, where the greatest peak wavelengths are also found in the region of $0.5 - 0.7\ z_i$.

A very different picture occurs for the cloudy period (Fig. 55 to 57). Here the smallest peak wavelength is recorded in the height interval at the top of the boundary layer, just beneath or in the clouds with a frequency of $3.1 \cdot 10^{-3}\ Hz$ and a wavelength of 0.33. The next larger wavelength is found in the middle interval of $0.5 - 0.7\ z_i$ with a frequency of $2.3 \cdot 10^{-3}\ Hz$ and a wavelength of 0.44. And the wavelength in the lowest interval of $0.2 - 0.5\ z_i$ is roughly the same as in the cloud free

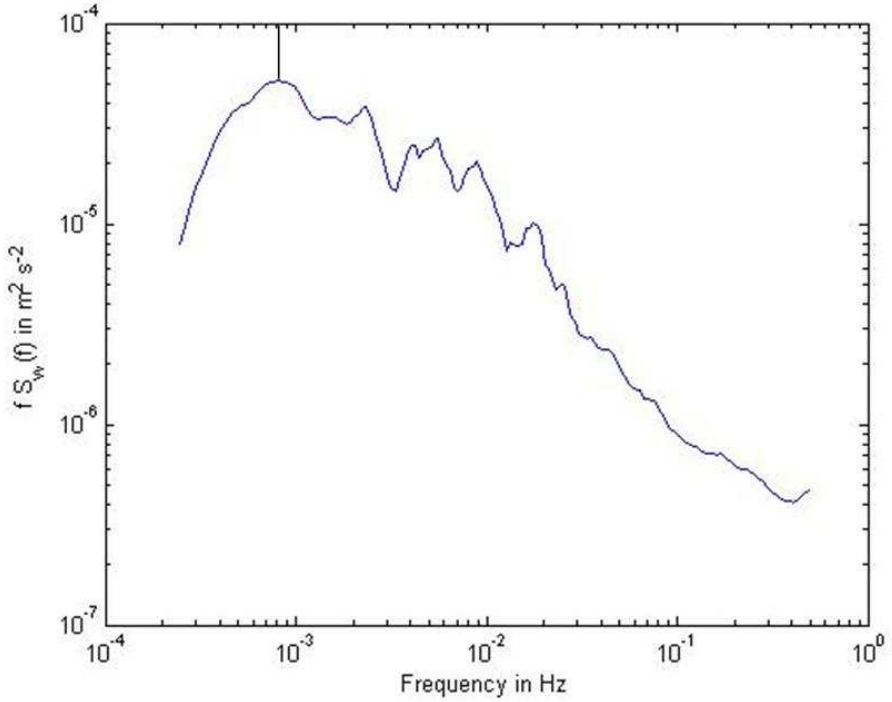

Figure 53: Power spectrum for height interval $0.5\ z_i - 0.7\ z_i$ for cloud free period.

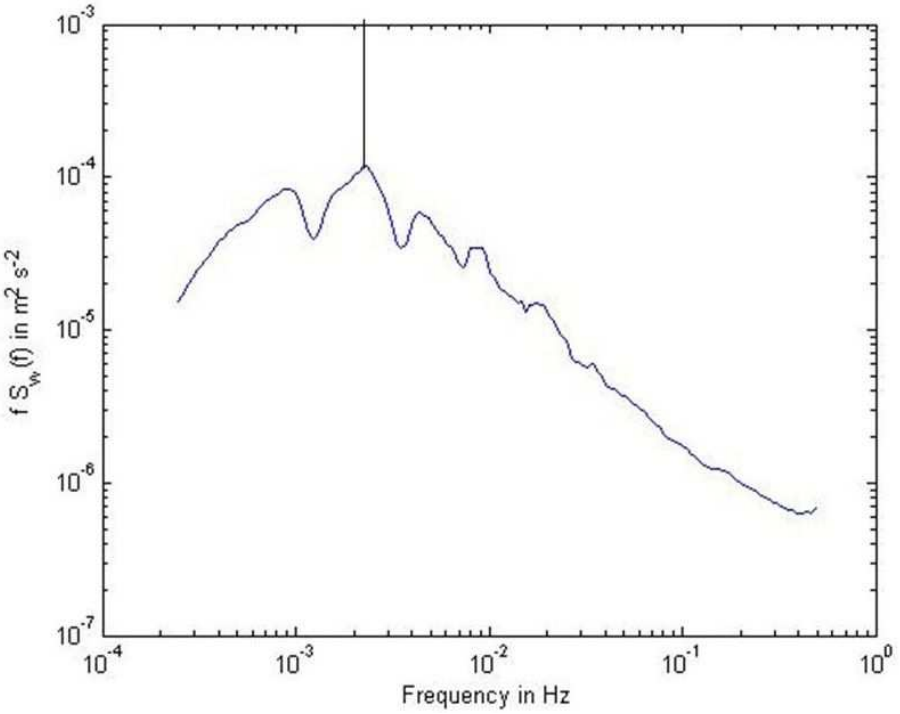

Figure 54: Power spectrum for height interval $0.2\ z_i - 0.5\ z_i$ for cloud free period.

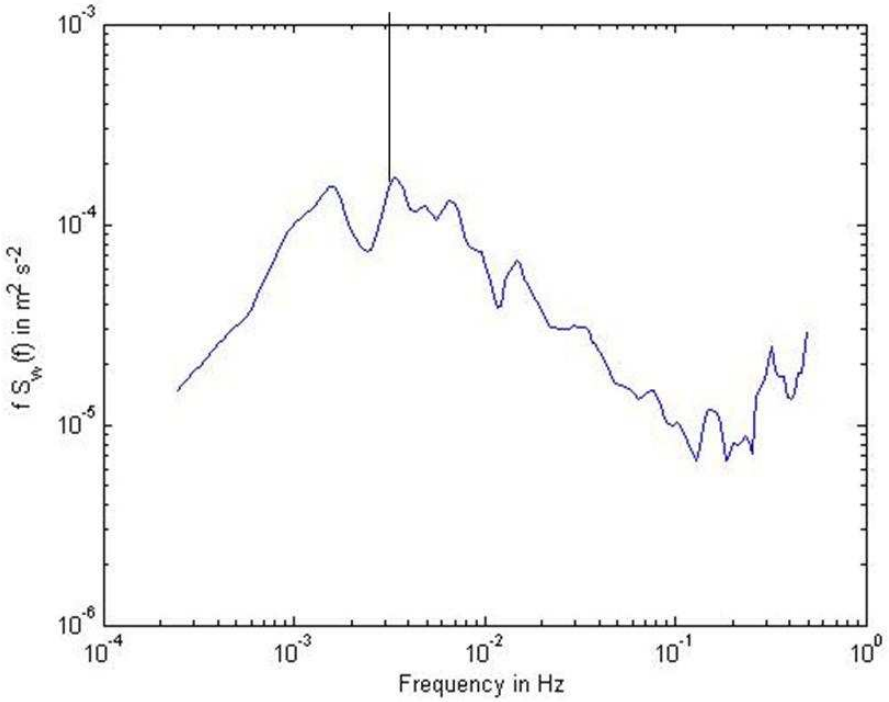

Figure 55: Spectrum for height interval 0.7 $z_i - 1$ z_i for cloudy period.

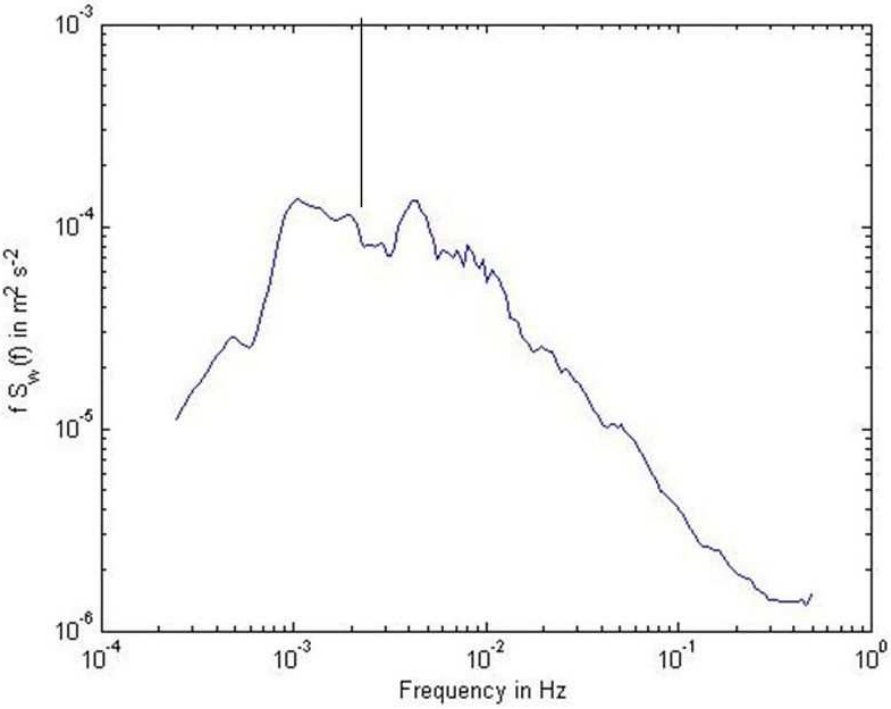

Figure 56: Spectrum for height interval 0.5 $z_i - 0.7$ z_i for cloudy period.

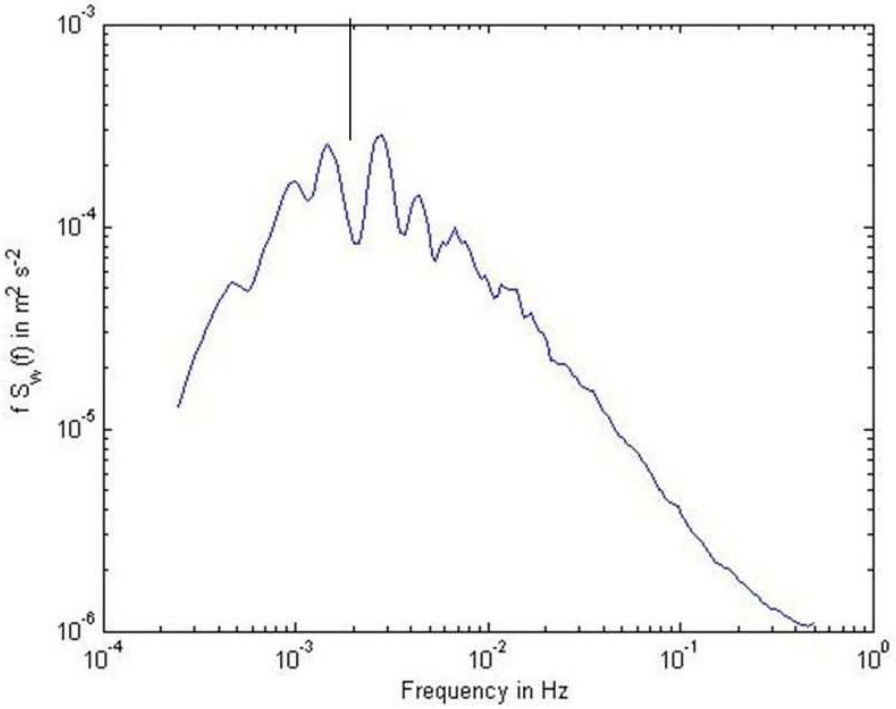

Figure 57: Spectrum for height interval $0.2\ z_i - 0.5\ z_i$ for cloudy period.

period with frequency of $2.0 \cdot 10^{-3}\ Hz$ and a wavelength of 0.51. Thus the influence of the clouds reach as far down as the middle of the boundary layer.

The peak wavelengths are shown in Figure 58. For the cloud free period the vertical distribution is similar to the results found by Caughey and Palmer (1979). The cloudy periods however show a significantly different distribution. Especially the maximum peak wavelength is no longer found in the middle of the planetary boundary layer. This means that the portion of small scale turbulence has increased in the middle of the boundary layer when convective cumulus clouds are present. However, as stated in section 8.4.3 these were only two cases with clouds. For a more reliable basis more data sets of convective clouds have to be recorded an analysed.

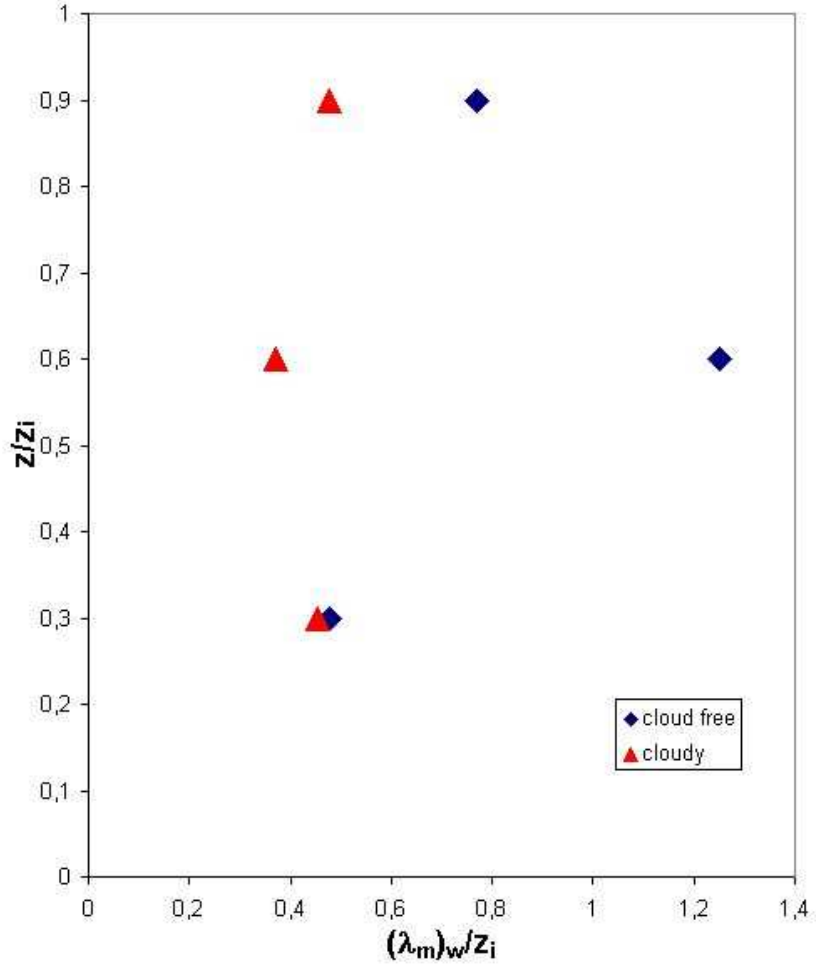

Figure 58: Peak wave lengths for three height intervals and two cases. The blue diamonds indicate the cloud free period and the red triangles the cloudy period.

10 Conclusion and Outlook

In this diploma thesis data sets from a coherent Doppler lidar were analysed. The work includes measurements with the CLR Photonics Windtracer and data from the sonic anemometers on the 200 m tower at the Forschungszentrum Karlsruhe. From the 200 m tower 10 minute mean and turbulent values were used. The Doppler lidar measures the radial wind velocity using a coherent pulsed laser at a wavelength of 2 μm. Several measurements during the summer months of 2004 were done, for this work data from two days in August 2004 was used. On August 2 measurements with a vertical pointing laser without rotation were done. On August 5 ppi scans with five different elevation angles were carried out.

The aim of the work was to test the ability and performance of the CLR WindTracer Doppler lidar for turbulence measurements in the convective planetary boundary layer. Different scanning methods were tested to derive information on the turbulence and turbulent structures in the planetary boundary layer.

To obtain the three wind components u, v and w out of one ppi scan the VAD algorithm was used. With this method the mean horizontal wind speed and direction as well as the mean vertical wind speed for each ppi scan was derived. For the purpose of identifying turbulent structures the w component of every beam was calculated. Using the Matlab programm a graphical display of the vertical wind speed was done. For one height the w component was displayed in a plan view plot at the position relative to the lidar were they were measured. With a Delaunay triangulation an interpolation of the data was tried. The received results were not very promising. Two aspects have to be considered. Firstly the elevation angle of the two inner circles is too high, the influence of the horizontal wind on the radial wind velocity might be overestimated and therefore the calculation of the w component incorrect. Secondly, and more important, the elapsed time between first and last scan is approx. 5 minutes, this means the horizontal drift of the structures has to be considered. The problem is that the horizontal drift of the turbulent structures in comparison of the horizontal wind speed is not known. Therefore further measurements with other scan strategies have to be performed. A detailed description of a possible scan technique is given in section 6.3. The basic idea is that scans orthogonal to the main wind

direction should be performed and that the turbulent structures can be measured while passing by the lidar. Doing this possibly a relation for horizontal wind speed and turbulent drift can be found.

The second part of the analysis used the data from August 2 when only the vertical wind component was measured, by pointing the laser vertically upwards. The development of the convective planetary boundary layer could be derived very clearly from the lidar data. The combination of signal to noise ratio and vertical wind speed showed the development in the morning, when the vertical extension of the mixing layer is closely connected with updrafts in the wind field, resulting in a pulsation of the developing boundary layer. During midday single clouds passed over the lidar and were analysed separately. The analysis of the σ_w profiles and of the energy spectra in different heights showed, that the presence of clouds had a great influence on the turbulent state of the upper and middle planetary boundary layer. But also the life cycle of the cloud is important, forced cumulus clouds in the early stages are connected with strong upward winds underneath and in the base of the clouds. Passive clouds towards the end of their life cycle however have no connection with the underlying boundary layer and no influence on vertical wind speeds and turbulence. However there is very little data available with the presence of clouds. In order to do a more thorough analysis of the cloud topped convective planetary boundary layer more measurements are necessary. These first results anyhow are very promising that new information about the behaviour of the turbulent boundary layer can be obtained. To get more information concerning fluxes the simultaneous measurements with other lidars (e.g. Raman or DIAL) is necessary. The combination of wind data with humidity and temperature information would be very helpful to understand more about the processes in the cloud topped convective boundary layer, e.g. in terms of parameterisations of atmospheric processes.

The performance of the CLR WindTracer lidar was very satisfactory. The Doppler lidar is a very good instrument for performing measurements in the convective middle and upper boundary layer. The lower part up to approx. 450 m can not be measured, as the lidar can only start measuring at a distance of 400 m. No problems with the lidar performance occurred during the measurements for this thesis. The data recording was stable and reliable. For this thesis lidar data with 1 Hz was used, it is however possible to increase the measurement to 10 Hz.

For the middle and upper planetary boundary layer the Doppler lidar is an ideal instrument to measure wind velocities with a high temporal and spatial resolution.

11 References

Barthlott, C., 2003: *Kohärente Wirbelstrukturne in der atmosphärischen Grenzschicht.* Wiss. Berichte Meteor. Inst. Univ. Karlsruhe, **33**, 128 pp.

Blackadar, A. K, 1997: *Turbulence and Diffusion in the Atmosphere: Lectures in Environmental Sciences*, Springer-Verlag Berlin, Heidelberg, 185 pp.

Blyth, A., L. Bennett, 2005: *CSIP operations plan*, University of Leeds, 66 pp.

Boers, R., and E.W. Eloranta, 1986: Lidar measurements of the atmospheric entrainment zone and the potential temperature jump across the top of the mixed layer. *Boundary-Layer Meteorol.*, **34**, 357-375.

Bollig, C., R. A. Hayward, W. A. Clarkson, D. C. Hanna, 1998: 2-W Ho:YAG laser interactivity pumped by a diode-pumped Tm:YAG laser. *Opt. Lett.* **23** (22), 1757-1759.

Browning, K. A., R. Wexler, 1968: The Determination of Kinematic Properties of a Wind Field Using Doppler Radar. *J. Appl. Meteor.*, **7**, 105-113.

Carson, D. J., 1973: The development of a dry inversion-capped convectively unstable boundary layer. *Quart. J. Roy. Meteor. Soc.*, **99**, 450-467.

Carswell, A. I., A. Fong, S. R. Pal, I. Pribluda, 1995: Lidar-Derived Distribution of Cloud Vertical Location and Extent. *J. Appl. Meteor.*, **34**, 107-120.

Caughey, S. J., S. G. Palmer, 1979: Some aspects of turbulence structure through the depth of the convective boundary layer. *Quart. J. R. Met. Soc.*, **105**, 811-827.

Clements, W. E., J. A. Archuleta, P. H. Gudiksen, 1989: Experimental Design of the 1984 ASCOT Field Study. *J. Appl. Meteor.*, **28**, 405-413.

CLR Photonics, 2002: *WindTracer System Operation User Manual*, 154 pp.

Deardorff, J. W., 1972: Numerical investigation of neutral and unstable planetary boundary layers. *J. Atmos. Sci.*, **29**, 91-115.

Deardorff, J. W., 1970: Convective velocity and temperature scales for the unstable planetary boundary layer and for Rayleigh convection. emphJ. Atmos. Sci., **27**, 1211-1213.

Driedonks, A. G. M., P. G. Dynkerke, 1989: Current problems in the stratocumulus-topped atmospheric boundary layer. *Boundary Layer Meteor.*, **46**, 275-303.

Etling, D., 1996: *Theoretische Meteorologie.* Friedr. Vieweg & Sohn Verlagsgesellschaft mbH, Braunschweig, Wiesbaden, 318 pp.

Fiedler, F., T. Prenosil, 1980: *Das MESOKLIP-experiment, mesoskaliges Klimaprogramm im Oberrheintal.* Wiss. Berichte Meteor. Inst. Univ. Karlsruhe, **1**, 107 pp.

Fiedler, F., H. A. Panofsky, 1970: Atmospheric scales and spectral gaps. *Bull. Am. met. Soc.*, **51**, 1114-1119.

Flamant, C., J. Pelon, 1996: Atmospheric Boundary-Layer Structure over the Mediterranean during a Tramontane Event. *Quart. J. R. Met. Soc.*, **122**, 1741-1778.

Flesia, C., C. L. Korb, C. Hirt, 2000: Double-edge molecular measurement of lidar wind profiles at 355 nm. *Opt. Lett.*, **25**, 1466-1468.

Foken, T., 2003: *Angewandte Meteorologie. Mikrometeorologische Methoden.* Springer-Verlag, Berlin, 289 pp.

Garratt, J. R., 1992: *The atmospheric boundary layer.* Cambridge University Press, Cambridge, 316 pp.

Gentry, B. M., H. Chen, S. X. Li, 2000: Wind measurements with 355-nm molecular Doppler lidar. *Opt. Lett.*, **25**, 1231-1233.

Grund, C. J., R. M. Banata, J. L., George, J. N. Howell, M. J. Post, R. A. Richter, A. M. Weickmann, 2000: High-Resolution Doppler Lidar for Boundary Layer and Cloud Research. *J. Atmos. Oceanic Technol.*, **18**, 376-393.

Haugen, D. A, J. C. Kaimal, E. F. Bradley, 1971: An experimental study of Reynolds stress and heat flux in the atmospheric surface layer. *Quart. J. Roy. Meteor. Soc.*, **97**, 168180.

Henderson, S. W., C. P. Hale, J. R. Magee, M. J. Kavaya, A. V. Huffaker, 1991: Eye-safe coherent laser radar system at 2.1 μm using Tm,Ho:YAG lasers. *Opt. Lett.*, **16** (10), 773-775.

Hooper, W. P., E. W. Eloranta, 1986: Lidar measurements of wind in the planetary boundary layer: The method, accuracy and results from joint measurments with radiosonde and kytoon. *J. Climate Appl. Meteor.*, **25**, 990-1001.

Izumi, Y. and S. J. Caughey, 1976: Minnesota 1973 atmospheric boundary layer experiment data report, AFGL Environmental Research paper No. 547.

Kaimal, J. C., J. J. Finnigan, 1994: A*tmospheric Boundary Layer Flows.* Oxford University Press, 289 pp.

Kaimal, J. C., J. E. Gaynor, 1982: The Boulder atmospheric observatory. *J. Appl. Meteor.*, **22**, 863-880.

Kaimal, J. C., J. C. Wyngaard, D. A. Haugen, O. R. Cote, Y. Izumi, S. J. Caughey, C. J. Readings, 1976: Turbulence Structure in the Convective Boundary Layer. *J. Atmo. Sci.*, **33**, 2152-2169.

Kalthoff, N., B. Vogel, 1992: Counter current and channelling effect under stable stratification in the area of Karlsruhe. *Theor. Appl. Climatol.*, **45**, 113-26.

Kane, T. J., W. J. Kozlowsky, R. L. Byer, and C. E. Byvik, 1987: Coherent laser radar at 1.06 μm using Nd:YAG lasers. *Opt. Lett.* **12**, 239-241.

Kolmogorov, A. N., 1941: The local structure of turbulence in an incrompressible fluid for very large Reynolds numbers. *Dokl. Akad. Nauk. SSSR*, **30**, 301-305.

Lettau, H. H., B. Davidson, 1957: *Exploring the atmosphere's first mile.* Pergamon Press, London, New York and Paris, 2 vols.

Lettau, H., 1939: *Atmosphärische Turbulenz.* Akademische Verlagsgesellschaft, Leipzig.

Lhermitte, R. M., D. Atlas, 1961: Precipitation motion by pulse Doppler. Proc. 9^{th} Weather Radar Conf., Boston, Amer. Meteor. Soc., 218-223.

Linne, H., and J. Bösenberg, 2003: Heterodyne lidar - a tool to investigate dynamic processes in the lower troposphere. 6th International Symposium on Tropospheric Profiling: Needs and Technologies, Leipzig, germany, September 14-20, 2003.

Lumley, J. L. and H. A. Panofsky, 1964: *The Structure of Atmospheric Turbulence*. Wiley-Interscience, New York, 239 pp.

Monin, A. S., A. M. Obukhov, 1954: Basic laws of turbulent mixing in the ground layers of the atmosphere. *Trans. Geoph. Inst. Akad. USSR*, **151**, 163-187.

Neff. W. D., 1990: Remote sensing of atmospheric processes over complex terrain. Meteorological Monographs, vol. 23, No. 45, American Meteorological Society, Boston, Mass., 173-228.

Pearson, G. N., P. J. Roberts, J. R. Eacock, M. Harris, 2002: Analysis of the performance of a coherent pulsed fiber laser for aerosol backscatter applications. *Appl. Opt.* **41**, 6442-6450.

Post, M. J., R. A. Richter, R. M. Hardesty, T.R . Lawrence, F. F. Hall Jr., 1981: NOAA's Pulsed, Coherent, Infrared Doppler Lidar - Characteristics and Data. *Proc. Soc. Photo-Opt. Instr. Eng.* **300**, 60-65.

Post, M. J. and R. E. Cupp, 1990: Optimizing a pulsed Doppler lidar. *Appl. Opt.* **29**, 4145-4158.

Press, W. H., S. A. Teukolsky, W. T. Vetterling, B. P. Flannery, 1992: *Numerical recipes in C, the art of scientific computing, second edition.* Cambridge University Press, New York, Cambridge 994 pp.

Priestley, C. H. B., 1959: *Turbulent Transfer in the Lower Atmosphere.* Univ. Chicago Press, Chicago.

Rinhart, R. E., 1991: *Radar for meteorologists.* Knight Printing Company, Fargo, North Dakota, 334 pp.

Roberts, O. F. T., 1923: The theoretical scattering of smoke in a turbulent atmosphere. Proc. R. Soc. London Ser. A 104, 640-654.

Rossby, C. G. and R. B. Montgomery, 1935: The layer of frictional influence in wind and ocean currents. Papers in Physical Geography and Meteorology, Cambridge, Mass., 3 (3).

Sridharan, A. K., K. Urbanek, R. Roussev, S. Saraf, T. S. Rutherford, C. Voss, M. M. Fejer, R. L. Byer, 2003: High pulse energy Yb:YAG MOPA and non-linear frequency conversion module for remote sensing applications. Earth Science Technology Office (ESTO), third annual Earth Science Technoclogy Conference (ETSC), University of Maryland, June 24-26, 2003.

Steyn, D. G., M. Baldi, R. M. Hoff, 1999: The detection of mixed layer depth and entrainment zone thickness from lidar backscatter profiles. *J. Atmospheric and Oceanic Technology* **16**, 953-959.

Stull, R.B., 1995: *Meteorology today for Scientists and Engineers.* West Publishing Company, Minneapolis/St. Paul, 385 pp.

Stull, R. B., 1988: *An Introduction to Boundary Layer Meteorology.* Kluwer, Dordrecht, 666 pp.

Swinbank, W. C., 1963: Long-wave radiation from clear skies. *Quart. J. Roy. Meteor. Soc.*, **89**, 339-348.

Taylor, G. I., 1915: Eddy motion in the atmosphere. Phil. *Trans. R. Soc. London Ser. A*, **215**, 1-26.

Taylor, G. I., 1921: Diffusion by continuous movement. *Proc. London Math. Soc. Ser. 2*, **20**, 196-212.

Ulden, van A.P. and J. Wieringa, 1996: *Atmospheric boundary-layer research at Cabauw.* Boundary-layer Meteorology, **78**, 39-69.

University of Minnesota, 1993: National Science and Technology Research Centre for Computation and Visualisation of Geometreic Structures (The Geometry Centre). For Information about qhull, see http://www.qhull.org/

Wiser, A., R. Calhoun, C. Kottmeier, 2005: The Karlsruhe Doppler wind lidar: Comparison with tower, profiler, sodar, radioson and tethersonde data. European Geosciences Union General Assembly 2005, 24.-29. April 2005, Vienna, Austria.

Willis, G. E., J. W. Deardorff, 1974: A laboratory model of the unstable planetary boundary layer. *J. Atmos. Sci.*, **31**, 1297-1307.

Wulfmeyer, V., S. Mayor, S. Spuler, W. A. Brewer, R. M. Hardesty, B. Rye, C. Bollig, 2003: Doppler lidar design study. Editor: V. Wulfmeyer, Universit Hohenheim, 109 pp.

Acknowledgements

I want to express my gratitude to all those who helped me to complete this diploma thesis and bring my studies to a successful end.

- Prof. Dr. Ch. Kottmeier for providing this very interesting subject and enabling me to take part in CSIP and other field campaigns.
- Prof. Dr. K.D. Beheng for acting as co-referee.
- Dr. A. Wieser for all the help in using Matlab and Tex and many more questions concerning my thesis. The always open ear for problems with the lidar technique and other obstacles. The thorough reading of the manuscript.
- Dr. N. Kalthoff for his engagement and help in discussing the progress of the work and the correction of the written thesis.
- My fellow students for the help and input when studying and great times enjoying student life.
- All staff from the field campaigns I was able to take part in during my time as a student, for the good times during the campaigns.
- My parents for their support throughout my studies when ever I needed it.
- Most over all my wife for the moral support, the helping suggestions and her understanding. My son for the joy and happiness he brought into my life the past seven months.
- All those I did not mention ...

Ich versichere wahrheitsgemäß, die Arbeit selbständig angefertigt und alle benutzten Hilfsmittel vollständig und genau angegeben und alles kenntlich gemacht zu haben, was aus Arbeiten anderer entnommen wurde. Ich erkläre mich damit einverstanden, dass diese Arbeit in die Institutsbibliothek gestellt und kopiert werden darf.

Karlsruhe, den 1. Dezember 2005

Roger Huckle